

**FIRN-AIR MODELLING IN THE
COMMUNITY FIRN MODEL**



CAROLVS
II
SOCIETATIS
REGALIS
AVTHOR
&
PATRONVS

SOCIETATIS PRES.

ARTIVM INSTAVRATOR

Bacon inu. D.D.C.

Wenceslaus Hollar sculpit 1667.

FIRN-AIR MODELLING IN THE COMMUNITY FIRN MODEL

– UNEARTHING THE PAST –

Author Jesper Ejlebak Holm
Advisor Assoc. Prof. Vasileios Gkinis
Advisor Post. doc. Michael Döring



UNIVERSITY OF
COPENHAGEN

PICE

Physics of Ice, Climate and Earth
The Niels Bohr Institute

This thesis has been submitted for
the degree of Cand. Scient. in Physics
of

The Faculty of Science
University of Copenhagen

MAY 22ND 2023

FRONTISPIECE

The frontispiece is from *The History of the Royal Society of London* by Thomas Sprat, 1667, etched by Wenceslaus Hollar Bohemian. National Galleries Scotland (CC BY-NC 2.0)

LOGO

The logo is from *The University of Copenhagen* based on the original seal from 1537, made in 2000 by Kontrapunkt

COLOPHON

This thesis was set with \LaTeX using the *kaobook* class. The body text font is CHARTER 10/12.6, on normal A4 paper, while, the sans serif is FiraSans, the mono is Inconsolata. Graphics created using Matplotlib under Python 3.8, TikZ/PDF, © Jesper Ejlebæk Holm 2023

To my family for their constant support and encouragement throughout my education

AS A SPECIES, WE'VE SOMEHOW SURVIVED LARGE AND SMALL ICE AGES,
GENETIC BOTTLENECKS, PLAGUES, WORLD WARS AND ALL MANNER OF
NATURAL DISASTERS, BUT I SOMETIMES WONDER IF WE'LL SURVIVE
OUR OWN INGENUITY.

- DIANE ACKERMAN, 2014- , *THE HUMAN AGE: THE WORLD SHAPED BY US*

Abstract

Over the last glacial period, a series of 25 climate fluctuations were observed, characterized by rapid warming followed by a longer cooling period. One of these Dansgaard-Oeschger (D-O) events happened around 11,500 years ago and heralded the end of the ice age and the beginning of the Holocene period. To simulate these events, studies use firn densification models coupled to air and heat diffusion in order to reconstruct paleotemperatures.

The Community Firn Model (CFM) is one such example, and it provides an open-source-modular framework to simulate physical processes in the firn. A 1-dimensional Lagrangian grid is used where density is explicitly calculated while diffusion is solved through an implicit Finite Volume Method (FVM). The project seeks to aid in the interpretation of these DO-events by conducting two experiments to better understand the model's behaviour under different conditions.

Initially, we examine the behaviour of the CFM with different densification schemes by testing a variety of "DO-like" events. It is observed that higher temperatures and lower accumulation rates lead to a shallower close-off depth. Secondly, noisy $\delta^{15}\text{N}$ data, computed from NGRIP, is inverted into noisy temperature data by way of Brent's root-finding method. Then the sensitivity of the inverted temperatures is estimated by including uncertainty from sources such as $\delta^{15}\text{N}$, surface density and diffusivity parameterization. We find that the magnitude of the $\delta^{15}\text{N}$ uncertainty is paramount for reliable interpretation of reconstructed temperatures.

Finally, the halfway time to a new equilibrium following a linear fluctuation is computed for a series of different amplitudes and duration. We show that for changes in amplitude, the halfway time tends to decrease, while the behaviour is more complex for the duration. Moreover, we estimate the uncertainty of the temperature gradient by calculating the excess of stable nitrogen isotopes compared to argon. This is used to compute the true equilibrium time for which the opposite behaviour is seen. Based on this the merits of the Halfway time versus Equilibrium time are discussed in the view of interpreting past climates.

Table of Contents

1	Introduction	1
1.1	History of Ice cores	1
1.2	Dansgaard Oescher events	1
1.3	Overview of the dissertation	2
2	Theoretical preliminaries	3
2.1	Ice sheets and ice cores	3
2.2	Firn Physics	5
2.2.1	Zones of densification	5
2.2.2	Firn densification models	7
	Herron and Langway	7
	Sigfus	10
	Barnola	10
	Goujon	11
2.2.3	Gas diffusion and air advection	13
	Gravitational and Thermal fractionation	14
2.2.4	Firn transport equation	15
	Diffusivity parameterization	17
	Firn air advection	18
2.3	Inverse modelling: Brent's method	20
3	Methods, models and data	23
3.1	The Community Firn Model	23
3.1.1	Overview of model calculations	23
	Spin-up run	25
	Main run	25
	Outputs for the CFM	28
3.2	Data	32
3.2.1	Nitrogen data	33
3.2.2	Temperature reconstruction	33
3.2.3	Accumulation rates	33
3.2.4	Setup for Experiment 1	34
3.3	Root finder	35
3.3.1	Speeding up the computation: Multiprocessing	36
4	Experiments	39
4.1	Steady state: Forward model runs	39
4.2	Steady state: Temperature sensitivity	39

4.3	Response to changing duration and magnitude of input forcing	40
4.3.1	Addendum: Equilibrium time	40
5	Results and Discussion	43
5.1	Steady state: Forward model runs	43
5.1.1	Performance comparison between densification schemes	43
5.1.2	Deviation between diffusivity parameterizations	44
5.2	Steady state: sensitivity tests	45
5.2.1	Densification schemes	46
5.2.2	Uncertainty in other parameters	47
5.2.3	Dependence on temperature	51
5.3	Response to changing input forcing	51
5.3.1	Varying magnitude	52
5.3.2	Varying duration	55
5.3.3	Addendum: Argon and true equilibrium time	55
6	Conclusion and outlook	59
A	Configuration files for the CFM	61
B	Algorithm flowcharts	63
C	NGRIP data	65
D	Distribution plots	69
D.1	Densification models	69
D.2	Diffusivity	72
D.2.1	Multiple peaks	72
D.3	Influence of Density	77
D.4	Influence of Diffusivity parameterization	79
E	Additional plots for changing forcing Halfway-time	81
E.1	Changing duration	81
E.2	Changing magnitude	83
F	Additional plots for changing forcing Equilibrium time	85
F.1	Changing duration	85
F.2	Changing duration	87
	Bibliography	89
	Index	98

List of Figures

2.1	Picture of ice core	3
2.2	Fractionation of stable water isotopes	4
2.3	Zones of transport in firn	6
2.4	Schematic of firn column with depth and density	7
2.5	Arrhenius plots for the logarithm of k_0 and k_1 vs. inverse temperature	9
2.6	Schematic of solid state sintering	10
2.7	Firn density-depth profiles for four densification models at 242K	13
2.8	Thermal and gravitation fractionation for BAR	16
2.9	Schematic of bulk air motion in the firn	19
2.10	Plot of close-off depths and $\delta^{15}\text{N}_{\text{cod}}$ for four densification models	20
3.1	Computation flowchart of the Spin-up run for the CFM	26
3.2	Computation flowchart of the Main run for the CFM	27
3.3	CFM Close-off depth plotted with temperature gradient	29
3.4	Typical CFM outputs with densification model Barnola and firn air enabled	30
3.5	Dataset from NGRIP Kindler et al. [23], 120 to 85 kyr b2k	31
3.6	Map of the Location for NGRIP and other sites	32
3.7	Accumulation rates fitted to surface temperatures	35
3.8	Computation flowchart for the Rootfinder	37
5.1	Modelled $\delta^{15}\text{N}_2$ and close-off depths plotted as a function of temperature: densifi- cation schemes	44
5.2	Modelled $\delta^{15}\text{N}_2$ plotted as function of temperature: effective diffusivity	45
5.3	Result of inversion for 225 K with different densification schemes for $N = 200$	46
5.4	Result of inversion for 225 K with uncertainty in different parameters for $N = 2400$, $\sigma_{15\text{N}} = 0.02$ permil	49
5.5	Result of inversion for 225 K with uncertainty in different parameters for $N = 2400$, $\sigma_{15\text{N}} = 0.002$ permil	50
5.6	Relationship of reference temperature and uncertainty for reconstructed tempera- tures	51
5.7	Response of CFM for changes in magnitude	53
5.8	Halfway times for changes in magnitude	54
5.9	Halfway times for changes in duration	56
5.10	Equilibrium times for changes in magnitude and duration	58
B.1	Test	63
C.1	Dataset from NGRIP Kindler et al. [23], 120 to 85 kyr b2k	65
C.2	Dataset from NGRIP Kindler et al. [23], 120 to 85 kyr b2k	66
C.3	Dataset from NGRIP Kindler et al. [23], 120 to 85 kyr b2k	67
D.1	Collection of plots showing results for $T_{\text{ref}} = 220$ K.	69

D.2	Collection of plots showing results for $T_{ref} = 225$ K.	70
D.3	Collection of plots showing results for $T_{ref} = 235$ K.	70
D.4	Collection of plots showing results for $T_{ref} = 240$ K.	71
D.5	Result of inversion for 225 K with uncertainty in different parameters for $N = 2400$	72
D.6	Result of inversion for 225 K with uncertainty in different parameters for $N = 2400$	73
D.7	Collection of plots showing results for $T_{ref} = 220$ K.	74
D.8	Collection of plots showing results for $T_{ref} = 225$ K.	75
D.9	Collection of plots showing results for $T_{ref} = 235$ K.	76
D.10	Depth-density profile at 220 K	77
D.11	Depth-density profile at 230 K	78
D.12	Depth-density profile at 240 K	78
D.13	Depth-diffusivity profile at 220 K	79
D.14	Depth-diffusivity profile at 234 K	80
D.15	Depth-diffusivity profile at 244 K	80
E.1	Response of CFM for changes in duration of Acc	81
E.2	Response of CFM for changes in duration in Temp	82
E.3	Response of CFM for changes in duration in both	82
E.4	Response of CFM for changes in magnitude of Acc	83
E.5	Response of CFM for changes in magnitude in Temp	84
E.6	Response of CFM for changes in magnitude in both	84
F.1	Response of CFM for changes in duration of Acc	85
F.2	Response of CFM for changes in duration in Temp	86
F.3	Response of CFM for changes in duration in both	86
F.4	Response of CFM for changes in magnitude of Acc	87
F.5	Response of CFM for changes in magnitude in Temp	88
F.6	Response of CFM for changes in magnitude in both	88

List of Tables

3.1	Example input forcing file for temperature and accumulation	24
3.2	Overview of $\delta^{15}\text{N}$ laboratory measurements	33
5.1	Table of reference temperature, mean and standard deviation for steady-state distribution experiments	47
5.2	Table of reference temperature, mean and standard deviation for steady-state distribution experiments	49

Preface

As a Physics student, this dissertation is my crowning achievement after five years of study. In addition, it is also the culmination (so far) of my deep interest in \LaTeX , typography and book design. The *kaobook*-template[1] is used for the design, which is based upon the PhD thesis of Ken Arroyo Ohori[2] and the classic Tufte handouts[3]. I make use of 1.5 column space, which allows for a much wider margin than other documents. This space is then used for side notes, margin figures, captions, references and a mini table of contents for each chapter. This means that, unlike footnotes, the reader only needs to look to the margin for notes¹ instead of at the bottom of the page. Side-references are used for key references, the first time they are referenced to avoid overflow in the margins.

As for typefaces, I have a confession to make, while I would very much like to use a professional typeface, they tend to be rather expensive, and I am but a university student. To remedy this, the *CHARTER* typeface is used for the body text upon the advice of Matthew Butterick[4]. This slab-serif typeface features *SMALL CAPS*, old-style figures in text mode (0123456789) and lining figures in math mode (0123456789). This font is paired with *FiraSans* for chapter headings from the advice of Markus Kohm[4], since serif typefaces would be too heavy, while, the mono-typeface *Inconsolata* is used for code listing.

Finally, I cannot recommend the HTML book *PRACTICAL TYPOGRAPHY* by Butterick [4] enough. It is in my view, mandatory for anyone serious regarding typography.

¹: Like this one: Hello World!

2023, Butterick: *Practical Typography*

Acknowledgements

In all fields of research, no project is completed alone. This dissertation would not have been possible if not for the support, guidance and wisdom of many people. First, I would like to thank my supervisors Vasileios and Michael for their advice, support and discussions throughout the project.

- ▶ Thank you, Vasileios, for taking me under your wing, although I at the time had little experience in firm modelling and for guiding me towards *much* cleaner Python code.
- ▶ Thank you, Michael, for the many long discussions about firm physics and for your interest in keeping a well-stocked library of firm-physics papers and dissertations.

I would also like to thank all the people at PICE, that I may or may not have interacted with throughout my studies.

- ▶ Special thanks to Maria Bramsen for making the transition from courses to thesis-writing as seamless as possible.
- ▶ Thanks to the people at Vejrbalonen: Alfred, Niels, Josephine, Jon and Lide for making my stay at PICE enjoyable and providing me with much-needed experience from other people in project work.
- ▶ Thanks to Jonathan Melcher for teaching me about Erda multiprocessing.

Moreover, as someone with autism, the guidance of the three below, has been instrumental in ensuring that I succeed in this endeavour.

- ▶ I have had the wonderful experience of having Mette Sckerl as my støtteperson/support person from the beginning of my B.Sc. degree until my second M.Sc. year. The weekly meetings allowed me to thrive amidst studies and international crises such as the pandemic etc.
- ▶ Next, I would like to thank Rikke Klausen in her capacity of study-mentor and for supporting me during the final M.Sc. year. The weekly meeting and your advice regarding thesis writing, article reading and deadline management have been a great boon.
- ▶ Finally, I would like to thank Ahmed for being my contact person at Studenterrådgivningen throughout my university studies. I am especially thankful for your support in managing a project amidst disruptions from other events in the world.

In other news, I owe a thanks to my friends: Nikolaj, Jonas and Mikkel for being constant study-companions throughout our studies.

- ▶ To Nikolaj, a fellow prequel memes connoisseur, workaholic and for helping me with my at times rather long sentences.
- ▶ To Jonas, for your wisdom in Python and amazing time-bending ability to stay updated with science videos on Youtube.

- ▶ To Mikkel, for being a fellow non-theoretical physicist and for your knowledge of obscure strategy board games. I wish you good luck in your studies.

To my friends in UNF, thanks for being a wonderful group of people and for the many long adventures in pedantry. To my friends from Flakkebjerg Efterskole, thanks for a wonderful year back in 2014/2015 and our experiences since then. To my high school teachers in Mathematics and Physics Svend and Daniel, thanks for your guidance and for teaching me about \LaTeX .

Finally, to my family, for their constant support and encouragement, and for instilling in me a love of travel.

- ▶ To my father Niels Erik, thanks for introducing me to science at an early age by teaching me about orders of magnitude. The later trips to CERN and London served only to solidify that interest.
- ▶ To my mother Anne, thanks for being a fellow travel enthusiast and for our many trips to Italy and Firenze. I am also thankful for our weekly telephone calls during the pandemic, which helped to navigate a chaotic world.
- ▶ To my sibling Skye, thanks for being a wonderful person and your support in navigating a world designed for neurotypical people. I am especially thankful for our discussions regarding our similar and dissimilar interests.

As a final note, I would like to thank the Lenovo ThinkPad laptop, that Vasileios lent me. It has been a tireless companion, even though it has been running near constantly since march.

1.1 History of Ice cores

Ice core drilling is a relatively new science, perhaps due to the harsh environmental conditions on the polar ice sheets. According to Langway [5], the first measurements of ice sheet interior were taken by Sorge [6], but then a pause of research followed until the 1950s¹. Then three research projects began[5, 7]: Queen Maud Land in Antarctica [8, 9], Juneau in Alaska[10] and in Central Greenland [11]. These ice cores were only 100 meters deep, and the ice recovered suffered from low quality, limiting detailed research[7, 12]. In the advent of the International Geophysical Year in 1957-1958, ice core drilling began in earnest with major contributions from the USA, the Soviet Union, and Denmark. Switzerland and France. After a period of six years from 1960, the first continuous ice core to bedrock was obtained at Camp Century[7]. These ice-core projects have since continued with many successful ice cores, such as ones from Greenland (GISP, GRIP NGRIP and most recently EGRIP etc.) and Antarctica (Vostock, Dome Fuji and Dome C etc.).

1.2 Dansgaard Oeschger events

Over the last glacial period, a series of 25 climate fluctuations were observed, characterized by rapid warming over decades followed by a longer cooling period of centurial or millennial timescales[13, 14]. These events are known as Dansgaard-Oeschger (DO) events named after Willi Dansgaard and Hans Oeschger, pioneers in the ice core science. Dansgaard championed the connection between the isotopic composition of polar ice and, the precipitation and site temperature [15, 16], while Oeschger and his associates developed methods[5] to measure the change in ¹⁴C in Carbon-dioxide gas extracted from the Ice cores. These DO-events are well studied, yet an exact and comprehensive mechanism is elusive[17]. Proposed mechanisms include binge-purge oscillations of ice-sheets[13, 18, 19], bipolar seesaw as a connection to the South seas[20] and a connection to Atlantic Meridional Overturning Circulation (AMOC)[21, 22]. One of these DO events happened around 11,500 years ago and marked the end of the ice age and the beginning of the Holocene period[14, 23]. Inspired by the experiments performed in [24–26], this thesis will examine the Community Firn Model and how its outputs might be used to gain knowledge useful for interpreting past climate histories. Specifically, we first examine the behaviour of the CFM with different

1.1 History of Ice cores	1
1.2 Dansgaard Oeschger events	1
1.3 Overview of the dissertation	2

¹: Understandable, given the war and the unrest that followed it

densification models for a variety of DO-like events. Secondly, we invert noisy $\delta^{15}\text{N}$ data from [23] into noisy temperature data and the resulting standard deviation is analysed. Finally, we force the CFM with warming signals of varying duration and magnitude, while recording characteristic equilibrium times. Before we do so, it is necessary to review a number of topics relating to firm modelling.

1.3 Overview of the dissertation

- ▶ In Chapter 2, the necessary firm physics and concepts are introduced alongside Brent's method
- ▶ In Chapter 3, the Community Firm Model and the data from Kindler et al. [23] is introduced. We also present the computation flow for the inversion method.
- ▶ In Chapter 4, we give a brief overview of the methodology in each experiment. Additionally, the uncertainty of the temperature gradient is estimated.
- ▶ In Chapter 5, we discuss how the behaviour in the experiments can be understood by applying our knowledge from previous chapters.

Theoretical preliminaries

2

In this chapter, we present all necessary preliminary knowledge necessary to proceed to the next section describing the methodology. In Section 2.1, we give a brief introduction to Ice cores, the concept of delta-notation and why we are interested in stable nitrogen isotopes. Secondly, in Section 2.2 we detail all densification schemes used in the thesis. We also detail the different components of the firn-air transport equation including fractionation, advection and diffusivity parameterizations. Finally, in Section 2.3, the method for inverting the Community Firn Model is explained, with more to come in Section 3.3.

2.1	Ice sheets and ice cores	3
2.2	Firn Physics	5
2.3	Inverse modelling: Brent's method	20

2.1 Ice sheets and ice cores

When snow falls in favourable climates and doesn't melt, ice sheets and glaciers form over many thousands of years as layers of snow accumulate. The chemical composition of each layer is mainly influenced by temperature and precipitation, in addition to wind, volcanic ash, sea salt etc. Gradually these layers are compressed by the weight of overlaying layers and turn to ice along with particulates and dissolved chemicals, while ancient air is trapped in bubbles. In this way, ice cores drilled at the ice sheets become a proxy for climatic information about the precipitation [27, 28] and temperature [13], volcanic activity [29, 30], the composition of the ancient atmosphere such as CO₂ [31, 32] and CH₄ [33, 34], etc.

The word Ice core refers to a cylindrical section of ice, that has been drilled from the polar ice sheets or mountain glaciers. Most ice cores are obtained from inland sheets since these are more stable. This is typically performed at the ice divide to ensure that the horizontal velocity profile does not interfere with the stratigraphy, making it easier to date the ice.

One climatic proxy in the ice is water stable isotopes (²H and ¹⁸O), where the abundances found in each layer can be used to reconstruct past climates [16]. To better quantify the abundance of water stable isotopes, the δ -notation is used [36]. Here we denote an isotope with $Z+N$ X, where Z is the number of protons, N the number of neutrons and X the specific element. The delta-value of stable isotopes can then be computed as

$$\delta^{Z+N}X = \frac{R_{\text{sample}} - R_{\text{reference}}}{R_{\text{reference}}}, \quad (2.1)$$

2008, Ruddiman: *Earth's Climate*



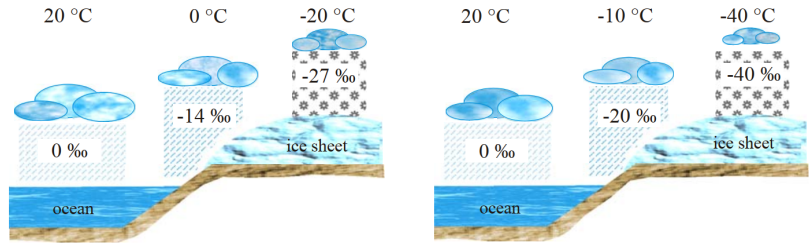
Figure 2.1: Picture of ice core. Adapted from Goss [35]

1964, Dansgaard: 'Stable isotopes in precipitation'

1998, Kendall et al.: 'Chapter 2 - Fundamentals of Isotope Geochemistry'

where R_{sample} is the ratio of heavy isotopes to light isotopes in the specimen and $R_{\text{reference}}$ is that of a standard reference. Next, $\delta^{18}\text{O}_{\text{ice}}$

Figure 2.2: Fractionation of stable water isotopes due to condensation and evaporation. Lighter water molecules evaporate faster due to higher vapour pressure, while also precipitating slower, leading to a depletion in the heavier molecules. [37]



is influenced by three factors[38]: the evaporation temperature at the water source, the path that the water molecules take through the atmosphere and the condensation temperature, see Figure 2.2. First, lighter isotopologues evaporate faster due to vapour pressure compared to heavier isotopologues. Meanwhile, heavier isotopologues are preferentially removed from the air with decreasing temperature through Rayleigh distillation. This can happen due to increasing elevation and latitude or seasonal temperature variability. Finally, warm air contains more water vapour and therefore a higher amount of heavy isotopologues. These effects result in the precipitation (and so the ice sheets) being more depleted in heavy isotopes, which equals a more negative δ -value.

Previously[15, 16, 23, 39–41], this connection between $\delta^{18}\text{O}_{\text{ice}}$ and precipitation and temperature have been used to reconstruct past surface temperatures, where one assumed a function of the form:

$$T_S = \alpha \cdot \delta^{18}\text{O}_{\text{ice}} + \beta \quad (2.2)$$

$$T_S = \alpha^* \cdot \delta^{18}\text{O}_{\text{ice}}^2 + \beta^* \cdot \delta^{18}\text{O}_{\text{ice}} + \gamma^*, \quad (2.3)$$

1: These effects can e.g. be changes in the seasonality of precipitation, sea-ice extent and condensation temperature, see the work by Liu et al. [38]

2: For a description about clathrates see [43] and for their importance in ice cores see [44, 45]

3: From Milankovitch theory: Eccentricity, obliquity and precession House [46]

where α is the slope of the linear function and β the intercept. However, due to various effects¹, these coefficients are not constant over time[42], requiring additional constraints on the surface temperatures. Borehole temperatures can be used for calibrations of slow changes. However, due to smoothing effects arising from heat diffusion in the ice sheet, this method is unable to resolve fast temperature changes and also results in a rapid reduction of the time resolution for past climates[24]. To reconstruct temperature changes stemming from these fast changes, we use stable inert gas isotopes (e.g., $\delta^{15}\text{N}$, $\delta^{40}\text{Ar}$) trapped as bubbles or air clathrates² in the ice matrix during the transition between snow and “glacier”-ice also known as Firn. Since these stable gas isotopes are chemically inert, their isotopic compositions ($\delta^{15}\text{N}$) are constant over orbital time scales³, see Mariotti [47], meaning that any deviation are due to site-specific processes or mechanisms in the firn. To understand, how this $\delta^{15}\text{N}$ signal is created in the firn, we first need to illuminate the characteristics of the firn itself.

2.2 Firn Physics

Firn⁴ is the intermediate stage between snow and glacial ice, that has remained from previous seasons⁵.

As more snow is precipitated on the ice sheet, the accumulating weight causes the underlying layers to gradually compact until the ice reaches the density of pure ice at $\rho_{\text{ice}} \approx 920\text{kg/m}^3$. Far above this density-horizon⁶, gas pores are formed, which keeps the firn air younger than surrounding ice by exchanging air with the upper atmosphere. At the lock-in-depth (LiD), this exchange is no longer possible, and the gas age is now locked. The difference in age between the firn air and the ice is known as Δage and is calculated as:

$$\Delta\text{age} = \text{ice age}_{\text{lid}} - \text{gas age}_{\text{lid}} \quad (2.4)$$

The volume of the firn not composed of ice, i.e. air bubbles, is known as the porosity $s = \rho/\rho_{\text{ice}}$ and is composed of closed s_{cl} and open s_{op} porosity. Here s_{op} refers to pores still interconnected with the overlying atmosphere through other pores[48] and decreases with depth as the ice densifies. Meanwhile, s_{cl} refers to the volume of all gas bubbles, that have been closed off from the atmosphere. After the lock in-depth, this increases with depth before decreasing again due to the compactification and the creation of clathrate ice[45].

There exist several ways of defining the closed porosity s_{cl} . Schwander [49] measured bubble volumes from ice core samples at Siple station, Antarctica and derived the following empirical relation:

$$s_{\text{cl}} = \begin{cases} s \exp \left[\frac{\rho}{\rho_{\text{cod}}} - 1 \right] & \text{for } \rho \leq \rho_{\text{cod}} \\ s & \text{for } \rho \geq \rho_{\text{cod}} \end{cases} \quad (2.5)$$

However, due to the reopening of bubbles during sample cutting, the bubble volume tends to be underestimated in measurements[50]. Alternatively, s_{cl} can be parameterized from density and air content measurements, as done by Goujon et al. [51] for Greenland and Antarctic sites:

$$s_{\text{cl}} = 0.37s \left(\frac{s}{\bar{s}_{\text{co}}} \right)^{-7.6} \quad (2.6)$$

where \bar{s}_{co} is the mean close-off porosity $\bar{s}_{\text{co}} = 1 - \bar{\rho}_{\text{co}}/\rho_{\text{ice}}$. This parameterization is designed[50], so that it is consistent with Equation 2.7 and it shows that 0.37 of the porosity has closed off at $\bar{\rho}_{\text{co}}$.

2.2.1 Zones of densification

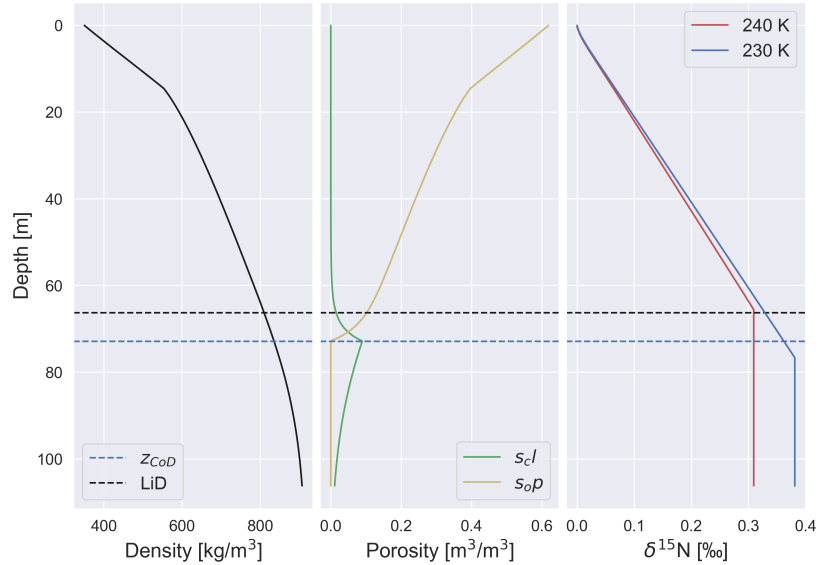
As firn is pushed deeper by the layers above, the grouping of the ice crystals changes the available transport methods of air. As such,

4: From swiss german firn meaning "last year's", only English relic of a word meaning "of last year".

5: In mountain glaciers, the snow is partially melted and refrozen, which allows it to become even more compact and dense than before.

6: The depths whose density is ρ_{ice}

Figure 2.3: Zones of transport in Firn: Left) Firn density modelled using the Herron and Langway model implemented in the CFM for 230 and 240 K. Middle) Open and closed porosity calculated according to Equation 2.6 and Right) $\delta^{15}\text{N}$ distribution with depth for 230 and 240 K modelled with the CFM. Higher temperatures result in a shallower firn column. Adapted from Scheidt [26] and Buizert et al. [50]



the firn column can be divided into three zones each defined by a dominant transport: The convective zone (CZ), the diffusive zone (DZ) and the lock-in zone or non-diffusive zone (LZ).

7: Large concerning temperature fluctuations deeper in the ice.

8: Antarctica features many of these sites such as Vostok and Megadunes since it is a desert [52].

2013, Buizert: 'ICE CORE METHODS | Studies of Firn Air'

The convective zone is the upper reaches of the firn column, subject to large⁷ temperature fluctuations and convection, which maintains the same air composition as the atmosphere so $\delta^{15}\text{N} = 0$. Often, the CZ is only a couple of meters deep as seen in Figure 2.3, due to fast packing. However, deep convective zones can be found at sites with simultaneously low accumulation rates and strong winds⁸.

Just below the CZ is the diffusive zone, and it is of paramount importance for the $\delta^{15}\text{N}$ signal since convection no longer is the prevailing transport. Instead, this zone is dominated by molecular diffusion due to the dimensions of the air pockets [52], with decreasing diffusivity with depth due to pore compaction ($\downarrow s_{op}$). In addition, gravitational fractionation causes enrichment of heavier isotopologues and molecules with depth until the lock-in zone, as seen in Figure 2.3. If there is a thermal gradient[53] in the firn column, heavy isotopologues would tend towards the colder end of the firn column. As an example, rapid warming in a DO event would cause an enrichment of $\delta^{15}\text{N}$ at the bottom, while the rapid cooling observed in the Younger Dryas would have the opposite effect.

In the lock-in zone, enrichment processes due to diffusion cease, since the air channels are now closed off due to the absolute pressure from overlying layers. Here, the air is advected downwards with the ice matrix. Further down still, we approach the close-off depth, defined as the depth where all air channels are closed off and $s_{op} = 0$. The specific density for this is site dependent due to differences in climatic conditions, but parameterizations for the mean close-off density $\bar{\rho}_{cod}$ exist. One such is by Martinerie et al. [54], where $\bar{\rho}_{cod}$ is a function

1992, Martinerie et al.: 'Physical and climatic parameters which influence the air content in polar ice'

of site temperature T

$$\bar{\rho}_{\text{cod}} = \left(\frac{1}{\rho_{\text{ice}}} + 6.95 \cdot 10^{-7} T - 4.3 \cdot 10^{-5} \right)^{-1} \quad (2.7)$$

Finally, the lock-in depth and corresponding lock-in density can be calculated empirically as:

$$\rho_{\text{lid}} = \bar{\rho}_{\text{cod}} - 14 \text{kg/m}^3 \quad (2.8)$$

2.2.2 Firn densification models

Generally, firn densification models describe densification in three separate stages based on the density.

In the past section, we presented an overview of the air transport regimes due to the packing of ice crystals. We will now give an overview of the different densification stages, see Figure 2.4. Until the critical density of 550kg/m^3 , ice crystals are distributed and partially destroyed by wind convection, leading to increased compactification. This is compounded by sublimation and resublimation, where larger crystals grow with the sacrifice of smaller crystals to a more spherical shape. This is the most rapid stage and the density-depth profile now follows a linear trend[55]. After the critical density and until $820 - 840 \text{kg/m}^3$, the crystals can not be packed tighter and a slower sintering process takes precedence. Here individual bubbles begin to form and the densification rate decreases sharply as seen in Figure 2.3. Finally, until the density of ice at 917kg/m^3 , the gas bubbles are further compressed until at last the air molecules are forced into the ice matrix due to the pressure. This happens far below the close-off depth e.g. at NGRIP the bubble to clathrate transition[56] is at $900 - 1600 \text{ m}$.

The Community Firn Model hosts an ensemble of 13 different densification models with use cases ranging from Δage reconstruction, surface elevation changes, ice sheet mass balance etc. Here, we focus on temperature reconstruction, where Δage acts as an additional constraint. We will focus on the following models implemented in the CFM: Herron and Langway [55], Sigfus [55], Barnola [57] and Goujon [51]. These models are constrained from many different sites and are widely used for temperature reconstruction by Δage of polar firn[58].

Herron and Langway

The Herron and Langway model [55] is the progenitor of many densification models due to its wide applicability and serves as a benchmark [58] for other models. It is an empirical model based upon Sorge's Law [59] and depth-density data from 17 firn core sites to

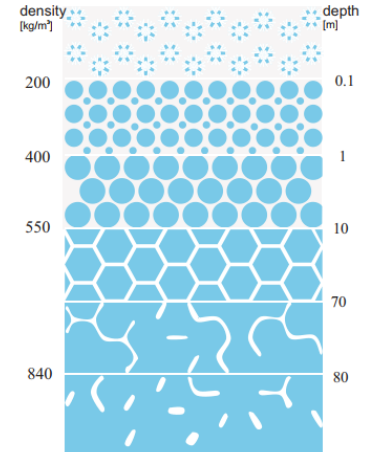


Figure 2.4: Schematic of firn column packing with depth and density. Adapted from Kindler et al. [23]

1980, Herron et al.: 'Firn Densification'

2017, Lundin et al.: 'Firn Model Intercomparison Experiment (FirnMICE)'

1954, Bader: 'Sorge's Law of Densification of Snow on High Polar Glaciers'

determine firm densification rate equations from two key assumptions still used by other firm models. In the CFM, the Herron and Langway model is implemented as a dynamic model, a stress-based model and an analytical solution. Here, we focus on the dynamic model and analytical and return to the third in the next section.

1953, Schytt et al.: 'The Norwegian-British-Swedish Antarctic Expedition, 1949-52. I. Summary of the glaciological work'
1958, Schytt: 'Snow and ice studies in Antarctica'

The dynamical model assumes first [60] that the change in air space i.e., porosity is linearly related to the change in stress due to the weight of overlying snow. Schytt [61] expressed this as:

$$\frac{d\rho}{\rho_{\text{ice}} - \rho} = \text{const. } \rho \, dh \quad (2.9)$$

where ρ_{ice} is the density of ice 917 kg m^{-3} and implies a linear relationship between $\ln \rho / (\rho_{\text{ice}} - \rho)$ and the depth h . Indeed, plotting this relationship for multiple sites shows this trend as two line segments, where the slope changes, when the first densification stage ends. We can express the slope of the segments as:

$$C = \frac{d \ln \rho / (\rho_{\text{ice}} - \rho)}{dh} \quad \rho < 550 \text{ kg m}^{-3} \quad (2.10a)$$

$$C' = \frac{d \ln \rho / (\rho_{\text{ice}} - \rho)}{dh} \quad 550 \text{ kg m}^{-3} < \rho < 800 \text{ kg m}^{-3} \quad (2.10b)$$

where C, C' are constants for each site. Here we substitute with $dh/dt = A/\rho$, where A is the accumulation rate:

$$\frac{d\rho}{dt} = \begin{cases} \frac{CA}{\rho_{\text{ice}}} (\rho_{\text{ice}} - \rho) & \rho < 550 \text{ kg m}^{-3} \\ \frac{C'A}{\rho_{\text{ice}}} (\rho_{\text{ice}} - \rho) & 550 \text{ kg m}^{-3} < \rho < 800 \text{ kg m}^{-3} \end{cases} \quad (2.11)$$

The second assumption is that temperature and accumulation are not correlated and that Equation 2.11 can be expressed as Arrhenius-type rate equations:

$$\frac{d\rho}{dt} = \begin{cases} k_0 A^a (\rho_{\text{ice}} - \rho) & \rho < 550 \text{ kg m}^{-3} \\ k_1 A^b (\rho_{\text{ice}} - \rho) & 550 \text{ kg m}^{-3} < \rho < 800 \text{ kg m}^{-3} \end{cases} \quad (2.12)$$

where k_0, k_1 are Arrhenius-type rate constants that depend on temperature and a, b are constants depending on the densification mechanism. Herron and Langway then obtained values for a, b by comparing slopes for pairs of sites with nearly equivalent temperatures and different accumulation rates with:

$$a = \frac{\ln C_1/C_2}{\ln A_1/A_2} + 1, \quad b = \frac{\ln C'_1/C'_2}{\ln A_1/A_2} + 1$$

Hereby, the values were determined to be $a \approx 1$ and $b \approx 0.5$. The values of the rate constants were determined by plots of $\ln k$ against

$1/T$, see Figure 2.5, to be of the form $k = \text{const. exp}(-Q/RT)$, where Q is the Arrhenius activation energy in kJ mol^{-1} :

$$k_0 = 11 \exp\left(-\frac{10.16}{RT}\right), \quad k_1 = 575 \exp\left(-\frac{21.4}{RT}\right)$$

and R is the gas constant and T is the temperature in Kelvin. The steps above can be neatly summarized into the following rate equation:

$$\frac{d\rho}{dt} = c(\rho_{\text{ice}} - \rho) \quad (2.13a)$$

$$c = \text{const. exp}\left(-\frac{Q}{RT}\right)A^a \quad (2.13b)$$

The analytical formulation of the Herron and Langway model (HLA) is a steady-state model, that given temperature T , accumulation rate A and surface density ρ_0 calculate density, depth and age relations. This model is included here since it is used by the CFM to generate initial spin-up files, see Figure 3.1.

For the n th densification zone, the density is calculated as [55, 58]:

$$\rho_h = \frac{\rho_{\text{ice}} Z_n}{1 + Z_n} \quad (2.14)$$

where for the initial densification zone, i.e. $n = 0$

$$Z_0 = \exp\left[\rho_{\text{ice}} k_0 h + \ln \frac{\rho_0}{\rho_{\text{ice}} - \rho_0}\right]$$

and is independent of the accumulation rate. The depth of the critical density or transition to the second zone is:

$$h_{550} = \frac{1}{\rho_{\text{ice}} k_0} \left[\ln\left(\frac{550 \text{ kg m}^{-3}}{\rho_{\text{ice}} - 550 \text{ kg m}^{-3}}\right) - \ln\left(\frac{\rho_0}{\rho_{\text{ice}} - \rho_0}\right) \right] \quad (2.15)$$

with corresponding age in years:

$$t_{550} = \frac{1}{k_0 A} \ln\left(\frac{\rho_{\text{ice}} - \rho_0}{\rho_{\text{ice}} - 550 \text{ kg m}^{-3}}\right) \quad (2.16)$$

For the second densification zone, we have

$$Z_1 = \exp\left[\rho_{\text{ice}} k_1 \frac{h - h_{550}}{A^{0.5}} + \ln \frac{550 \text{ kg m}^{-3}}{\rho_{\text{ice}} - 550 \text{ kg m}^{-3}}\right]$$

So that the age at a given density is

$$t_\rho = \frac{1}{k_1 A^{0.5}} \ln\left(\frac{\rho_{\text{ice}} - 550 \text{ kg m}^{-3}}{\rho_{\text{ice}} - \rho}\right) + t_{550} \quad (2.17)$$

Finally, the mean annual accumulation rate is estimated from the slope of the second densification zone i.e. $A = (\rho_{\text{ice}} k_1 / C')^2$

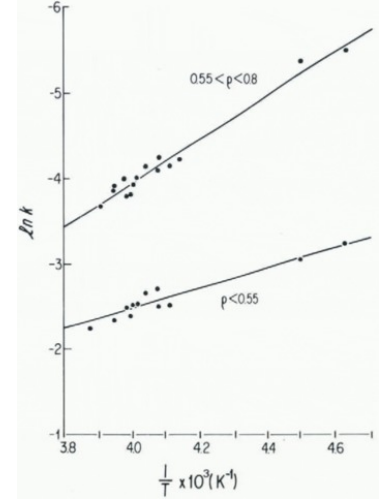


Figure 2.5: Arrhenius plots for the logarithm of k_0 and k_1 vs. inverse temperature. Adapted from Herron et al. [55]

Sigfus

The Sigfus model in the CFM is identical to the Herron and Langway model in the first densification zone. In the second zone, Equation 2.12 may be rewritten to include the stress σ :

$$\frac{d\rho}{dt} = \frac{k_1^2 (\sigma_\rho - \sigma_{550}) (\rho_{\text{ice}} - \rho)}{g \ln \left[\frac{\rho_{\text{ice}} - 550 \text{ kg m}^{-3}}{\rho_{\text{ice}} - \rho} \right]}, \quad (2.18)$$

where σ_{550} is the stress at the critical density with a recommended activation energy of 42.6 kJ mol^{-1} .

Before we continue, it is important to note [62] that the activation energies found in Herron et al. [55] are lower than those predicted by other models. This leads it to be less sensitive to temperature change faster than one-year frequency. In addition, Barnola et al. [57] found that the Herron and Langway model was less suitable for sites with relatively high accumulation rates compared to the site temperature.

Barnola

The Barnola et al. [57] model was developed for Δ age calculations in ice cores. Like the Sigfus model, it uses the Herron and Langway model for the first densification zone, but then uses the Pimienta [63] model for the second and third densification zones [58, 62]. Here, densification below the close-off depth is described to be caused by plastic deformation of the ice around the air channels and bubbles. The densification rate is

$$\frac{d\rho}{dt} = Af\Delta P^n = \rho_{\text{ice}} A_0 \exp\left(-\frac{Q}{RT}\right) f\sigma_{\text{eff}}^n, \quad (2.19)$$

where A_0 is a constant, Q the activation energy for mechanical creep 60 kJ mol^{-1} , ΔP the effective absolute pressure and σ_{eff} the effective stress [57, 62]. Finally, the exponent n ranges between 1 and 3 depending on the stress. Tests on polar ice from Vostok were conducted by Pimienta et al. [64] to determine the dependence of strain rate on the stress $d\varepsilon/dt = A\sigma^n$. For stresses of 0.1 MPa and lower $n = 1$ and for stresses higher than this value $n = 3$, in good agreement with Doake et al. [65]. The function f is given by the spherical pore model of Wilkinson et al. [66] who investigated the densification of a powder compact during pressure sintering of cobalt monoxide:

$$f_s(\rho) = \frac{3}{16} \left[1 - \frac{\rho}{\rho_{\text{ice}}} \right] \left[1 - \left(1 - \frac{\rho}{\rho_{\text{ice}}} \right)^{1/3} \right]^{-3}$$

1991, Barnola et al.: ‘CO₂-climate relationship as deduced from the Vostok ice core’

1987, Pimienta: ‘Étude du comportement mécanique des glaces polycristallines aux faibles contraintes’

1987, Pimienta et al.: ‘Mechanical behavior of anisotropic polar ice’

1985, Doake et al.: ‘Flow law for ice in polar ice sheets’

1975, Wilkinson et al.: ‘Pressure sintering by power law creep’

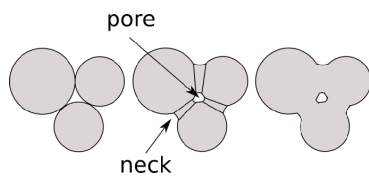


Figure 2.6: Schematic of solid state sintering for porous media. Adapted from Hansen et al. [67]

Barnola et al. analyzed Antarctic and Greenland density-depth profiles with different climatic histories using Equation 2.19 and deduced an empirical function for the second densification zone (550 – 800 kg m⁻³):

$$f_e(\rho) = 10^{\alpha\rho^3 + \beta\rho^2 + \delta\rho + \gamma}, \quad (2.20)$$

where $\alpha = -37.455$, $\beta = 99.743$, $\delta = -95.027$ and $\gamma = 30.673$. For the third densification zone beyond 800 kg m⁻³ Barnola et al. [57] uses the Pimienta model with $f = f_s(\rho)$. The function $f_e(\rho)$ is constructed such that:

$$\rho_c = 800\text{kgm}^{-3} \Rightarrow f_s(\rho_c) = f_s(\rho_c) \ \& \ f'_s(\rho_c) = f'_e(\rho_c) \quad (2.21)$$

Finally, in the CFM n is set to 3 as the effective stress in firn rapidly rises to higher than 0.1 MPa [57].

Goujon

Similar to the Barnola and Pimienta model, the Goujon model takes its roots in Metallurgy by considering grain scale physical processes such as sliding and deformation. In the original work, Goujon et al. [51] uses the densification scheme developed by Arnaud et al. [68] coupled with a simplified heat diffusion model by Ritz [69] without horizontal advection. In the CFM, this set of models is referred to as the Goujon family, since Stevens et al. [62] does include a heat diffusion module with horizontal advection.

In the following, we use the notation by Goujon et al. where ρ is the absolute firn density and $D = \rho/\rho_{\text{ice}}$ is the relative density. Additionally, in Goujon et al. [51] the first, densification zone only begins⁹ after an initial 2-meter convective zone with constant density 350 kg m⁻³. As explained in Subsection 2.2.1, effects due to convection become negligible below the CZ and other effects begin to appear.

In the first zone ($D < 0.6$), snow densifies into firn mainly by the boundary sliding of grains or ice crystals. Alley [70] describes that grains under a vertical load will slide downward and densify unless constrained geometrically by other grains. Here, we define the coordination number Z as being the average number of contacts or local grains in the firn structure¹⁰. Boundary sliding continues until the grains are supported by a tripod of bonds, where, $Z \approx 6$ which based on the work by Alley et al. occurs at the critical density $D_0 \approx 0.6$. The densification rate¹¹ in this zone is given by [70]:

$$\frac{dD}{dt} = \gamma \left(\frac{P}{D^2} \right) \left(1 - \frac{5}{3}D \right), \quad (2.22)$$

where P is the overburden absolute pressure due to the overlying snow layers and γ depends on the viscosity of grains boundary and

2003, Goujon et al.: ‘Modeling the densification of polar firn including heat diffusion’

2000, Arnaud et al.: ‘Physical modeling of the densification of snow/firn and ice in the upper part of polar ice sheets’

9: In the CFM, this does not apply as we can choose a specific CZ depth and only use the densification scheme.

1987, Alley: ‘FIRN DENSIFICATION BY GRAIN-BOUNDARY SLIDING’

10: For more information regarding metallurgy and powder densification, feel free to read through these articles Gotoh et al. [71] and German [72].

11: Note that this rate is not dependent on temperature

geometrical parameters. γ should be set, so that \dot{D} is continuous at the transition between zone-1 and zone-2 densification.

Unlike all previous models, Goujon et al. prescribe a variable critical density dependent on the mean annual temperature at the site based on the empirical relation¹² by Arnaud [73]:

$$D_0 = 0.00226 \cdot T_s [^\circ\text{C}] + 0.647 \quad (2.23)$$

In the second densification zone $0.6 \geq D \leq 0.9$, sliding is negligible or constrained and firm densifies through elastic or plastic deformation of grains, where the effective absolute pressure is induced by contact areas. The densification scheme here is based upon the sintering theory by Artz [Artz [74] and Arzt et al. [75]]

$$\frac{dD}{dt} = 4.1817 \cdot 10^4 \exp\left(-\frac{Q}{RT}\right) (D^2 D_0)^{1/3} \left(\frac{a}{\pi}\right)^{1/2} \left(\frac{4\pi P}{3aZD}\right)^3, \quad (2.24)$$

where Q is the activation energy at 60 kJ mol^{-1} , R is the gas constant, T is the temperature in Kelvin, a is the average contact area between grains relative to the initial grain radius and Z is the coordination number [62, 68]. Here the densification continues until $D = D_{\text{CoD}}$, where D_{CoD} is the relative close-off density adapted from Martinerie et al. [54].

In the third densification zone $0.9 \geq D \leq 1$, the firm ice is compressed further by the deformation of an ice matrix with first cylindrical $D < 0.95$ and then spherical $D \geq 0.95$ pores. The densification rates are as follows [63, 66]:

$$\frac{dD}{dt} = \begin{cases} 2A \left(\frac{D(1-D)}{[1-(1-D)^{1/3}]^3} \right) \left(\frac{2P_{\text{eff}}}{3} \right)^3 & \text{for } 0.9 < D < 0.95 \\ \frac{9}{4} A (1-D) P_{\text{eff}} & \text{for } 0.95 \geq D < 1 \end{cases}, \quad (2.25)$$

with

$$P_{\text{eff}} = P + P_{\text{atm}} - P_b, \quad A = 7.79 \cdot 10^3 \exp\left(-\frac{Q}{RT}\right)$$

where P_{atm} is the surface pressure and P_b the air pressure in the bubble.

Buizert et al. [76] reported an issue in his implementation of the Goujon et al. [51], which is reviewed here due to its importance to the CFM model. In the case that $D_0 \geq 0.6$; which happens for $\approx -20.94^\circ\text{C}$ Equation 2.23, then the term $(1 - 5/3D)$ in Equation 2.22 becomes zero for $D = 0.6$ and negative for $D \geq 0.6$, which is decidedly nonphysical. Furthermore, for $D = D_0 \geq 0.6$, the rate predicted by Equation 2.25 becomes infinite due to a zero contact area. In the

¹²: The corresponding additive constant for Kelvin is 0.03

¹⁹⁸², Arzt: 'The influence of an increasing particle coordination on the densification of spherical powders'
¹⁹⁸³, Arzt et al.: 'Practical applications of hotisostatic Pressing diagrams'

CFM, Stevens et al. [62] remedies this by limiting Equation 2.23 at a maximum value of $D = 0.59$, which occurs for temperatures greater than -25°C corresponding to a density of 541 kg m^{-3} , which results in the Goujon model always predicting the critical density transition at slightly lower densities than the standard 550 kg m^{-3} . In addition, Stevens et al. follow the recommendation by Buizert et al. to modify the transition at relative density $D'_0 = D_0 + \varepsilon$, where ε is a small number. They then iterate Equation 2.22 to find γ using D_0 given by Equation 2.23 that gives the maximum \dot{D} at the bottom of the first densification zone without exceeding \dot{D} at the top of the second densification zone.

In Figure 2.7, the depth-density profile for the four different densification models are plotted using constant forcing at $T = 242 \text{ K}$ and $A = 0.19 \text{ m ice/yr}$. At $\sim 550 \text{ kg m}^{-3}$, the mentioned kink is visible, while the Goujon model has a lower critical density.

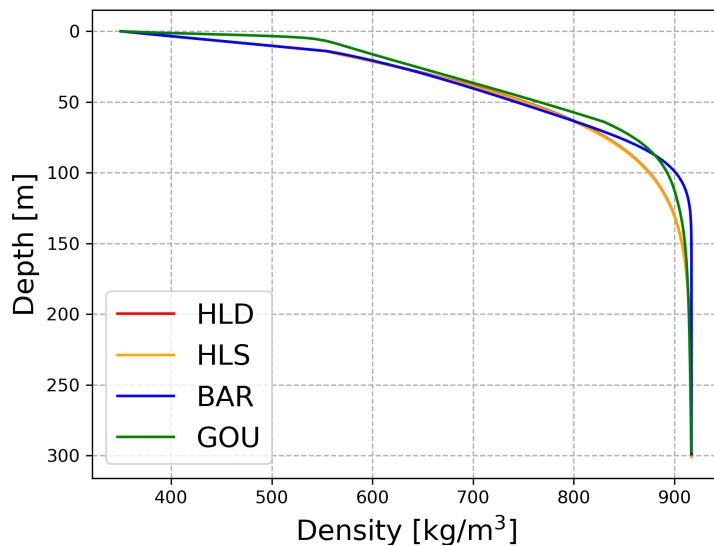


Figure 2.7: Plot of modelled density-depth profiles for four densification models. Firm densification models are Herron and Langway (HLD), Sigfus (HLS), Barnola (BAR) and Goujon (GOU) using constant forcing at $T = 242 \text{ K}$ and $A = 0.19 \text{ m ice/yr}$.

2.2.3 Gas diffusion and air advection

As mentioned in Subsection 2.2.1, the diffusive zone is the origin for two key phenomena that determine the $\delta^{15}\text{N}$ signal, gravitational and thermal fractionation of isotopologues. Besides the two fractionation processes, other mechanisms such as advection, dispersive mixing etc. also play a role in altering the isotopic composition of the air. In this thesis, we model $\delta^{15}\text{N}$ values from firm forcing using two approaches: One relies on solving the one-dimensional firm air transport equation with finite volume methods by Patankar [77] in the module `firm_air`. This method accounts for molecular diffusion, thermal and gravitational fractionation, eddy diffusivity and firm air advection. The other method approximates thermal and gravitation

fractionation according to [49, 78] and [79, 80], which leads to much faster calculations than using the `firn_air` module.

Gravitational and Thermal fractionation

1989, Schwander: ‘The transformation of snow to ice and the occlusion of gases’

1988, Craig et al.: ‘Gravitational Separation of Gases and Isotopes in Polar Ice Caps’

13: See Lente et al. [81] for an overview of different derivation methods, that have been used throughout the ages.

Once convection is negligible, heavier isotopes and molecules are enriched with increasing depth in the firn. We can derive the relation for this enrichment by using the barometric equation Schwander [49] and Craig et al. [78] and ideal¹³ gas law $\rho = nM/V$, $n/V = p/(RT)$:

$$\frac{dp}{dz} = \underbrace{-\rho g}_{\text{Ideal gas}} \Rightarrow \frac{dp}{dz} = -\frac{Mg}{RT}p \Rightarrow p(z) = p_0 \cdot \exp\left(\frac{-Mg}{RT}z\right) \quad (2.26)$$

where p is the partial pressure, ρ the density, g the acceleration constant, n the amount of moles, z the firn depth, M the molar mass, R the ideal gas constant and T the temperature. Following the derivation in Kindler et al. [23], we then compare two gasses a and b , then the ratio $R_{a,b}$ of their respective concentrations C is:

$$R_{a,b}(z) = \frac{C_a(z)}{C_b(z)} = \frac{p_a(z)}{p_b(z)} = \frac{p_{a0} \cdot \exp\left(\frac{-M_a g}{RT}z\right)}{p_{b0} \cdot \exp\left(\frac{-M_b g}{RT}z\right)} \quad (2.27)$$

If we then compare the ratios between top and bottom, then since $p(0) = p_0$:

$$\frac{R_{a,b}(z)}{R_{a,b}(z=0)} = \exp\left(\frac{-\Delta M g}{RT}z\right)$$

where $\Delta M = M_a - M_b$. Finally, we convert this into the δ -notation and obtain the following form for the gravitational fractionation of gas species X in parts per thousand:

$$\delta X_{\text{grav}}(z) = \exp\left(\frac{-\Delta M g}{RT}z - 1\right) \cdot 10^3 \approx \frac{\Delta M g z}{RT} \cdot 10^3 \quad (2.28)$$

Additionally, temperature gradients result in thermal diffusion throughout the firn column, which in turn causes a thermal fractionation effect leading to the enrichment of heavy isotopes at the cold end of the ice matrix. The effect can be expressed as [53, 79]:

$$\frac{R_b}{R_t} = \left(\frac{T_t}{T_b}\right)^{\alpha_T} \quad (2.29)$$

transformed into δ -notation in ppt:

$$\delta X_{\text{therm}}(T) = \left[\left(\frac{T_t}{T_b}\right)^{\alpha_T} - 1\right] \cdot 10^3 \approx \Omega_X \Delta T \quad (2.30)$$

where

$$\Omega_X = \frac{\alpha_{T,X}}{T_{\text{mean}}} \cdot 10^3$$

Here T_t and T_b (R_t, R_b) are the temperature (ratio $R_{a,b}$) at the top and bottom of the firn column, α_T and Ω are respectively the thermal diffusion factor and sensitivity and ΔT the temperature difference between top and bottom. These constants α and Ω varies depending on the molecule and temperature. From the works of Leuenberger et al. [80] and Lang et al. [82], α_T was found empirically for stable nitrogen isotopes:

$$\alpha_T = 4.61198 \cdot 10^{-3} \ln \left(\frac{T_{\text{mean}}}{113.65[K]} \right) \quad (2.31)$$

based on original measurements by Boersma-Klein et al. [83], where T_{mean} is the mean firn temperature given by [83, 84]

$$T_{\text{mean}} = \frac{T_c \cdot T_h}{T_h - T_c} \ln \left(\frac{T_h}{T_c} \right) \quad (2.32)$$

where T_h and T_c are the hot and cold temperatures of the firn respectively. For stable nitrogen isotopes Ω was also calculated by Grachev et al. [85] for a temperature range of -60 to 0 °C:

$$^{15}\Omega_X = \frac{8.656}{T_{\text{mean}}} - \frac{1232}{T_{\text{mean}}^2} \quad (\pm 3\%) \quad \text{‰/°C} \quad (2.33)$$

Finally, in the CFM Ω_N was found to be $\Omega_N = 14.7 \cdot 10^{-3} \text{‰/°C}$ by Grachev et al. [85] and is valid for an average firn temperature of -30 °C. by using Equation 2.33. In this thesis, we designate the contributing fractionation effects on $\delta^{15}\text{X}$ as respectively $\delta^{15}\text{X}_{\text{th}}$ and $\delta^{15}\text{X}_{\text{grav}}$, while the total is given as $\delta^{15}\text{X}_{\text{tot}} = \delta^{15}\text{X}_{\text{th}} + \delta^{15}\text{X}_{\text{grav}}$.

In Figure 2.8, we see the change in close-off depth and $\delta^{15}\text{N}_{\text{cod}}$ due to a DO-like event. In b) higher temperatures lead to a lower close-off depth and shallower firn column due to increased densification. Here, the higher thermal energy in a sense leads to more energy available for crystallization, according to the Arrhenius theorem. As Equation 2.28 is approximately linear in z , $\delta^{15}\text{N}_{\text{grav}}$ is directly proportional to the change in z_{cod} . Meanwhile, a positive temperature gradient ΔT leads to a positive $\delta^{15}\text{N}_{\text{th}}$, where heavier nitrogen isotopes are enriched at the cold end of the firn column. The opposite behaviour is seen during the cooling period, which curiously is not completely symmetrical to the warming signal.

2.2.4 Firn transport equation

Unlike other firn modelling works, the CFM can couple a firn-air transport model with densification schemes and heat diffusion. Instead of relying on steady-state depth-density and diffusivity profiles,

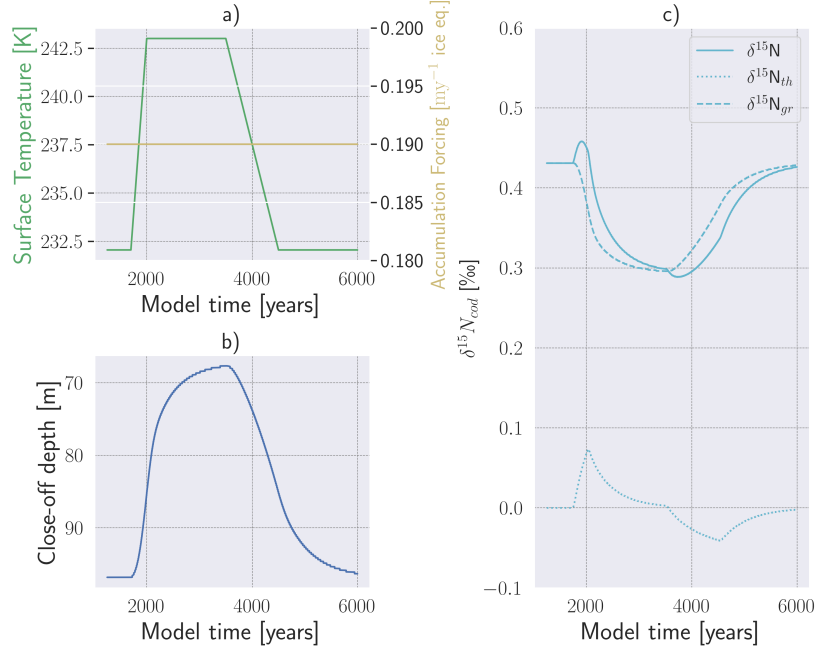


Figure 2.8: Thermal and gravitation fractionation for the Barnola densification model using the advection option by Darcy. Each effect is calculated using Equations 2.28 and 2.30 a) Shows temperature and accumulation forcing, b) shows the change in close-off depth and c) shows $\delta^{15}\text{N}_{\text{tot}}$, $\delta^{15}\text{N}_{\text{grav}}$ and $\delta^{15}\text{N}_{\text{th}}$.

1993, Schwander et al.: ‘The age of the air in the firn and the ice at Summit, Greenland’

1979, Freeze et al.: *Groundwater*

we can instead simulate gas transport together with the evolution of depth-density forced by changing temperatures and accumulation. Originally Schwander et al. [86] introduced a transport equation adapted from hydrology [87], that only included molecular diffusion and gravitational settling. However, over a long period, this was upgraded by among others [50, 88–92] to also contain thermal diffusion, air advection and eddy diffusion [90, 93]. Therefore, the CFM solves the following one-dimensional advection-diffusion-dispersion equation Stevens et al. [62]:

$$\frac{\partial C}{\partial t} = \frac{1}{s_{\text{op}}(t, z)} \frac{\partial}{\partial z} \left[s_{\text{op}}(t, z) \kappa_{\text{eff}}(t, z) \left(\frac{\partial C}{\partial z} - \frac{\Delta M g}{RT} + \Omega \frac{dT}{dz} \right) + s_{\text{op}}(t, z) \kappa_{\text{eddy}}(z) \frac{dC}{dz} \right] - w_{\text{air}}(z) \frac{\partial C}{\partial z} \quad (2.34)$$

where C is the concentration of a gas species in ppm or ppt. The unitless parameter s_{op} is the open porosity, ΔM the molar mass difference either between two isotopologues or from the air in $[\text{kg mol}^{-1}]$, Ω is the thermal diffusion sensitivity $[\text{K}^{-1}]$ for a gas species, $w_{\text{air}}(z)$ is the advection rate relative to the ice matrix and $\kappa_{\text{ef}}(t, z)$ is the effective diffusivity and accounts for the longer, more tortuous path that air takes as the open porosity decreases. There are several ways to parameterize this diffusivity, and we review them in the section below.

Additionally, convection can be included in several ways for modelling firn air transport. A rudimentary way is to treat the firn column as beginning from the bottom of the convective zone and have the air above being of atmospheric composition. Another option is to include an eddy diffusion term, affecting all gasses equally from Kawamura et al. [94]:

$$\kappa_{\text{ed}} = \kappa_{\text{eddy}}(z) = \kappa_{\text{eddy}}^0 \exp\left(-\frac{z}{H}\right)$$

where κ_{eddy}^0 is the eddy diffusivity at the surface and H is a characteristic depth scale chosen in the CFM to be the convective zone depth.

Diffusivity parameterization

In total, the CFM hosts an ensemble of six different parameterizations for effective diffusivity. Here, they are reviewed shortly in chronological order as they appear in the CFM `firn_air.py` module. The first three are very similar as they were developed from each other.

Schwander et al. is the first parameterization and was found using linear regression through measured diffusivities of CO₂ by Schwander et al. [95] and should have good global validity according to the authors. It is given as[62]:

$$\kappa_{\text{eff}} = \gamma_{\text{N}} \cdot D(s) = \gamma_{\text{N}} \cdot c (23.7s_{\text{tot}} - 2.84), \quad (2.35)$$

where $\gamma_{\text{N}} = 1.2638$ is the free-air diffusivity of nitrogen relative to CO₂ from [89, 96] and $D(s)$ is the diffusion coefficient for CO₂ relating to the total firn porosity. c is a temperature and pressure correction factor:

$$c = \frac{p_0}{p} \left(\frac{T}{253.16\text{K}} \right)^{1.85} \quad (2.36)$$

from [97], p, p_0 the mean and reference pressure and T the mean temperature¹⁴. Finally, CFM includes a factor 10^{-6} as unit conversion.

¹⁴: Stevens et al. [62] notes that it does not work very well in the `firn_air.py` file

Battle et al. is next, where the model by Schwander et al. [95] is used as an initial guess to match the diffusivity-depth profile and then adjusts¹⁵ until the model reproduces CO₂ depth profile. This yields the following expression in CFM

$$\kappa_{\text{eff}} = \gamma_{\text{N}} \cdot D(s) = \gamma_{\text{N}} \cdot 1.16 (23.7s_{\text{tot}} - 2.84), \quad (2.37)$$

with a unit conversion factor of $1/(24 \cdot 3600)$.

¹⁵: See Battle et al. [98] for a more detailed investigation

Severinghaus et al. uses the same temperature and pressure correction factors as [95], but has a slightly different expression:

$$\kappa_{\text{eff}} = \gamma_{\text{N}} \cdot D(s) = \gamma_{\text{N}} \cdot D_{\text{CO}_2}^0 (2s_{\text{tot}} - 0.167), \quad (2.38)$$

Note that, in the original publication by Severinghaus et al. [53], the diffusivity coefficient and temperature correction factor are calculated for 25°C, however, Stevens et al. [62] instead uses updated values from Buizert et al. [50] at 0°C.

Freitag et al. used three-dimensional reconstructions in combination with pore-scale model simulations to estimate transport properties and the effective diffusivity takes the form[62, 99]:

$$\kappa_{\text{eff}} = \gamma_N \cdot D(s) = \gamma_N \cdot D_{\text{CO}_2}^0 s_{\text{op}}^{2.1} \quad (2.39)$$

Noticeably, Freitag et al. [99] does not use any correction factors and depends on the open porosity instead of the total.

Witrant et al. is a multi-gas tracer study at eleven different polar sites and features Lock-in zone physics for the diffusivity, whereas it is otherwise negligible in other models. The effective diffusivity in the diffusive zone was calculated by Witrant et al. [100]:

$$\kappa_{\text{eff}} = \gamma_N \cdot D(s) = \gamma_N \cdot D_{\text{CO}_2}^0 \left(\frac{T}{273.15 \text{ K}} \right)^{1.8} \frac{p_0}{p} (2.5s_{\text{op}} - 0.31), \quad (2.40)$$

whereas in the lock-in zone κ_{eff} is approximated with a sigmoid curve below a threshold depth z_{thr} :

$$\kappa_{\text{eff}}(z) \approx \frac{D_{\text{thr}} - 10^{-2}}{1 + e^{50(z - (z_F - z_{\text{thr}})/2/z_F)}} + 10^{-2} \quad (2.41)$$

Where $D_{\text{thr}} = 1 \text{ m}^2 \text{ yr}^{-1}$ if the accumulation rate is less than 0.1 m water eq. and $D_{\text{thr}} = 100 \text{ m}^2 \text{ yr}^{-1}$ otherwise.

Adolph et al. is based on Freitag et al. [99] and studied co-located measurements of diffusivity, and permeability together with microstructure on firn core samples. Adolph et al. [101] arrived at the following relationship:

$$\kappa_{\text{eff}} = \gamma_N \cdot D_{\text{CO}_2}^0 \left(k \cdot 10^{6.973} \right)^{-2.79} \quad (2.42)$$

where $k = s_{\text{op}}^{3.71} \cdot 10^{-7.29}$ is the permeability of the firn.

Firn air advection

For air advection relative to the ice matrix, we have two different parameterizations available:

Darcy's law from Hydrology [87, pp. 16-28] and [92] is based on the viscous flow of air through a porous medium (firn). Here, we begin with the barometric equation for hydrostatic equilibrium:

$$p(z) = p_0 \exp\left(-\frac{M_{\text{air}}g}{RT}z\right) \quad (2.43)$$

where, once again, p_0 is the surface pressure, M_{air} the molar mass of air, g the acceleration constant, R the gas constant and T the

temperature at a depth z . Suppose that a deviation to this hydrostatic equilibrium occurs, then the resulting viscous flow is described by Darcy's law[92]:

$$w_{\text{air}} = -\frac{k}{\mu} \left(\frac{dp}{dz} - \frac{M_{\text{air}}g}{RT} p \right), \quad (2.44)$$

where k is the permeability of firn and μ the dynamic viscosity of firn air.

Buizert considers the bulk motion of firn air alongside the fluxes occurring in and between the open and closed porosity during close-off, see Buizert et al. [50]. The flux in the closed porosity is made of the downward transport of bubbles by the ice matrix at an "ice"-velocity $w_{\text{ice}} = A\rho_{\text{ice}}/\rho$, where A is the accumulation rate in m yr^{-1} equivalent. In the open porosity, air can also travel directly downward and is given by w_{air} . In total, the fluxes can be written as

$$\Phi_{\text{op}} = s_{\text{op}}^* w_{\text{air}} = s_{\text{op}} \exp\left(-\frac{M_{\text{air}}g}{RT} z\right) w_{\text{air}} \quad (2.45)$$

$$\Phi_{\text{cl}} = s_{\text{cl}} \frac{p_{\text{cl}}}{p_0} w_{\text{ice}}, \quad (2.46)$$

where the open porosity s_{op} has been rescaled with the barometric equation to account for increasing pressure by depth. The fraction p_{cl}/p_0 is the enhanced pressure in the closed porosity relative to the surface pressure.

In Figure 2.9, Φ_1, Φ_2 are fluxes in/out of the closed porosity, while Φ_3, Φ_4 are fluxes in/out of the open porosity and Φ_5 is the flux from the open to the closed porosity and as such depicts the close-off of air bubbles. Since mass must be conserved, it must hold that the total air flux leaving and entering the system between z and $z + \Delta z$ or $\Phi_1 + \Phi_3 = \Phi_2 + \Phi_4$, which can be generalized to hold for all depths:

$$\Phi_{\text{op}}(z) + \Phi_{\text{cl}}(z) = \Phi_{\text{op}}(z_{\text{cod}}) + \Phi_{\text{cl}}(z_{\text{cod}}) = \Phi_{\text{cl}}(z_{\text{cod}}) \quad (2.47)$$

then combining Equations 2.45 and 2.46 with Equation 2.47, we can solve for the firn air velocity in the open porosity also known as the air advection rate:

$$w_{\text{air}} = \frac{A\rho_{\text{ice}}}{s_{\text{op}}^*} \left(\frac{s_{\text{cl}}(z_{\text{cod}})p_{\text{cl}}(z_{\text{cod}})}{\rho_{\text{cod}}} - \frac{s_{\text{cl}}(z)p_{\text{cl}}(z)}{\rho(z)} \right) \quad (2.48)$$

Figure 2.10 shows close-off depths and $\delta^{15}\text{N}_{\text{cod}}$ modelled using densification models (HLD, HLS, BAR and GOU) coupled with heat diffusion and the firn_air module. In Figure 2.10 c), we see the familiar excursions of $\delta^{15}\text{N}_{\text{th}}$ due to thermal fractionation, while the different close-off depths lead to different values for $\delta^{15}\text{N}_{\text{grav}}$ due to the gravitational fractionation (see Equation 2.28 and Figure 2.10).

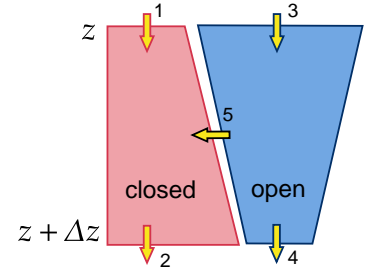


Figure 2.9: Schematic of bulk air motion in the firn from a firn column depth of z to $z + \Delta z$. In this region, total porosity decreases, while the closed porosity increases, i.e., in the lock-in zone. Adapted and modified/recreated from Buizert et al. [50]

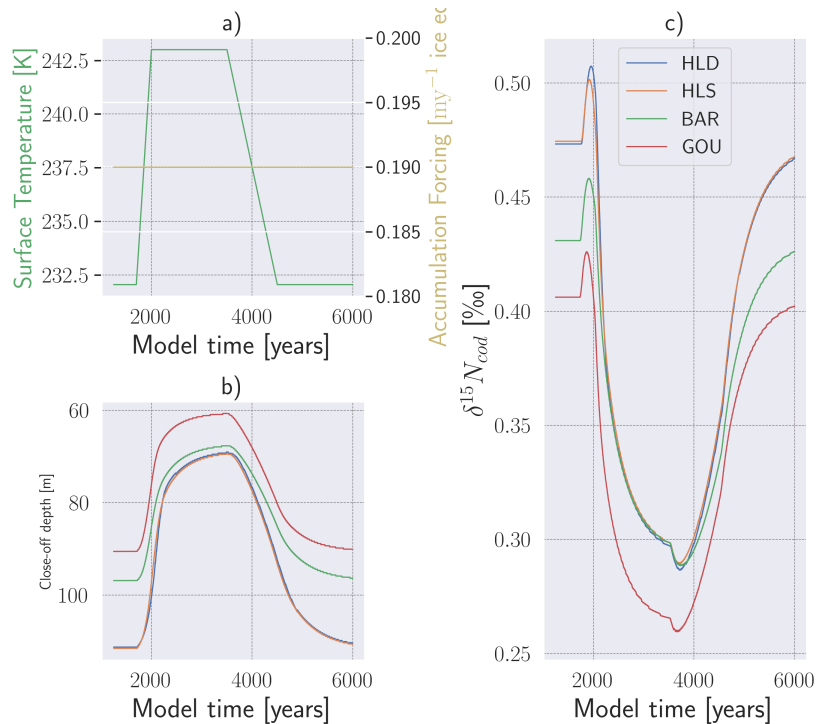


Figure 2.10: Plot of close-off depths and $\delta^{15}\text{N}_{\text{cod}}$ for four densification models a) Shows temperature and accumulation forcing, b) shows the change in close-off depth and c) shows $\delta^{15}\text{N}_{\text{cod}}$

2.3 Inverse modelling: Brent's method

One of the aims of this project is to study the sensitivity of reconstructed temperatures from $\delta^{15}\text{N}$ abundances in ancient air from firn cores. To this end, we invert the Community Firn Model which models firn densification, heat and gas diffusion with a common root-finder from the `scipy.optimize` library [102]. The algorithm chosen here is Brent's method, implemented in SciPy as `optimize.brentq`, which combines secant, bisection and inverse quadratic interpolation.

2020, Virtanen et al.: 'SciPy 1.0'

1971, Brent: 'An Algorithm with Guaranteed Convergence for Finding a Zero of a Function'

16: Other methods have been developed, notably the ITP (Interpolate, Truncate, Project) method, but this has not been implemented in Python to my knowledge yet.

In this section, we will expound on the workings of this algorithm. Brent [103] devised this algorithm based on the work of Dekker [104] which used the fast secant method where possible, and then the slow but robust bisection method in other cases. It is therefore sometimes known as the Brent-Dekker method¹⁶. Brent's method uses the very fast but unstable inverse quadratic interpolation or the secant method where possible and then falls back to the bisection method if necessary. This achieves the reliability of the bisection method while preserving the speed of the faster methods. We will now go through both algorithms since Brent's method is a modification to Dekker's method. Like Dekker's method, Brent's method takes as input a function f and an interval, which contains a root, and then the method promises to converge towards the root with superlinear speed.

Suppose, we are given a function $f(x)$ and we seek the solution x_{opt} so that $f(x_{\text{opt}}) = 0$. In addition, we require an interval $[a_0, b_0]$, which contains a root i.e. $f(a_0) \cdot f(b_0) = -1$. Provided f is continuous between the endpoints, then the intermediate value promises a solution in the interval.

For each iteration, the following points are relevant: b_k the current

guess, a_k and b_{k-1} the previous guess, which for the first iteration is $c_k = b_{k-1} = a_0$. Note that since b_k should always be the best guess, then $|f(b_k)| \leq |f(a_k)|$, if that is not the case then the points are swapped. Next, we calculate two new points:

$$s = \begin{cases} b_k - \frac{b_k - c_k}{f(b_k) - f(c_k)} f(b_k) & \text{if } f(b_k) \neq f(c_k) \\ m & \text{otherwise} \end{cases} \quad (2.49)$$

$$m = \frac{a_k + b_k}{2} \quad (2.50)$$

In other words, if the output of the secant method, s is between b_k and m , then we use it as the new provisional guess $x_{k+1} = s$. Otherwise, if the secant method fails, then the bisection result is used $x_{k+1} = m$. Next, we check for convergence and whether the maximum number of iterations has been reached and finish if any of these are true. Finally, to complete the loop, we compute the following inequality $f(a_k) \cdot f(x_{k+1}) > 0$. If this is true, i.e., the new guess is worse than b_k , but better than a_k then $a_{k+1} = x_{k+1}$, otherwise the guess performs better than b_k and $b_{k+1} = x_{k+1}$. If one wishes to see a more detailed overview, turn to Figure B.1.

The modification of Brent [103] functions by enabling it to use inverse quadratic interpolation (IQI) and using a new variable d ; previously c to handle ill-behaved function. First, it tries to compute the new point s through IQI with a Lagrange interpolating polynomial of degree 2 [105]. If that fails, it will then resume with Dekker's method, except that now we test if s is between b and $\frac{3a+b}{4}$. In addition, it includes another test to force bisection rather than interpolation if the function is ill-behaved. This is done to ensure that the average improvement from step to step is not arbitrarily small. If the function is well-behaved, then Brent's method uses mainly IQI or secant interpolation and will converge at least as fast as Dekker's method will converge regardless of function unlike Dekker's [103].

In Python, this method is implemented by the `scipy.optimize` library as `brentq`, which takes the function f , endpoints a, b in addition to other arguments for f . While we cannot specify the starting guess¹⁷, we can adjust the convergence criterion by the maximum amount of iterations or the absolute x_{tol} and relative tolerance, r_{tol} respectively. The function will finish if it goes through too many iterations or if the guess satisfies `np.allclose(x, x0, xtol, rtol)` i.e., we finish if the following inequality $|a_{k+1} - b_{k+1}| \leq a_{tol} + r_{tol} \cdot |b_{k+1}|$ is true.

¹⁷: It will default to the lower endpoint

In this chapter, we will focus on the aforementioned Community Firm Model, its inputs and outputs as well as how one can use it for different research directions. Next, the data from Kindler et al. [23] and the root finding algorithm for the first experiment Section 4.2 is introduced, along with how the algorithm can be sped up in Python. Finally, the two experiments and their scopes are presented, so that we are ready to continue.

The python files necessary to plot and run all experiments are found in: <https://github.com/Arcaru24601/CommunityFirnThesis.git>

3.1	The Community Firm Model	23
3.2	Data	32
3.3	Root finder	35

3.1 The Community Firm Model

The Community Firm Model (CFM) was designed to two key issues in the Firm modelling community. The first was to obtain a unified framework for firn ice modelling instead of many disjointed modelling schemes. The second was to develop a model, which could couple firn densification together with heat and firn air diffusion.

The CFM is designed to be a modular firn evolution framework to accommodate different research directions. Its most basic task is to predict depth-density and depth-age profiles for the firn, but using the accompanying configuration file, the CFM can simulate heat diffusion, meltwater percolation and refreezing, water isotope diffusion, firn air diffusion and grain growth[62].

The Community Firm Model is implemented for Python 3 and runs on versions higher than 3.6. This thesis uses CFM version 1.1.10. The CFM has since been updated to version 2.0, but this version change only affects surface energy balance, Enthalpy diffusion and the Morris densification scheme, neither of which are important for this thesis.

3.1.1 Overview of model calculations

The CFM uses a one-dimensional Lagrangian or material following grid, whereupon each output variable is calculated. The firn core can then be thought of as many model volumes, where each cell is a layer of the firn with uniform properties such as density, depth, temperature etc. At each time step, a new layer is added at the top of the firn column as a new cell and one cell is removed at the bottom. In each layer the density is calculated explicitly:

$$\rho_{\text{new}} = \rho_{\text{old}} + \frac{d\rho}{dt} dt \quad (3.1)$$

where the change in density through time is assumed to be a function of the temperature T , accumulation rate \dot{b} and current density ρ :

$$\frac{d\rho}{dt} = f(T, \dot{b}, \rho)$$

Here f is a placeholder function for a densification scheme such as the ones in [Subsection 2.2.2](#). Many densification schemes use the accumulation rate as a proxy for the overburden stress from the layers above. Since the accumulation rate is constant for a layer at depth z , the stress is then $\sigma(z) = \dot{b}g\tau(z)$, where g is the gravitational acceleration and $\tau(z)$ is the age of the firn for the current layer¹. For schemes forced with the accumulation rate instead of stress, the CFM will then use the mean accumulation rate \dot{b}_μ over the lifetime of a cell rather than the instantaneous at a given time step. In their study², Li et al. [106] found that using instantaneous accumulation rates would lead to no densification for zero accumulation rate, which is not realistic. The CFM includes the option of switching between mean and instantaneous accumulation rates since the schemes might not have been developed with this in mind. Furthermore, the diffusion of both firn air and heat is solved using a fully implicit finite-volume scheme from Patankar [77].

1: τ is also used for the tortuosity of the firn, but since Stevens et al. [62] used $\tau(z)$ for the depth, we will also use it here.

2: Here they also developed a densification model for surface elevation changes. It is also included in the CFM

3: It is possible to also specify other variables such as surface density

Finally, the CFM can be configured using a .JSON formatted file, which details model specifications for each run. In addition, the CFM requires input files for at least the temperature and accumulation rate³, which should be .csv files and contain the relevant variables at the respective time steps. Here, we use a setting in the .JSON file timesetup: "interp" (short for interpolation), where we only need to specify the variables at time steps, where there is a change in the inputs. This is then interpolated onto the model time domain using the number of years and time steps. A short example on the .csv files is found in [Table 3.1](#) and an overview of common configuration settings is included in [Appendix A](#).

Table 3.1: Example input forcing file for temperature and accumulation for accumulation/temperature curve in time for a ramp signal lasting 50 years with a spin-up time of 1000 years.

Time steps [yr]	1000,	1250,	1300,	1400
Temperature forcing [K]	232,	232,	242,	242
Time steps [yr]	1000,	1250,	1300,	1400
Accumulation [m ice eq./yr]	0.19,	0.19,	0.19,	0.19

A model run of the CFM constitutes a spin-up run and a main run, although there are differences between the two runs they can be summarized in the following:

- ▶ Initialize firn column
- ▶ Evolve firn column with main run physics
- ▶ Save final time step of time evolution in .hdf5

We will now go through each type in the following sections and their computation flows can be seen in [Figures 3.1](#) and [3.2](#).

Spin-up run

The spin-up run initializes a firm column with a specific number of volume elements specified by the firm column depth, accumulation rate and time steps from the `.json` file⁴:

$$N = \frac{H - H_{\text{baseSpin}}}{b_{\text{dot}}\theta / \text{stpsPerYear}} \quad (3.2)$$

where H is the thickness of the ice sheet, normally set to be 3 km, H_{baseSpin} is the depth of the initial firm column, $b_{\text{dot}}\theta$ is the mean or first element in the accumulation forcing in meters ice eq. and stpsPerYear is the number of time steps per year to define the model time domain, see [Appendix A](#).

During the first time-step, the spin-up run uses the Herron and Langway analytical model to quickly calculate steady-state density, age and depth profiles from the initial or mean entry of the input forcing, depending on setting `spinup_climate_type`. In the time-evolve loop (see [Figure 3.1](#)), the density and age profiles are now calculated with a user-chosen densification scheme from the i 'th forcing entry in the `.csv` input files.

Here, it is also possible to couple the firm densification model with heat diffusion by using the heat diffusion module (`"HeatDiff": true`). This is done using the finite volume method of Patankar [77] on the differential equation with a thermal conductivity as prescribed by Calonne et al. [107]. Note that, it is not possible to use firm air diffusion during the spin-up run. Presumably, this is done to save time in case the forcing files would lead to an unstable firm column, for which there would be no need to use the time-expensive `firm_air` module.

At the end of each time step, the firm column grid is updated with depth z , density ρ and age. At the last time-step, the spin-up run saves these variables in a `.hdf5` file `CFMspin.hdf5` that is then used by the main run.

Main run

Now that the firm column is stable and initialized, the main run begins. It functions exactly as the spin-up except that it is forced with varying temperatures, and accumulation rates among others with the `firm_air` module enabled (see [Figure 3.2](#)). The `gaschoice` setting allows the user to model stable nitrogen and argon isotopes in addition to CO_2 . Here, `gaschoice` is set to `d15N2` to model stable nitrogen isotopes. The module `solver.py` solves [Equation 2.34](#) once again through Patankar [77] with source term set by `"thermal": on` and `"gravitational": on`. In addition, the diffusivity and air advection parameterization as explained in [Subsection 2.2.4](#) can be set by `"Diffu_param": "Schwander"` and `"advection_type": "Darcy"`. The `firm_air` module, then outputs the concentration, gas age and the diffusivity of the chosen gas species in addition to the air and firm advection rate.

4: Due to the large size of the upcoming figures, they have been collected to their own group of pages, to not break up the text-block.

2019, Calonne et al.: 'Thermal Conductivity of Snow, Firm, and Porous Ice From 3-D Image-Based Computations'

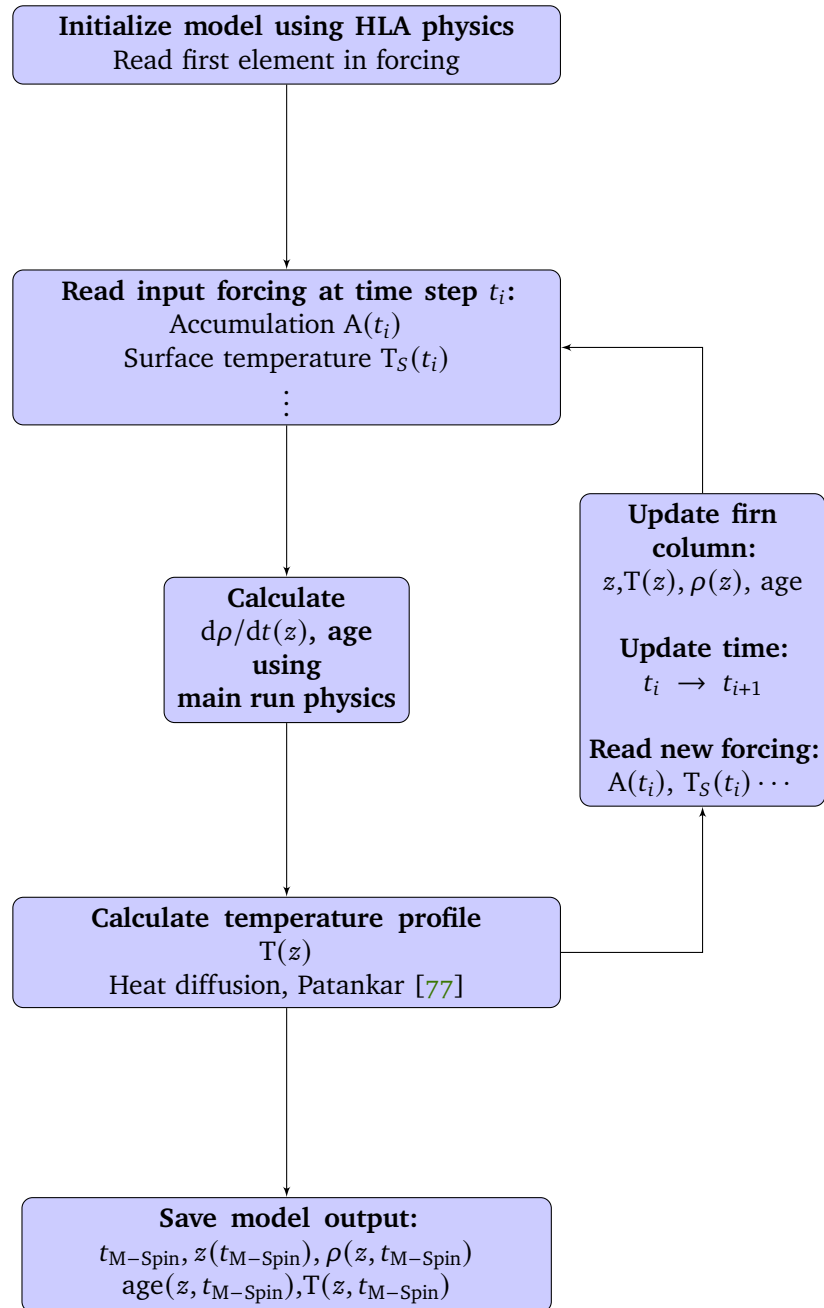


Figure 3.1: Computation flowchart of the Spin-up run for the CFM: Spin-up run is initialized using Herron and Langway Analytical model and then evolves using main run physics except for firn air model. The last time step is saved as initial input for the main run. Adapted from [25, 26]

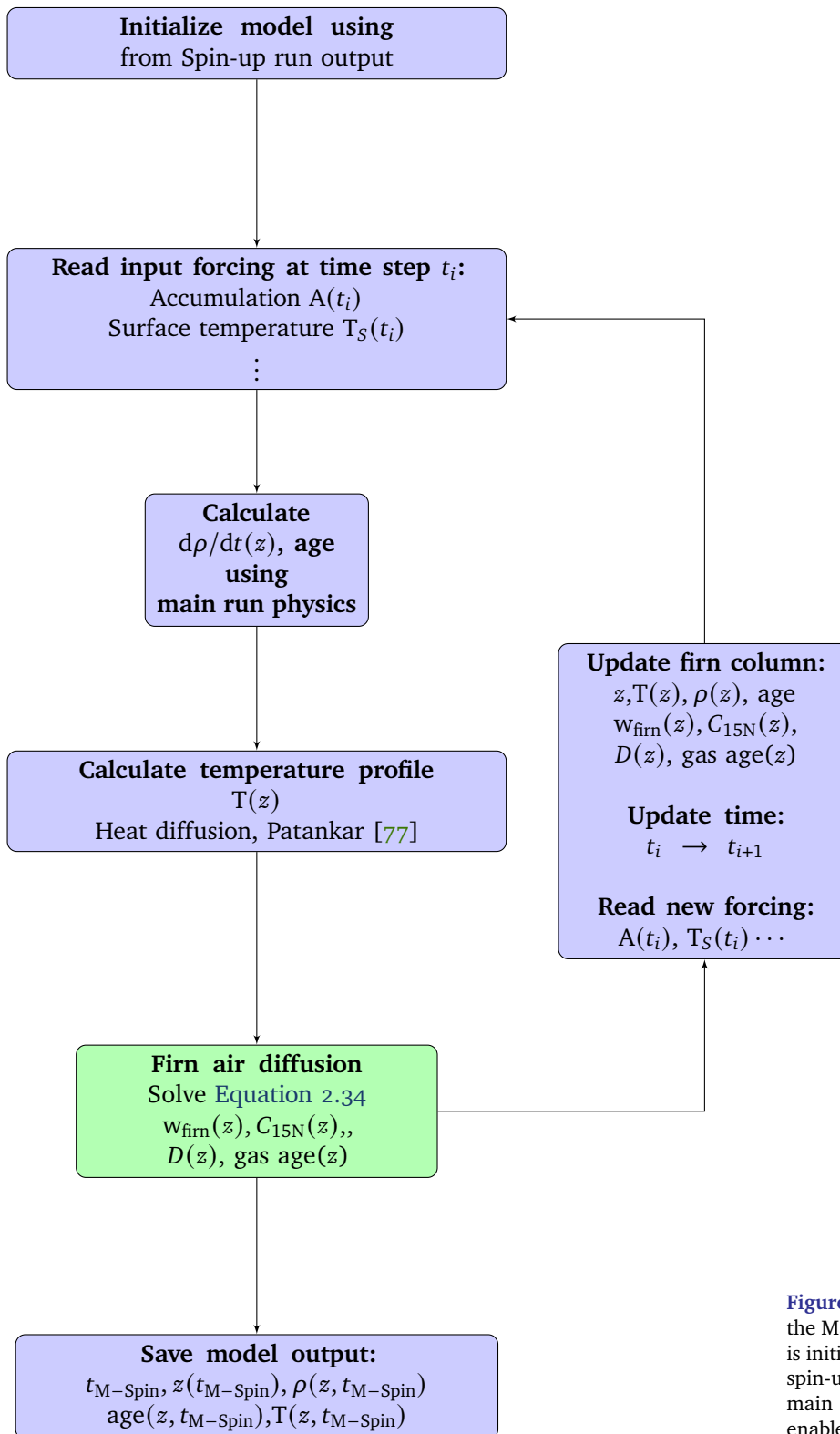


Figure 3.2: Computation flowchart of the Main run for the CFM: Main run is initialized using the final output of spin-up run and then evolves using main run physics with air diffusion enabled. [25, 26]

Outputs for the CFM

After the model run is complete, the CFM saves model outputs as specified by the user in the `.json` configuration file in a single `CFMresults.hdf5` file. In this thesis, the outputs saved are the following: "BCO", "Modelclimate", "d15N2", "density", "depth", "diffusivity", "forcing" and "temperature". These outputs are saved mostly as 2D matrices of size $N_{dt} \times N_{dz}$, while Model climate, forcing and BCO are 1D arrays with only the model time domain N_{dt} . While, it is possible to specify other outputs such as grain size, compaction rate, liquid water content etc. only outputs⁵ relevant are included, if for no other reason than to conserve storage and decrease computation speed. All output files contain a column with the model time values. The model climate contains the input temperature and accumulation rate interpolated onto the model time domain while forcing contains the raw input forcing from the `.csv` files⁶. BCO, short for Bubble Close-Off, contains multiple 1-D arrays and contains the age and depth of the following: Close-off, lock-in, 815 and 830 density horizons as well as the depth of zero open porosity. Here, the close-off and lock-in are calculated according to Equation 2.7 from Martinerie et al. [54].

5: It is not uncommon for the `.hdf5` files to reach sizes of 100-200 MB even with only the options specified above.

6: Regardless if one specified input rain and melt files, the forcing output will show these as "-9999".

Next, we will explore how these outputs behave in a DO-like signal, i.e., a short period of warming followed by a plateau and finally a long period of cooling. For simplicity, only temperature will change during the example in Figure 3.4, which shows typical outputs for the CFM. In the subplots, b, c and d, we see depth profiles for different time steps, while a, e and f show the time steps with vertical lines.

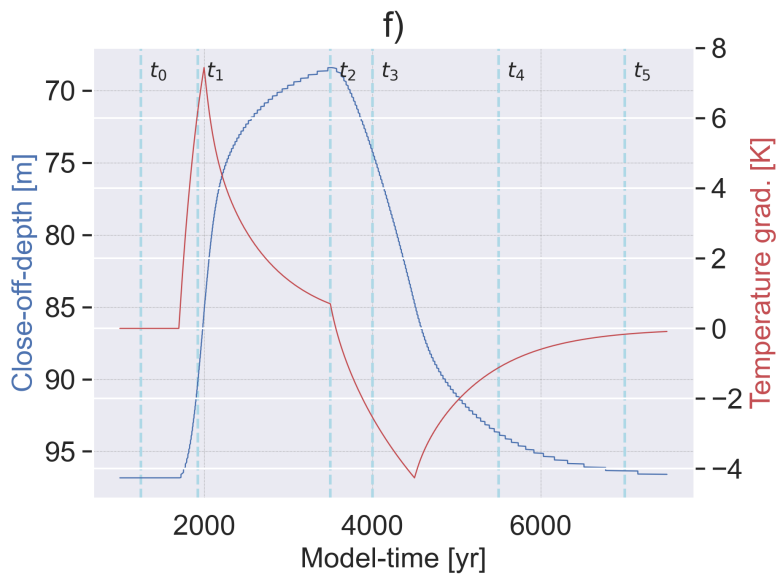
In Figure 3.4 b), we see the depth-density profile as it evolves. Visible is the characteristic kink in the profile due to the zone 1 to zone 2 densification at 550 kg m^{-3} . In addition, for higher temperatures, we reach a higher densification rate, while the opposite is true for lower temperatures. This relates to the Arrhenius activation energy theorem, since the ice matrix would have a higher amount of energy, leading to higher rates of crystallization.

The depth- $\delta^{15}\text{N}$ profile in c) shows several interesting phenomena. First, all profiles t_i have a linear dependence on depth during the initial part, starting from atmospheric values at $\delta^{15}\text{N} = 0$ until the close-off depth from which no change can continue. Since t_1 is before the temperature increase, only gravitational fractionation plays a role, which is linear in depth. For t_1 , we see an increased excursion of stable nitrogen isotopes at close-off due to the thermal fractionation caused by the positive temperature gradient (Also visible in e)). However, since higher temperatures equate to a shallower firn column due to increased densification rate, the subsequent time steps t_2, t_3 have a much lower abundance of $\delta^{15}\text{N}$. For t_4 , the temperature is back at the previous level, but equilibrium has yet to set in leading to a higher abundance than t_3 , but lower than t_0 . Finally, t_5 has reached equilibrium again, as it is very similar to t_0 .

In both c) and e), $\delta^{15}\text{N}$ drops to 0 ‰ deep in the firn. The cause of this lies in the firn air initialization during the main run, where the $\delta^{15}\text{N}$ matrix is initialized as ones. It is hereby necessary for the CFM

to run until such a time that $\delta^{15}\text{N}$ has diffused and advected down to the close-off depth and beyond in the ice-matrix⁷. In d), we see the depth-temperature profile, showing that a significant time needs to pass before equilibrium is reached. Finally, in f), we see the evolution of close-off depth with time, which looks like a smoothed version of the temperature forcing in a). This again relates to the dependence of close-off depth to temperature due to the densification rates.

In Figure 3.3, the temperature gradient between the surface and close-off depth is plotted together with the close-off depth. Due to an unknown bug with Python regarding the figure size, this is plotted separately from Figure 3.4. Here, we observe that at t_2 , the close-off depth reacts quickly to the change in the temperature forcing. Additionally, we see the same behaviour, where the temperature gradient is not symmetric in amplitude for warming and cooling, as seen in Figure 2.8.



7: Since we are focused on physics above the close-off depth, this time is almost instant as seen in e).

Figure 3.3: CFM Close-off depth plotted with temperature gradient. See Figure 3.4

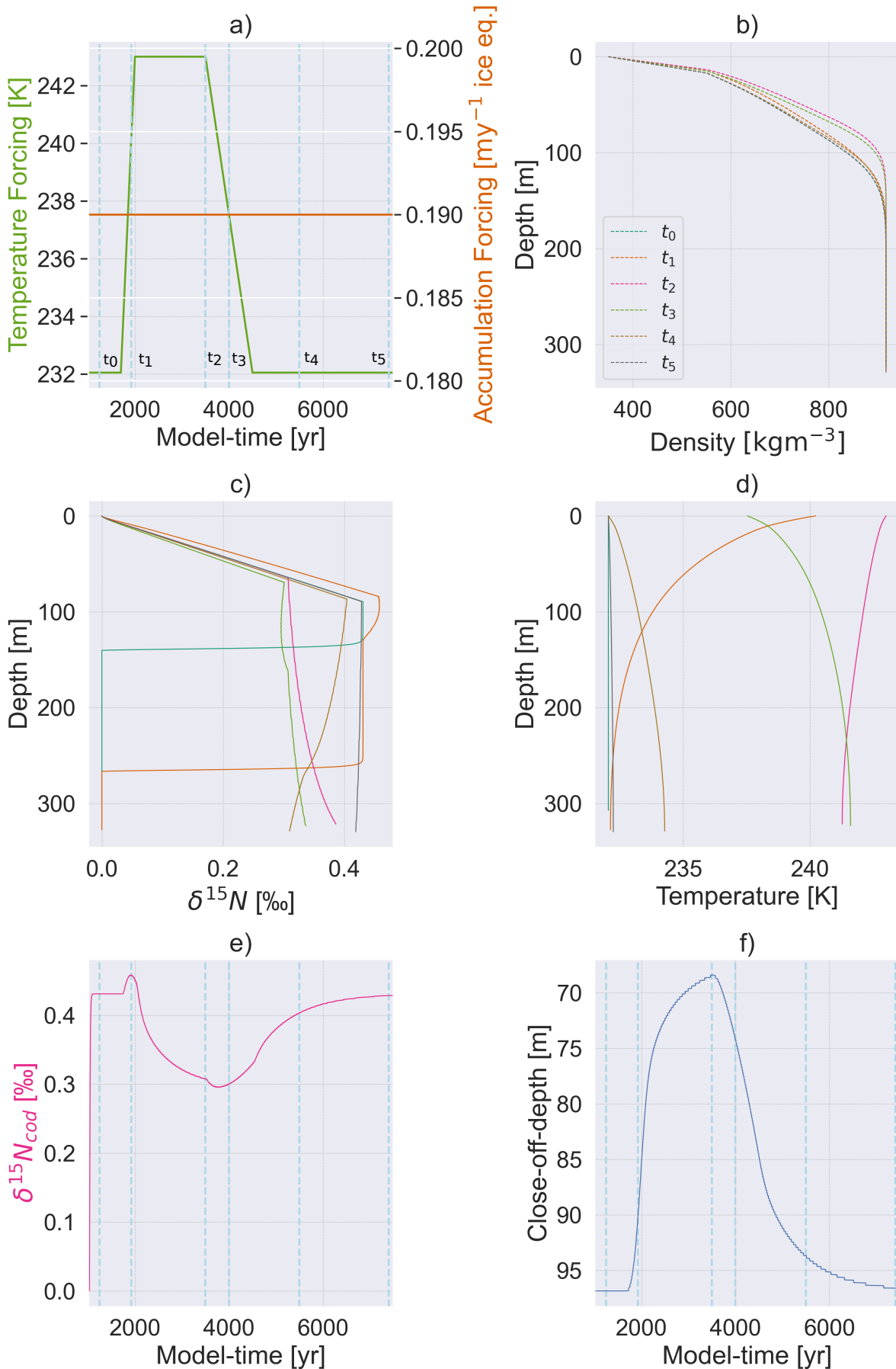


Figure 3.4: Typical CFM outputs with densification model Barnola and firm air enabled. Vertical cyan lines mark time steps t_i where $t_i \in [1249, 1924, 3499, 3999, 5499, 7399]$ in years. a) Surface temperature and accumulation rate input forcing, b) depth-density profile for different time steps t_i , c) depth- $\delta^{15}\text{N}$ profile, the artefact for t_0, t_1 is due to firm-air initialization during the main run, d) depth-temperature profile, e) abundance of stable nitrogen isotopes at close-off with the same artefact present and f) evolution of close-off depth with time.

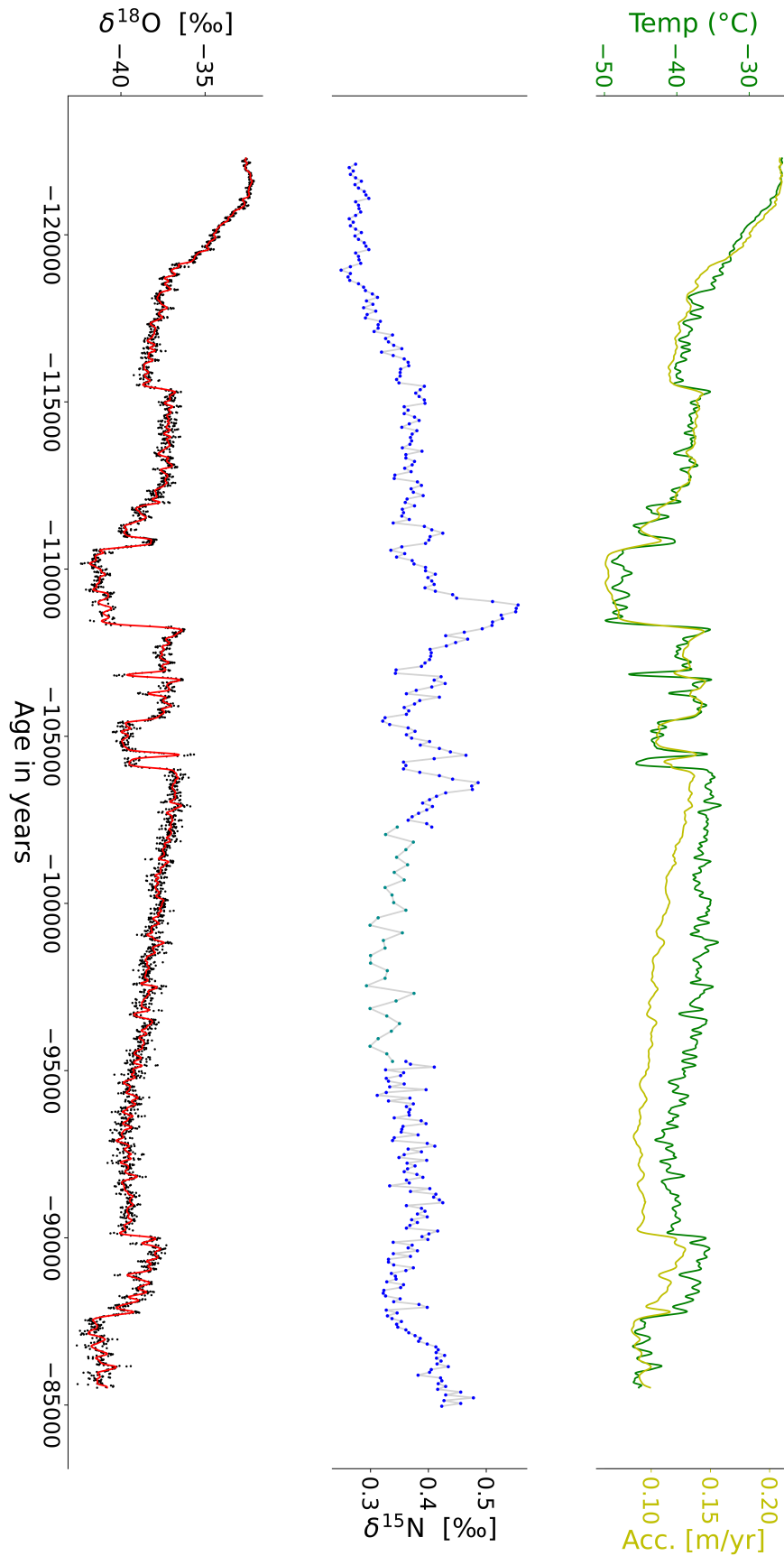


Figure 3.5: Dataset from NGRIP Kindler et al. [23], 120 to 85 kyr b2k. In yellow accumulation rate in m/yr ice eq. as found by Kindler et al. [23]. In teal, the temperature reconstruction by [23] using ice-core data together with a firm densification model coupled with heat diffusion. Blue points are $\delta^{15}\text{N}$ on a gas age scale as measured by ● [108, 109] and ● by [23]. Black points are $\delta^{18}\text{O}$ on the ice age scale, while the red line is a cubic smoothing spline with a cut-off frequency $1/200 \text{ yr}^{-1}$. Adapted and modified from [23, 26].

3.2 Data

In this section, we will introduce the source of the data that the experiments are based on. Note that, due to a time reevaluation, we are only considering steady-state temperature reconstruction and not transient inversion. We will therefore only use some data in the following section, however, due to the inter-connectedness of the data, it is necessary to give a brief introduction to each component. Due to the large size of the figure, we have elected to show one figure in the main text and the rest in the appendix.

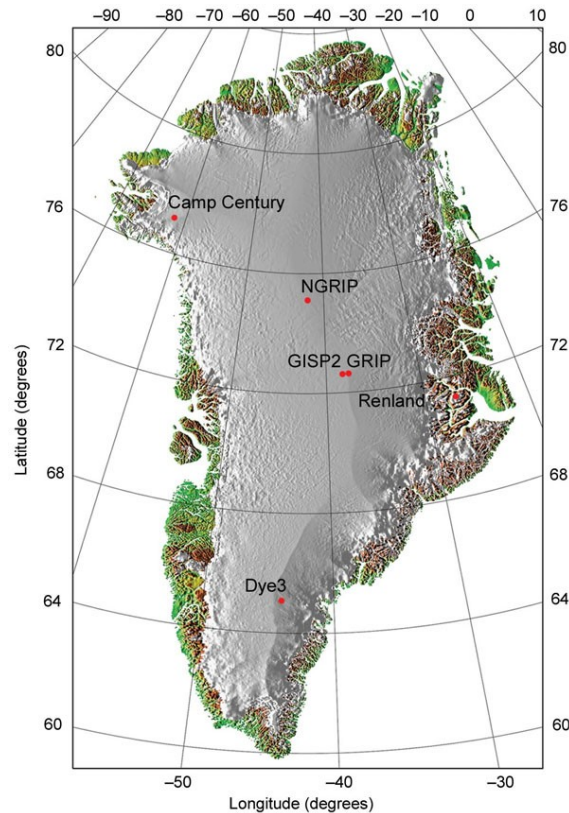


Figure 3.6: Map over Greenland with the location of NGRIP and other important ice core sites. Adapted from NGRIP members [14]

2004, NGRIP members: ‘High-resolution record of Northern Hemisphere climate extending into the last interglacial period’

8: Kilo-years before 2000

To reconstruct past temperature histories from the surface of Greenland, we use ice-core measurement data from NGRIP members [14] by Kindler et al. [23]. The NGRIP site was chosen due to a desire to avoid ice folding at bedrock, as had been the case for GRIP and GISP2. Therefore, a new site was proposed at 72.10 °N and 42.32 °W which featured, among others, the following geographical conditions[14]:

- ▶ Ridge position reducing ice flow deformation
- ▶ A flat bedrock topography
- ▶ A lower precipitation rate compared to the previous sites

The NGRIP site hereby covers a time period from 10 to 120 kyr b2k⁸ at an elevation of 2917 m and ice thickness H of 3085 m.

The time chronology system for the datasets is the Greenland Ice Core Chronology 2005 Extension[110] (GICC05ext) and GICC05. These are based on annual layer counting, where the GICC05 reaches down to 60.2 kyr b2k. For depths deeper than 60.2 kyr, the GICC05 is extended

with the timescale developed for GRIP by NGRIP members [14] and Johnsen et al. [111] *ssogseao6bm*[112–116], which is shifted 705 years to younger ages⁹.

9: Is- [117] states that caution should be taken due to the way it was extended

3.2.1 Nitrogen data

The dataset from Kindler et al. [23] is a composite set containing data from many research groups at the Climate and Environmental Physics Division (KUP) of the Physics Institute at the University of Bern (Holocene to DO17) [23, 41] and from Laboratoire des Sciences du Climat et de l'Environnement (LSCE), Gif-sur-Yvette (DO18 to DO25) [108, 109, 118–120]. In both cases, Isotope Ratio Mass Spectrometry (IRMS) is used to determine the abundance of $\delta^{15}\text{N}$ in the air bubbles found in the ice cores. Uncertainties in stable nitrogen isotopes for KUP were reported at ± 0.02 permil, while they were ± 0.006 permil for LSCE. As a handy overview, the specific DO events, approximate ages, laboratory and uncertainty have been collected in the following table:

Period	Lab.	σ ‰
DO0 - DO8	KUP[23]	0.02
DO8 - DO17	KUP[41]	0.02
DO18,19, 20	LSCE[118]	0.006
DO21	LSCE[119]	0.006
DO22	LSCE[120]	0.006
DO23, 24	LSCE[108]	0.006
DO25	LSCE[109]	0.006

3.2.2 Temperature reconstruction

In their temperature reconstruction, Kindler et al. [23] exploited the correlation mentioned previously in Equation 2.2 with a slight modification:

$$T = \frac{\delta^{18}\text{O}_{\text{ice}} + 35.1[\text{‰}]}{\alpha} + 241.6[\text{K}] + \beta, \quad (3.3)$$

where 35.1 permil and 241.6 K are NGRIP Holocene values [14] and α, β are temperature- $\delta^{18}\text{O}_{\text{ice}}$ -sensitivity and shifts respectively. To reduce the effect of noise on the model output, Kindler et al. [23] employed a cubic smoothing spline. To be specific, the $\delta^{18}\text{O}_{\text{ice}}$ data from the *ssogseao6bm* was splined with cut-off frequency of $f_{\text{cop}} = 1/200\text{yr}^{-1}$ years, i.e., any event with frequencies higher than f_{cop} are filtered out. The temperature reconstruction by Kindler et al. was done using a firn densification scheme coupled with heat and gas diffusion, formulated by Schwander et al. [121]. Using this model, they computed stable nitrogen gas isotope distributions, which they could then fit the ice core data by varying α, β and the accumulation rate. The $\delta^{18}\text{O}_{\text{ice}}$ -dataset can also be accessed from [117].

Table 3.2: Overview of laboratory measurements for $\delta^{15}\text{N}$ for NGRIP and their corresponding uncertainties. Adapted from Kindler et al. [23].

3.2.3 Accumulation rates

The accumulation rate data can be recorded based on the thickness of each layer in the ice core. In their paper, Kindler et al. used accumulation rates from the *ssogseao6bm* time-scale, since this ensured full coverage from 62-120 kyr b2k. However, during their temperature reconstruction, it was necessary to adjust the accumulation rate data by varying levels, so that the modelled $\delta^{15}\text{N}$, Δdepth and Δage would match the experimental values. For example, in the period 12 to 64

kyr b2k, the accumulation rate was reduced by 20 to 30 % [23, p. 73-74].

3.2.4 Setup for Experiment 1

Here, we prepare some data for use in the first experiment, where we test the steady-state sensitivity of the CFM. Inspired by previous studies (Gkinis et al. [25], Johnsen et al. [39], and Dahl-Jensen et al. [122]), we assume a logarithmic relationship between the accumulation rate and the surface temperature, i.e., that:

$$\ln A = -a + bT, \quad \text{or} \quad A = e^{-a+bT} \quad (3.4)$$

It should be noted that this temperature-accumulation relationship is a qualitative one and therefore not representative of real ice-sheet conditions. It is nevertheless very useful for generating somewhat realistic input forcing for use in the experiments. To find the parameters a and b , we employ orthogonal distance regression, implemented in Scipy as `scipy.odr`. This was chosen in lieu of other choices, since other methods like `scipy.curve_fit` couldn't estimate the covariance matrix. As a starting guess for the fit, we used the parameters described by Gkinis et al. [25], where:

$$a = 21.492, b = 0.0811 \quad (3.5)$$

After fitting the accumulation rates to the reconstructed surface temperatures reported by Kindler et al. [23], we arrive at the following parameters and standard deviation:

$$a = 18.823, \sigma_a = 0.098, b = 0.0701, \sigma_b = 0.0004 \quad (3.6)$$

In Section 4.1, this will be used as the basis for the forward model runs, to complete the sensitivity experiments in Section 4.2. The result of `scipy.odr` are plotted in Figure 3.7, where the red points are pairs of temperature and accumulation rate, while the intersecting line is the function $A(T) = \exp(a + bT)$.

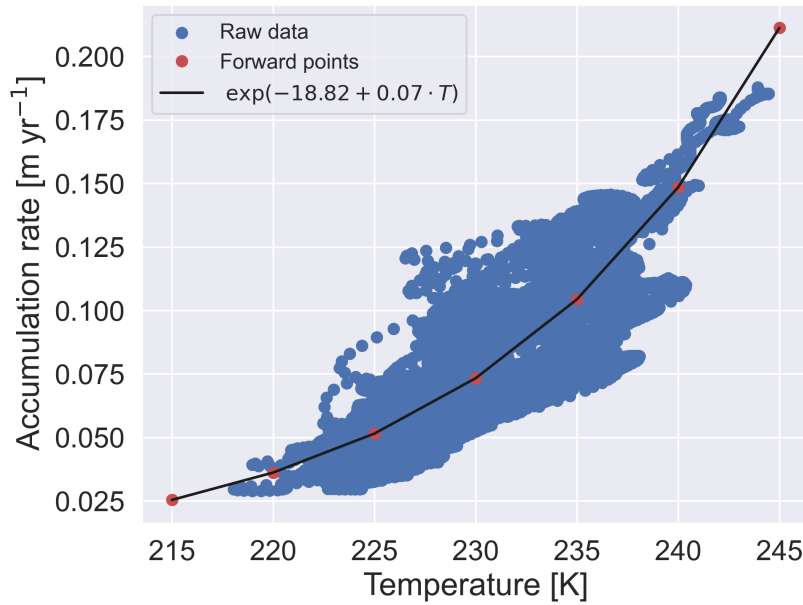


Figure 3.7: Accumulation rates fitted to reconstructed surface temperatures from Kindler et al. with an exponential function of the form $A(T) = \exp(-a + b \cdot T)$. Here a, b are equal to 18.82 and 0.07 K^{-1} . Inspired by [25, 39, 122]

3.3 Root finder

Steady-state temperatures are reconstructed from $\delta^{15}\text{N}$ values by inverting the Community Firn Model with Brent’s method from the `scipy.optimize` library. Here, we draw the value $\delta^{15}\text{N}_{i,\text{ref}}$ from a normal distribution of $\mathcal{N}(\delta^{15}\text{N}_{j,\text{mu}}, \sigma_{\delta^{15}\text{N}})$, where the mean is obtained from a forward model run with the CFM with inputs $T_{i,\text{ref}}, A_{i,\text{ref}}$ as detailed in Section 4.1. The reference accumulation input is saved for all i repetitions to ensure that the problem is stable and converging.

The main input parameters for the root finder are a function f to be minimized and a reference value for the abundance of $\delta^{15}\text{N}_{i,\text{ref}}$. Here, the function f takes an input temperature guess between T_{min} and T_{max} , and saves it as `input_temp.csv`. It then runs the CFM with these inputs and outputs `CFMresults.hdf5` to be analyzed. The module `read_model_data` is implemented, which crucially outputs the abundance of stable nitrogen isotopes at close-off depth by solving the firn air transport Equation 2.34. The function f calculates a cost function defined as the deviation between the model and reference $\delta^{15}\text{N}$ as $\delta^{15}\text{N}_{i,\text{model}} - \delta^{15}\text{N}_{i,\text{ref}}$, which serves as the primary output. As a failsafe, if the CFM has crashed and as such no `CFMresults.hdf5` exists, then the cost function is set to 100. This can happen in cases where the close-off depth exceeds the firn column domain of 300 meters, which can happen for very low temperatures and accumulation because the firn layers become very thick. Therefore, since there is no depth equal to the computed close-off depth, `read_model_data` cannot compute $\delta^{15}\text{N}_{\text{cod}}$.

The root finder then exploits the `brentq` module as explained in Section 2.3 to find the temperature that satisfies the tolerance criteria set by x_{tol} and r_{tol} or if the number of iterations exceeds a maximum allowed number. If any of these are fulfilled, then the root-finder stops iterating and a dictionary is saved as a `Point_i.h5` file. This dictionary contains among others the number of iterations, stable nitrogen

ro: Note, that since we are in steady-state, the temperature is constant throughout the firn column

abundance and temperature at close-off¹⁰. This is then repeated for the total M repetitions desired, where $\delta^{15}\text{N}_{i,\text{ref}}$ is changed between each repetition.

Beyond uncertainty in stable nitrogen isotopes, one can also investigate the effect of noisy surface densities and effective diffusivity parameterization. The function `apply_noise` takes several boolean variables, deciding if each uncertainty source should be used or not. In the case of surface densities, we draw $\rho_{i,s}$ from $\mathcal{N}(330, 20)$ where the units are kg m^{-3} , while for effective diffusivity we select a random element from a list containing all parameterizations from [Subsection 2.2.4](#). The configuration files `FirnAir_Opti.json` and `Air_config.json` are configured for "rhos" and "bco_dist". Note that, if scenarios with different uncertainties are sequential, care must be taken to reset all configuration files between each run. The function `reset_to_factory()` is implemented, which simply resets the surface density and diffusivity parameterization to 350.0 kg m^{-3} and "schwander" respectively, as all forward model run were computed with these settings.

Finally, we run each scenario in a specific process instance, which as explained in [Subsection 3.3.1](#) employs a single CPU core for each task. We assign each process with a unique parameter `file_id`, which causes all IO-operations to access configuration, input and output files with the same `file_id`. This way, we avoid any issues of different processes accessing a file out of turn. For instance, given two simulations of the following form $S(\sigma_{\delta^{15}\text{N}}, \sigma_{\rho_s}, \sigma_{D_{\text{eff}}})$ where each variable is either true or false. Then a simulation with only uncertainty in stable nitrogen isotopes $S(\text{True}, \text{False}, \text{False})$ could access files pertaining to a simulation $S(\text{True}, \text{True}, \text{False})$, which would conflict with the goal of the simulation.

3.3.1 Speeding up the computation: Multiprocessing

Python processes are normally restricted to using only one CPU core through the global interpreter lock (GIL). Here, only one Python thread can access the Python interpreter at a time. This creates a severe limit for long-running simulations of multiple scenarios since each process has to be finished in sequence before the next. We overcome this with the Multiprocessing package in Python, which assigns a Python interpreter, memory and GIL to each process. If a laptop, for instance, has a CPU of 4 cores, then we would be able to simulate three (four) different scenarios concurrently¹¹.

Note, that this is different from multithreading, where the threads share memory enforcing the GIL. This is why the two are suited for different tasks, for CPU-bound tasks multiprocessing is better while multithreading suits IO-bound jobs more. In the first experiment, we carry out maybe a dozen IO operations depending on configuration and significantly more CPU calculations. The same is true for the second experiment, and so multiprocessing is much more suited for our purposes.

¹¹: We limit ourselves to $N - 1$ cores to maintain one core for system-related tasks and overhead

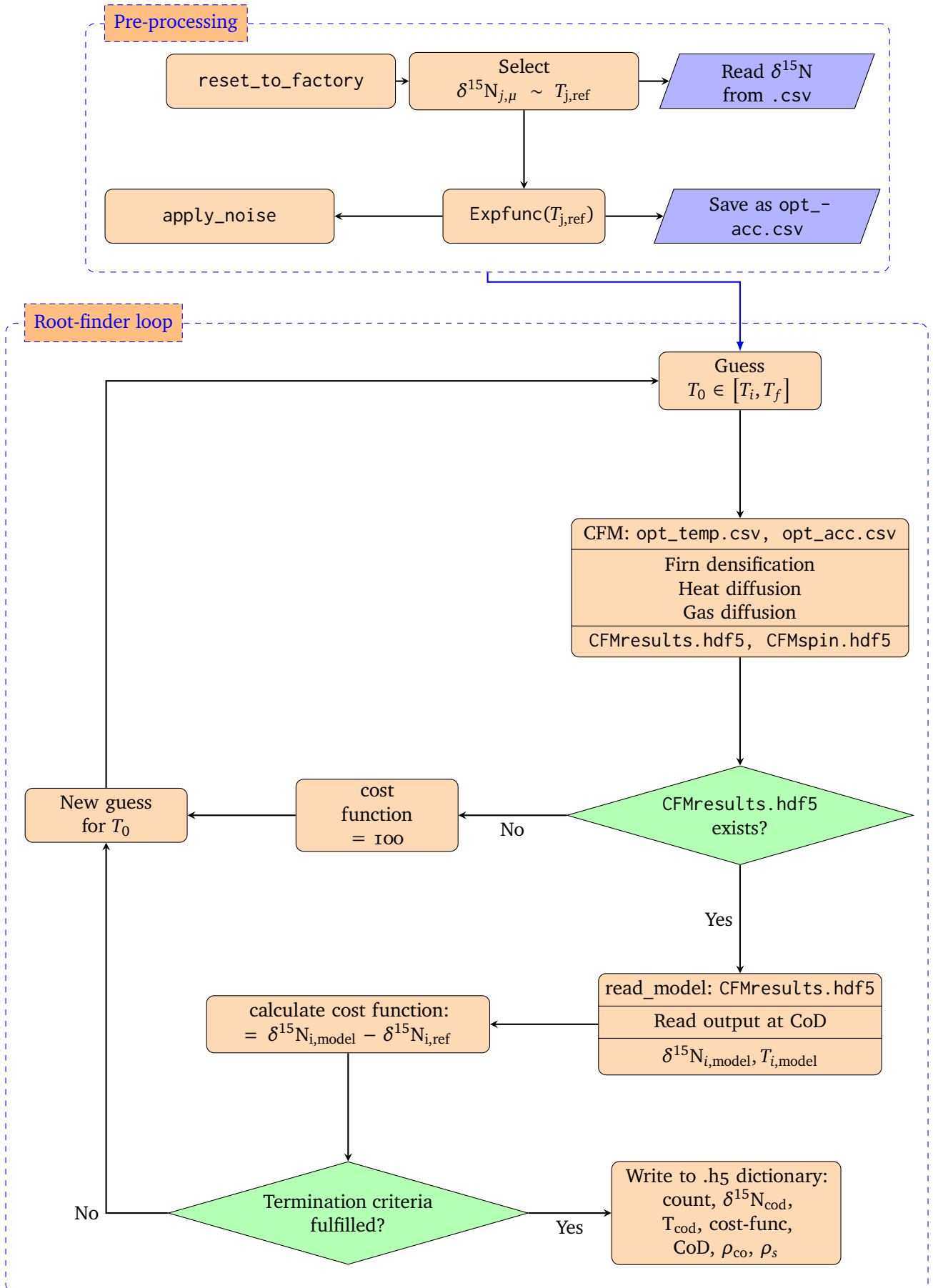


Figure 3.8: Computation flowchart for the rootfinder, `apply_noise()` creates a distribution for $\delta^{15}\text{N}$, ρ_s , D_{eff} .

This project aims to better understand the transition to the Holocene period, 12000 years ago. First, the sensitivity of the Community Firn Model is probed in a steady state for uncertainty in various quantities and parameterizations. Second, we investigate how the firn column reacts to systematic changes in input forcing and compare the responses to data from NGRIP. Hereby, we present three things for each experiment: What we are doing, how we are doing it and why we are interested in the experiment. The discussion and results will be left to [Chapter 5](#).

4.1	Steady state: Forward model runs	39
4.2	Steady state: Temperature sensitivity	39
4.3	Response to changing duration and magnitude of input forcing	40

4.1 Steady state: Forward model runs

The steady-state sensitivity experiment is made of two phases: A forward model run and then sensitivity tests. We conduct these forward model runs to generate the input $\delta^{15}\text{N}$ values for use in the second phase. In addition, the goal of the first phase is to compare the agreement or deviation between different densification models and diffusivity parameterizations in the abundance of stable nitrogen isotopes. This knowledge will be crucial in interpreting the results seen in the second phase, both regarding temperature and model dependence. The surface temperature and accumulation rates are drawn from [Figure 3.7](#) using the highlighted (T_i, Acc_i) pairs. We then run the CFM with the firn-air module enabled for 1000 years with a 1000-year spin-up run. The chosen surface density is 350.0 kg m^{-3} .

- ▶ Fit NGRIP[23] accumulation rates to reconstructed temperatures
- ▶ Run CFM forward for Temp/Acc pairs and output $\delta^{15}\text{N}_{\text{cod}}$ for densification model HLD, HLS, BAR and GOU.
- ▶ Repeat the above, but for all diffusivity parameterizations.

4.2 Steady state: Temperature sensitivity

The goal of this experiment is twofold. First, we study how different densification models behave, when reconstructing temperatures from noisy data, specifically stable nitrogen isotopes. Secondly, we test how uncertainty in $\delta^{15}\text{N}$, surface density, diffusivity parameterization etc. affect the sensitivity of the reconstructed temperatures. As mentioned in [Section 3.3](#), we use the root finder implemented in `Steady_state.py` to perform the inversion procedure by employing the `brentq` method from `scipy.optimize`. The reference temperature and $\delta^{15}\text{N}$ are a result of forward model runs on temperature accumulation pairs obtained from the NGRIP data. In addition, the distribution for the surface density is Gaussian with a mean and

standard deviation of 330 kg m^{-3} and 20 kg m^{-3} from the general $300\text{-}350 \text{ kg m}^{-3}$ range [23, 62]. The workflow for the experiment can be summarized to:

- ▶ Draw $\delta^{15}\text{N}_{\text{ref}}$ from $\sim \delta^{15}\text{N}_{\text{cod}} \pm 3\sigma \cdot \mathcal{N}(0, 1)$
- ▶ Add uncertainty in chosen quantities, e.g., ρ_s, D_{eff}
- ▶ Invert $\delta^{15}\text{N}_{\text{ref}}$ with Brent's method[103] for M repetitions

4.3 Response to changing duration and magnitude of input forcing

The objective of the second experiment is to quantify the time elapsed after a change in input forcing before a new equilibrium point is reached (assuming no further changes).

1: Taken between the surface and close-off depth

To that end, we force the CFM with an input ramp signal with different amplitudes and durations for the four densification HLD, HLS, BAR and GOU. Here, the relevant outputs are the close-off depth, temperature gradient¹ and $\delta^{15}\text{N}_{\text{cod}}$. Next, we find the so-called halfway equilibrium time for the close-off depth and temperature gradient as a means of estimating the true equilibrium time. In this thesis, this is taken to mean the halfway time from the end of the ramp signal to the equilibrium point. For the stable nitrogen signal, we merely identify the time for which, $\delta^{15}\text{N}_{\text{cod}} \leq 0.006$ as this would be below the lowest measurement uncertainty as reported from Kindler et al. [23].

This is done for two scenarios, wherein only the magnitude or the duration of the forcing signal can change. Both of these scenarios are computed for changes in temperature, accumulation rate and both. The “baseline” change is a duration of 300 years, a warming of 10 degrees Kelvin and an increase of 0.075 m water eq. in accumulation. In the case, where both forcings are changed, the accumulation rate is adjusted through Equation 3.4

In the first scenario of changing duration, we make 28 iterations, where the duration changes from 10 to 2000 years. This range consists of 8 values between 10 and 100 years and 20 linearly spaced values from 100 to 2000 years. This is done to illuminate the general length of the warming signal in a DO event. Secondly, we change the magnitude of the forcing signal by increasing the change with a factor linearly spaced between 1/3 and 3 in 28 iterations.

4.3.1 Addendum: Equilibrium time

Our use of the halfway time instead of the true equilibrium arose from a problem earlier in the thesis. We defined the equilibrium time as the first time for which the selected variable was constant. This presented a new question: How high should the tolerance be? Of course, using different tolerances for constancy yields distinct results.

So, the halfway time was developed as a stop-gap measure, since it was easier to code and required no reliance on a tolerance.

However, a new opportunity has arisen. As explained earlier, we use the measurement uncertainty in $\delta^{15}\text{N}$ from Kindler et al. [23] to find the equilibrium time for stable nitrogen isotopes. If we could find similar measures for the temperature gradient and close-off depth, we would have a way of estimating the true equilibrium time². For the close-off depth, we choose to use the CFM depth resolution as this uncertainty, as it was the most readily available. Unfortunately, there is no way to measure the temperature gradient directly from thousands of years ago. Despite that, there is a way to estimate the temperature gradient in addition to the uncertainty. Recall, that the CFM can simulate both stable nitrogen and argon isotopes and from Subsection 2.2.3 that gravitational fractionation is discriminatory against isotope mass. We can then calculate the so-called $\delta^{15}\text{N}_{\text{exc}}$ or the excess in stable nitrogen isotopes, defined as:[123]

$$\delta^{15}\text{N}_{\text{exc}} = \delta^{15}\text{N}_{\text{tot}} - \frac{1}{4}\delta^{40}\text{Ar}_{\text{tot}} \quad (4.1)$$

And since the gravitational fractionation of argon is four times higher than of nitrogen:

$$\begin{aligned} \delta^{15}\text{N}_{\text{exc}} &= \left(\delta^{15}\text{N}_{\text{grav}} + \delta^{15}\text{N}_{\text{th}}\right) - \frac{1}{4}\left(4\delta^{15}\text{N}_{\text{grav}} + \delta^{40}\text{Ar}_{\text{th}}\right) \\ &= \Omega_{\text{N}}\Delta T - \frac{1}{4}\Omega_{\text{Ar}}\Delta T = \left(\Omega_{\text{N}} - \frac{1}{4}\Omega_{\text{Ar}}\right)\Delta T \end{aligned}$$

Then the temperature gradient is simply

$$\Delta T = \frac{\delta^{15}\text{N}_{\text{exc}}}{\Omega_{\text{N}} - \frac{1}{4}\Omega_{\text{Ar}}} = \frac{\delta^{15}\text{N}_{\text{tot}} - \frac{1}{4}\delta^{40}\text{Ar}_{\text{tot}}}{\Omega_{\text{N}} - \frac{1}{4}\Omega_{\text{Ar}}} \quad (4.2)$$

In addition, the thermal diffusion factor for Argon was found by Grachev et al. [124] to be:

$$\alpha_{\text{Ar}} = 26.08 - \frac{3952}{T_{\text{mean}}} \quad (\pm 1\%) \quad (4.3)$$

This results in a thermal sensitivity coefficient for ^{40}Ar at an average temperature of $-30\text{ }^\circ\text{C}$ in the CFM[62] at $39.4 \cdot 10^{-3}\text{ }^\circ\text{C}$. Finally, the measurement uncertainty for $\delta^{40}\text{Ar}$ as done by Morgan et al. [125] to be 8 permeg or 2 permeg for $\delta^{40}\text{Ar}/4$. However, we will be using a more conservative value of $\sigma_{\text{Ar}_{\text{tot}}} = 6$ permeg as older studies such as Kobashi et al. [126] reported higher uncertainties.

We can then employ the error propagation formula to find the estimated uncertainty based on the error sources[108, 109, 118–120] of $\delta^{15}\text{N}$ and $\delta^{40}\text{Ar}$ being respectively $\sigma_{\text{N}_{\text{tot}}} = 6$ permeg and $\sigma_{\text{Ar}_{\text{tot}}} = 6$ permeg:

$$\sigma_{\Delta T} = \sqrt{\left(\frac{\partial \Delta T}{\partial \text{N}_{\text{tot}}}\right)^2 \sigma_{\text{N}_{\text{tot}}}^2 + \left(\frac{\partial \Delta T}{\partial \text{Ar}_{\text{tot}}}\right)^2 \sigma_{\text{Ar}_{\text{tot}}}^2} \quad (4.4)$$

2: This is just the same as using the earlier method, but using the uncertainty as the threshold

This is then

$$\sigma_{\Delta T} = \sqrt{\frac{\sigma_{N_{\text{tot}}}^2}{\left(\Omega_N - \frac{1}{4}\Omega_{\text{Ar}}\right)^2} + \frac{\sigma_{\text{Ar}_{\text{tot}}}^2}{\frac{1}{4^2}\left(\Omega_N - \frac{1}{4}\Omega_{\text{Ar}}\right)^2}} = 1.275 \text{ K } (\pm 1\%) \quad (4.5)$$

The error in the thermal sensitivities mentioned earlier of ($\pm 1\%$) for Argon and ($\pm 3\%$) for Nitrogen result in a difference of 1%. As such, we will use the value $\sigma_{\Delta T} = 1.275 \text{ [K]}$ as the threshold for the equilibrium time.

Of course, this presents new challenges. To measure argon in firn there are two challenges to overcome:

- ▶ General abundance of argon in the atmosphere
- ▶ Small molecular diameter of Argon causes leaks

Argon constitutes approximately 1 % of the atmospheric composition [127, 128], while nitrogen is far more plentiful at 80 %. This means, that the experimental apparatus will now need to be advanced enough to detect deviations smaller than that of nitrogen. To make matters worse, the bond length of argon is of the same scale as the ice cell size in the firn [129]. This effectively means that argon will permeate out of the ice matrix after an ice core has been drilled, also known as post-coring fractionation. ^{36}Ar will permeate faster than ^{40}Ar due to the mass difference, which presents [130] a great hurdle when reconstructing temperatures.

In this chapter, we explore the different experiments, review their results and compare them to predictions from Chapters 2 and 3 and relevant literature.

5.1 Steady state: Forward model runs

Having fitted the NGRIP accumulation rates to temperature via an exponential function, and thereby obtained N temperature, accumulation pairs, we can now run the Community Firn Model forward. As with the whole sensitivity experiment, this is done in two phases: one where we compare the agreement between the densification schemes presented in Subsection 2.2.2 and one where the same is done, but for the diffusivity parameterizations in Subsection 2.2.4. In both phases, we solve the firn-air transport equation via Patankar [77]’s approach, since the diffusivity parameterizations would not influence the analytical calculation of the fractionation effects. Here, the standard densification scheme and diffusivity parameterization are HLD and Schwander, i.e., we only change one model/parameterization. Additionally, only gravitational fractionation is enabled as there is no thermal gradient and the time step is set to annual. After each phase, the $(T_{i,\text{ref}}, \delta^{15}\text{N}_{i,\text{ref}})$ points are saved in a .csv file for use in the second part of the experiment.

5.1.1 Performance comparison between densification schemes

In Figure 5.1 the difference between densification models Herron and Langway, Herron and Sigfus, Barnola and Goujon are plotted over a range of surface temperatures in green, purple-blue, yellow and grey respectively. The marker points specify pairs of $(T_{i,\text{ref}}, \delta^{15}\text{N}_{i,\text{ref}})$ as outputted by the CFM, while the lines are straight-line segments between each point¹. The delta-values of stable nitrogen isotopes are taken at the modelled close-off depth for each densification model and temperature found according to Martinerie’s formula in Equation 2.7. Meanwhile, the black dots mark individual points used in Section 5.2 for the sensitivity experiment.

Initially, we observe that the Goujon model always predicts a lower value for $\delta^{15}\text{N}_{\text{cod}}$, than the other models. This behaviour could be due to the fact, that the Goujon model transitions earlier than the other models to zone 2 densification and as seen in Figure 2.7 predicts a lower close-off depth than HLD, HLS and BAR. Furthermore, two different “regimes” of model agreement are in play for the other models. For lower temperatures of -58 to -48 degrees Celsius, HLD and HLS agree best with the Goujon model, while for higher temperatures

5.1	Steady state: Forward model runs	43
5.2	Steady state: sensitivity tests	45
5.3	Response to changing input forcing	51

¹: Here we have chosen temperatures, that are whole numbers, in order to make the figure to distinguish between reference and modelled temperatures

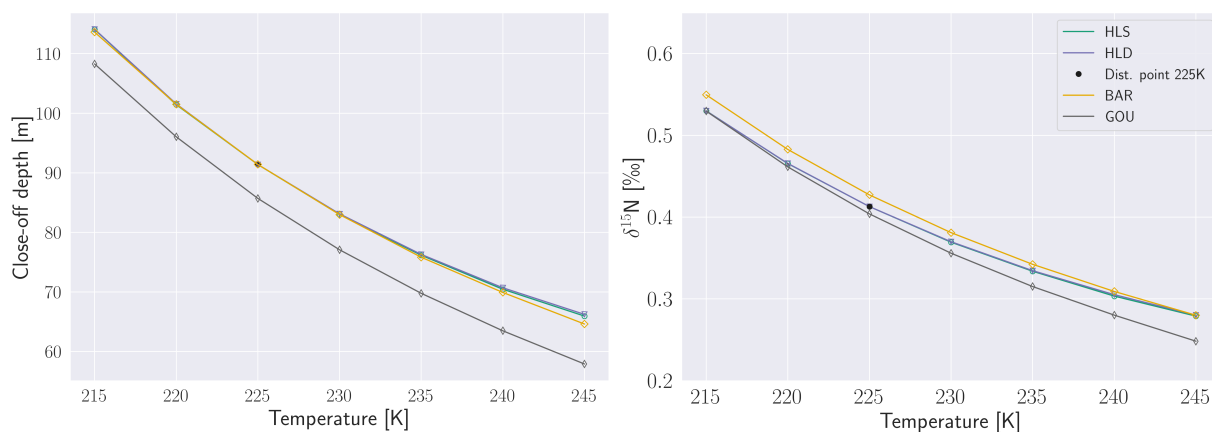


Figure 5.1: Modelled $\delta^{15}\text{N}_2$ and close-off depths plotted as a function of temperature over $N = 6$ points with densification models HLD, HLS, BAR and GOU. The marker points signify individual model outputs, while the lines are interpolations between each point.

the same is true for BAR. One might have thought otherwise, as the Goujon model is the only scheme that does not use the Herron and Langway model for the first densification zone. Curiously, this “envelope” or pocket shape, where the HLD and HLS are contained within BAR and GOU also takes place in Figures 5.8 and 5.9.

5.1.2 Deviation between diffusivity parameterizations

As before, in Figure 5.2 the abundance of stable nitrogen isotopes at close-off depth is plotted for varying temperatures for the six different effective diffusivity parameterizations using the HLD densification model. Note that the colours assigned to the D_{eff} parameterizations in the figure text for Figure 5.2 are only approximates. We mentioned in Subsection 2.2.4, that the Battle et al. [98] parameterization was based upon the parametrization by Schwander et al. [95], and it is immediately visible in Figure 5.2. There is some very slight deviation initially, but are otherwise indiscernible.

In addition, the number of distinguishable parameterizations changes depending on temperature. For low temperatures, we have a quintet with a deviation of ~ 0.1 ‰, except for Schwander & Battle who have a larger difference than the rest. At temperatures around -43 °C, the $\delta^{15}\text{N}$ -temperature curve of Freitag and Schwander intersect, reducing the number of discernible states to three. Finally, for high² temperatures, all D_{eff} parameterizations except Severinghaus and Freitag arrive at the same result. It is unclear if this trend continues further on for higher temperatures.

2: High is relative to the temperature range in the context of Figure 5.2.

Furthermore, our ability to discern between these separate states depends on the convergence thresholds for the Root-finder and the uncertainty in stable nitrogen isotopes or surface density. For example, the sensitivity test has a standard uncertainty in $\delta^{15}\text{N}$ is set to 0.02 ‰ to reflect the measurement error found in the work by Kindler et al. [23]. In any case, the best possibility to distinguish between each state will be at the extremes of the temperature range, where

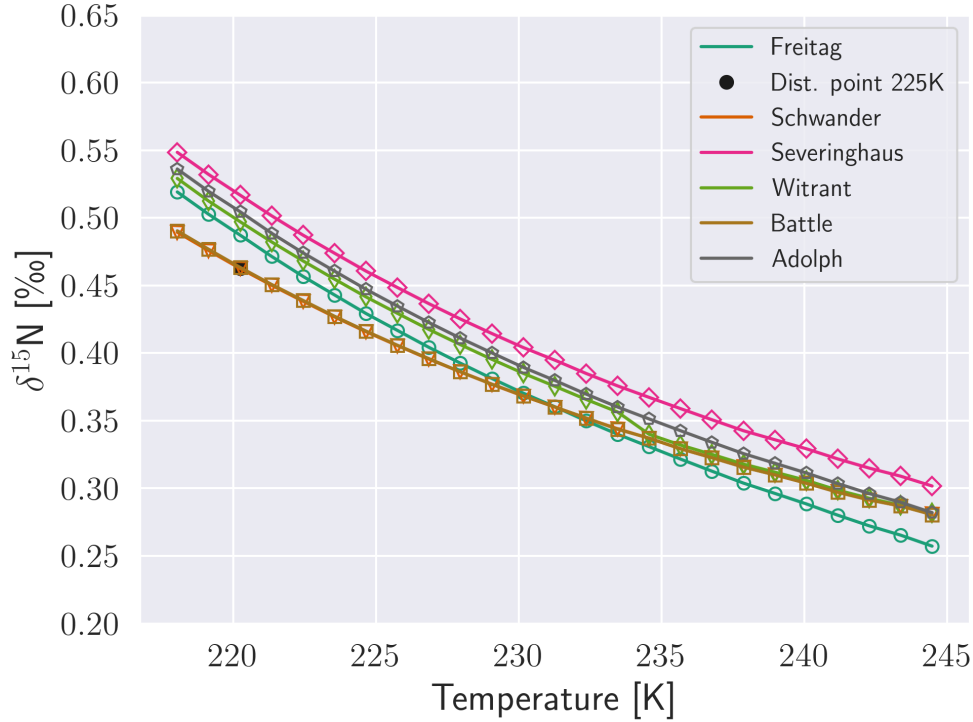


Figure 5.2: Modelled $\delta^{15}\text{N}_2$ plotted as function of temperature over $N = 6$ points with effective diffusivity parameterizations Freitag et al. [99] ●, Schwander et al. [95] ●, Schwander et al. [95] ●, Witrant et al. [100] ●, Battle et al. [98] ● and Adolph et al. [101] ●. The marker points signify individual model outputs, while the lines are interpolations between each point.

the greatest deviation is found. Finally, for the temperatures marked by the black points in Figure 5.2, we have plotted depth-diffusivity profiles for all parameterizations in Figures D.13 and D.15. Here, all parameterizations converge at zero diffusivity near the close-off depth. Notable differences between each temperature include the appearance of sin()-like shape for Witrant et al. at 234 and 244 K, however, other changes require more careful study. Interestingly, the Battle et al. parameterization shoots off from the others, even though it is based on Schwander et al.

5.2 Steady state: sensitivity tests

In this part of the steady state experiment, we test the sensitivity of the Community Firn Model by applying uncertainty in one or more parameters. We begin by comparing the ability of the different densification schemes to reconstruct temperatures based on the $(T_{i,\text{ref}}, \delta^{15}\text{N}_{i,\text{ref}})$ pairs in the last section. Next, we focus on a single densification scheme and examine the sensitivity or uncertainty of the reconstructed temperatures based on the uncertainty in stable nitrogen isotopes, surface density and diffusivity parameterizations. The absolute convergence threshold for the root-finder is chosen to be $\sigma_{\delta^{15}\text{N}}/10$, where $\sigma_{\delta^{15}\text{N}} = 0.02$ ‰ and the relative is set to $1/1000$ of the absolute threshold as inspired by the default settings for `optimize.brentq`[102]. Finally, we inspect the profile of the sensitivity as a function of reference site temperature.

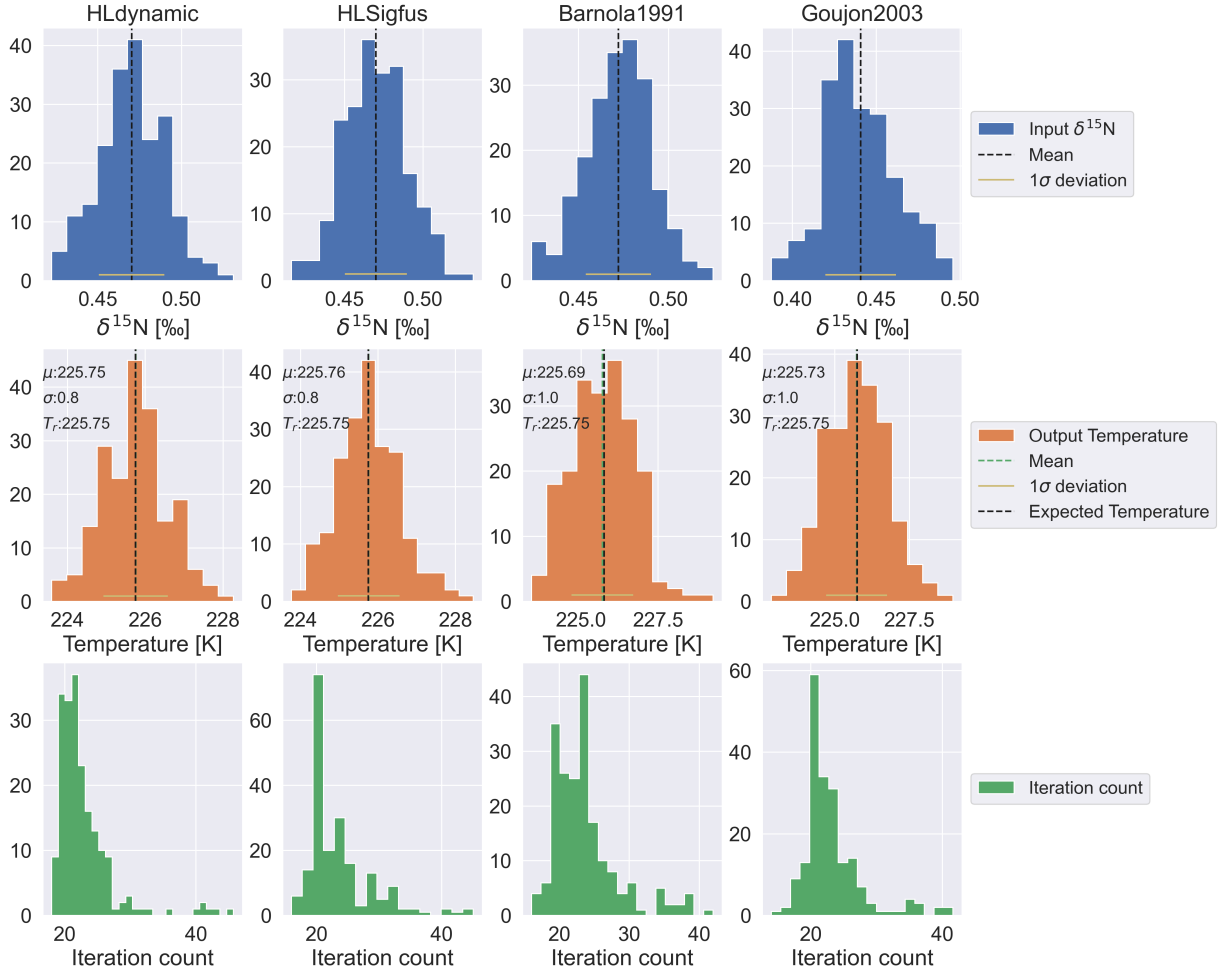


Figure 5.3: Result of inversion for 225 K with different densification schemes for $N = 200$ repetitions. Columns designate the densification scheme used, while the rows show reference stable nitrogen isotopes, reconstructed temperatures and iteration count. Black and green vertical lines respectively show the distribution mean and expected temperature, while the yellow line is one standard deviation.

5.2.1 Densification schemes

In Figure 5.3, we see the results of an inversion procedure for 225 K. In the first row is the reference $\delta^{15}\text{N}$ -distribution created from a normal distribution with the $(T_{i,\text{ref}}, \delta^{15}\text{N}_{i,\text{ref}})$ pairs from Figure 5.1 as the mean. For the second row, the reconstructed temperatures are plotted alongside a text box containing the standard deviation, mean and reference temperature for each distribution. While the $\delta^{15}\text{N}$ -distribution does change from column to column due to different values of $\delta^{15}\text{N}_{\text{ref}}$, the reference temperature does not change (see Figure 5.1). For other inversion results, see the appendix at Figures D.1 to D.4.

In general, the agreement between the expected and mean temperatures are all excellent for the different densification schemes. There is a slight increase in the deviation between T_{ref} and T_{μ} for higher temperatures, which could be related to the increase in the uncertainty from $\sigma_T \leq 1$ K at 225 K to $1 \text{ K} \leq \sigma_T \leq 1.4$ K for 235 K, see Figure D.3. There is no substantial change in iteration count with temperature, where the mode/mean for both is around 20 although Barnola and

Goujon have a slightly higher count. Notably, this does not mean that each iteration takes the same time. Recall from Figure 3.7 that higher surface temperatures equate to higher accumulation rates and from Equation 3.2 that higher accumulation rates lead to fewer volume elements. Since H , H_{basespin} and stpsPerYear are constant, the number of volume elements for 215 Kelvin is eight times the number for 245 Kelvin. Furthermore, it has also been observed that the Goujon model takes a much longer time than the other densification models based on file-generation time slots in Windows file explorer, taking almost 1.5 times as long as the other models.

It also appears, that the Goujon model seems to crash or diverge weirdly, where the reconstructed temperature falls outside the allowed range of the root-finder see Figure D.4 and Table 5.1. This results in a distribution where the temperatures either lie in the interval $T_{\text{ref}} \pm 2$ K or around 0 K, which is nonsensical. Past experiments in Section 5.3 suggest that a higher model run-time would nullify these effects, resulting in more time for the Goujon model to converge. It is, however, unknown if this behaviour is fundamental to the Goujon model or a problem with the implementation in CFM. Further investigation would involve increasing the model runtime and implementing a check to catch when the root finder outputs a result outside the allowed range. Finally, the data from Figures 5.3, D.1, D.3 and D.4 have been collected into Table 5.1, so that the development in the standard deviation over a range of temperatures can be observed. On

T_r [K]	HLD		HLS		Bar		GOU	
	μ [K]	σ [K]						
220	220.1	0.8	220.1	0.8	220.1	0.9	220.2	0.9
225	225.0	1.0	225.0	1.0	225.0	1.2	225.0	1.1
235	235.0	1.4	235.2	1.4	235.1	1.6	235.1	1.6
240	240.1	1.5	240.3	1.5	240.2	1.8	235.4	33.7

Table 5.1: Table of reference temperature, the mean and standard deviation in Kelvins for each model and reference temperature. Excellent agreement between models in most cases. Error in Goujon for $T_{\text{ref}} = 240$ K due to the output of values outside the allowed range.

Table 5.1, we see the dependence of the reconstructed temperature based on the reference temperature. The models by Herron, Langway and Sigfus perform better than those by Barnola and Goujon for this limited sample. However, except for the reconstruction at 240 K, all densification models arrive at a T_{recon} within 0.1 Kelvin in most cases with a few exceptions at higher temperatures. Additionally, it is apparent, that the uncertainty of T_{recon} increases with the temperature on the sample before us. In Subsection 5.2.3, we plot this relationship with temperature for all relevant sensitivity tests.

5.2.2 Uncertainty in other parameters

Next, we compare the sensitivity of the reconstructed temperatures, when there is an uncertainty in ρ_s and D_{eff} parameterization alongside the standard $\delta^{15}\text{N}$ uncertainty. As a standard, we use a surface density of 350 kg m^{-3} and the Schwander parameterization[95], when not randomly choosing them, such as $\delta^{15}\text{N}$ and ρ_s tests. In Figure 5.4, we see the results of temperature inversion for uncertainties in $\delta^{15}\text{N}$, ρ_s and D_{eff} for $N = 2400$. The columns show uncertainty

sources included in the inversion, with the first only including $\sigma_{^{15}\text{N}}$, while the second and third adding σ_{ρ_s} and $\sigma_{D_{\text{eff}}}$. Clearly, adding uncertainty from additional sources increase both the standard deviation of the reconstructed temperature and the deviation to the reference temperature. This is best seen in the overlap, where adding the uncertainty in diffusivity parameterization extends the temperature distribution to 230 K.

Notably, we do not see any indication of multiple modes/peaks in the third column, as we might otherwise have thought from Figure 5.2. Furthermore, when inspecting Figure D.6, where we do not include σ_{ρ_s} , there is no significant difference to Figure 5.4, where σ_{ρ_s} is included. I have the following hypothesis for this behaviour: We know that $\sigma_{^{15}\text{N}} = 0.02$ and the difference between parameterizations in Figure 5.2 was ~ 0.01 . This means that any sign of multiplicity from the diffusivity is hidden since the background uncertainty from $\delta^{15}\text{N}$ is too high.

Observing Figure 5.2, we can definitely improve in terms of which temperatures we search at. Here, it would be more sensible to search at 215 or 245 Kelvin. However, it is also apparent that the deviation between Severinghaus and Schwander/Freitag is approximately constant between 225 and 245 K at 0.05 permil. We also saw that the removal or inclusion of σ_{ρ_s} does not affect the resulting distribution noticeably regarding the multiple peaks. This points toward, that the high measurement uncertainty of stable nitrogen isotopes $\sigma_{^{15}\text{N}} = 0.02$ permil is responsible for hiding any signs of multiple peaks. To that end, the root-finder was applied for two scenarios, one where $\sigma_{^{15}\text{N}}$ takes the values 10^{-6} and $2 \cdot 10^{-3}$ permil. The first is merely a "sanity check" meant to eliminate any uncertainty from stable nitrogen isotopes, that might interfere. The second is more realistic since the data from Kindler et al. [23] had an uncertainty of 0.02 or 0.006 permil.

Indeed, we see in Figure 5.5, that this multi-modality appears for 235 K at $N = 200$ repetitions. Compare Figure 5.2, where the $\delta^{15}\text{N}$ -Temperature profiles were the closest to each other at 235 K, means that the uncertainty in stable nitrogen isotopes was among the deciding factors in hiding the multiple peaks, see Appendix D.2.1 for other figures. A consequence of this is the following: If the measurement uncertainty in $\delta^{15}\text{N}$ is of the same magnitude as the difference between D_{eff} parameterizations, then it is unimportant, which parameterization is used since any difference is hidden away. On the flip side, if the magnitude of $\sigma_{^{15}\text{N}}$ is at least 1/10 of the aforementioned difference, then it becomes important for interpreting temperature reconstructions.

On another note, in Figures D.10 and D.12, depth-density profiles are plotted for three temperatures for three different surface densities. We observe that, at the close-off depth, the distinct profiles have not yet converged, although the difference is tiny. This could be used to further research the influence of surface densities in temperature reconstruction. In general, we also note that for most sensitivity tests presented so far, the mean temperature is right of the expected temperature.

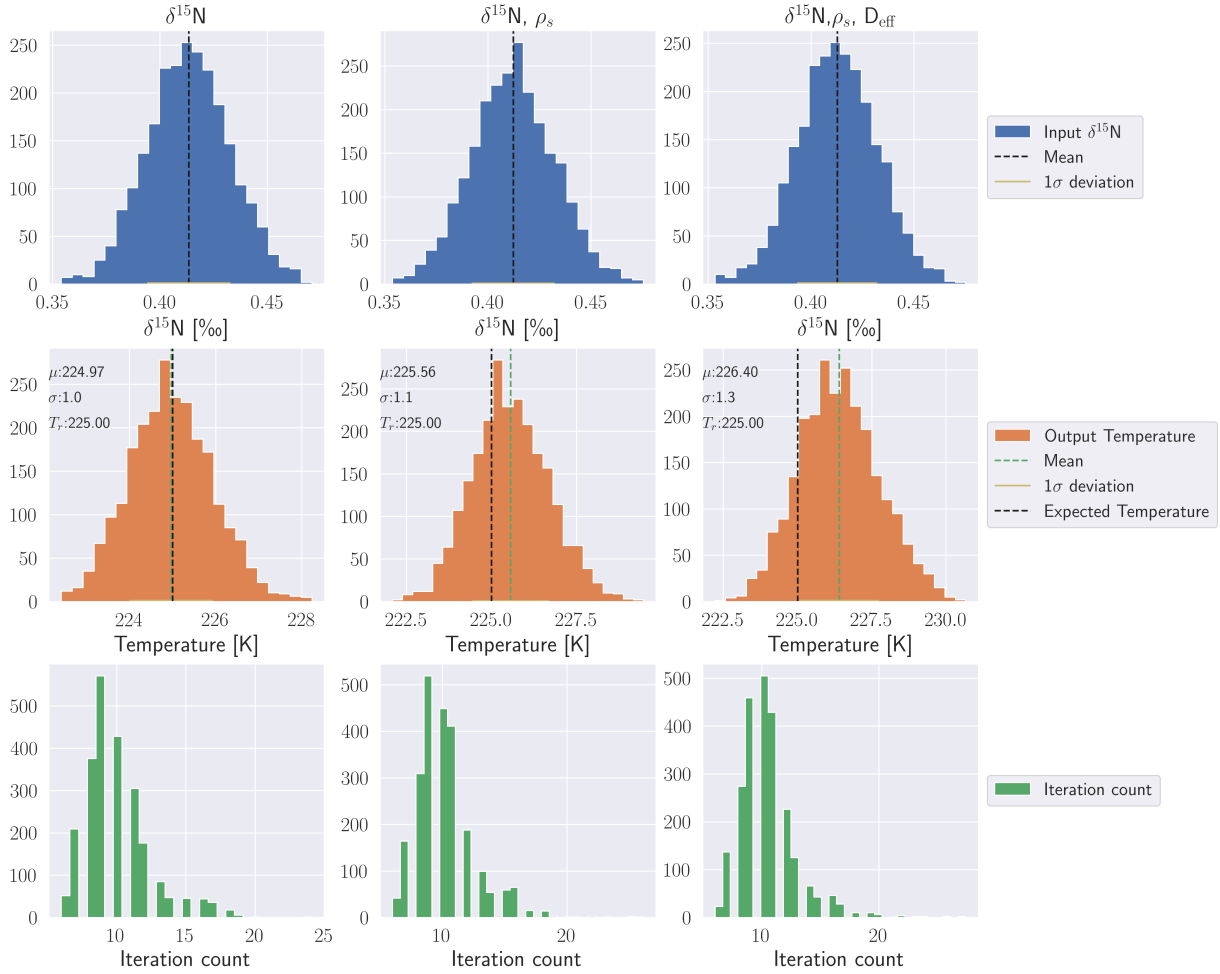


Figure 5.4: Result of inversion for 225 K with uncertainty in different parameters for $N = 2400$ repetitions, $\sigma_{15\text{N}} = 0.02$ permil. Columns designate which uncertainty is included, while the rows show reference stable nitrogen isotopes, reconstructed temperatures and iteration count. Black and green vertical lines respectively show the distribution mean and expected temperature, while the yellow line is one standard deviation.

T_{ref} [K]	Only $\delta^{15}\text{N}$		$\delta^{15}\text{N}$ and ρ_s		$\delta^{15}\text{N}$ and D_{eff}	
	Mean	σ	Mean	σ	Mean	σ
220	220.04	0.82	220.6	1.01	220.93	1.08
225	225.08	0.97	225.67	1.16	225.91	1.22
230	229.98	1.17	230.58	1.31	230.70	1.36
235	235.01	1.28	235.60	1.43	235.44	1.5
240	240.14	1.5	240.76	1.65	240.37	1.75
245	244.84	1.73	245.47	1.86	244.85	2.03

Table 5.2: Table of reference temperature, the mean and standard deviation in Kelvins for each uncertainty source and reference temperature.

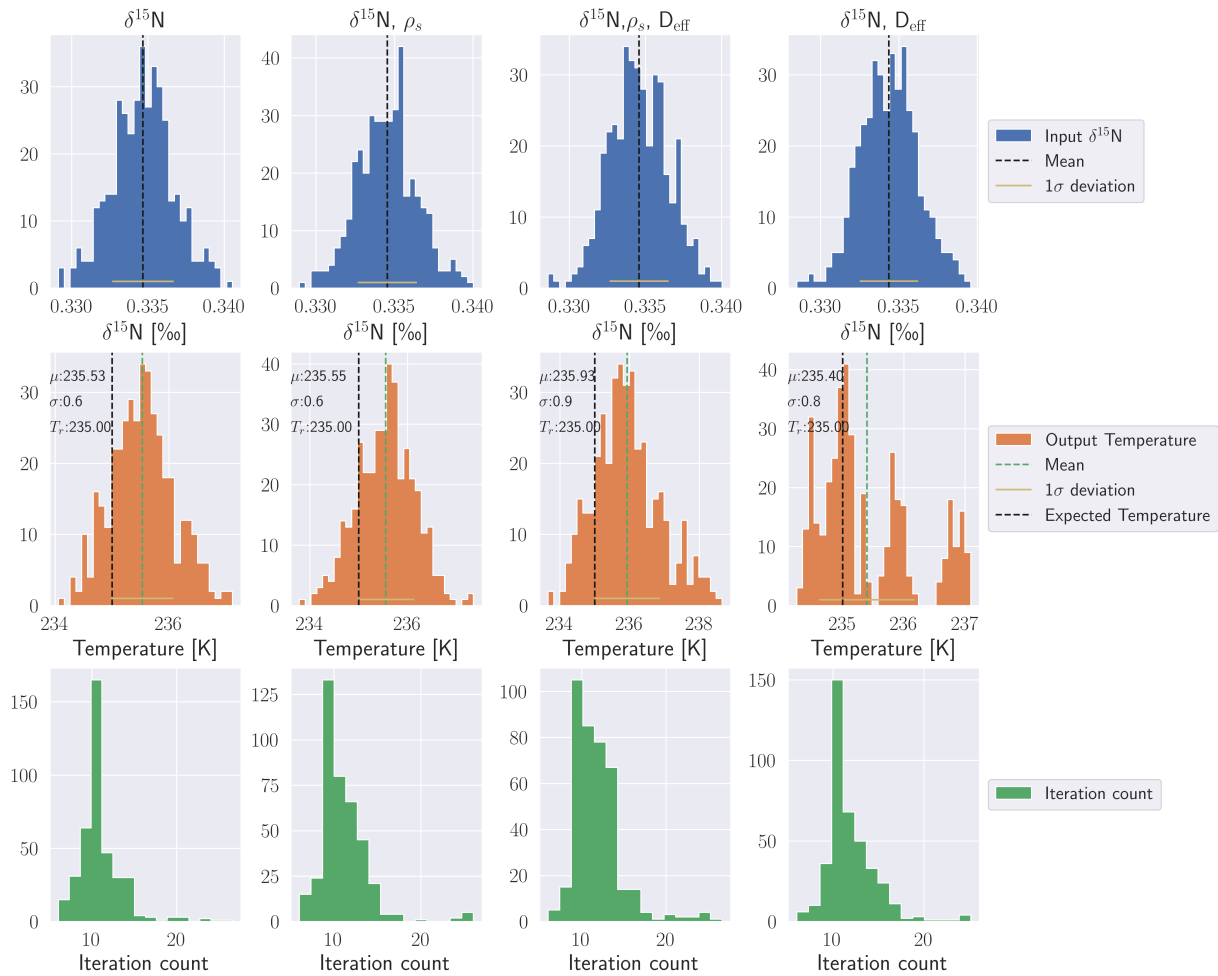


Figure 5.5: Result of inversion for 225 K with uncertainty in different parameters for $N = 2400$ repetitions, $\sigma_{\delta^{15}\text{N}} = 0.002$ permil. Columns designate which uncertainty is included, while the rows show reference stable nitrogen isotopes, reconstructed temperatures and iteration count. Black and green vertical lines respectively show the distribution mean and expected temperature, while the yellow line is one standard deviation. Multiple peaks are clearly visible.

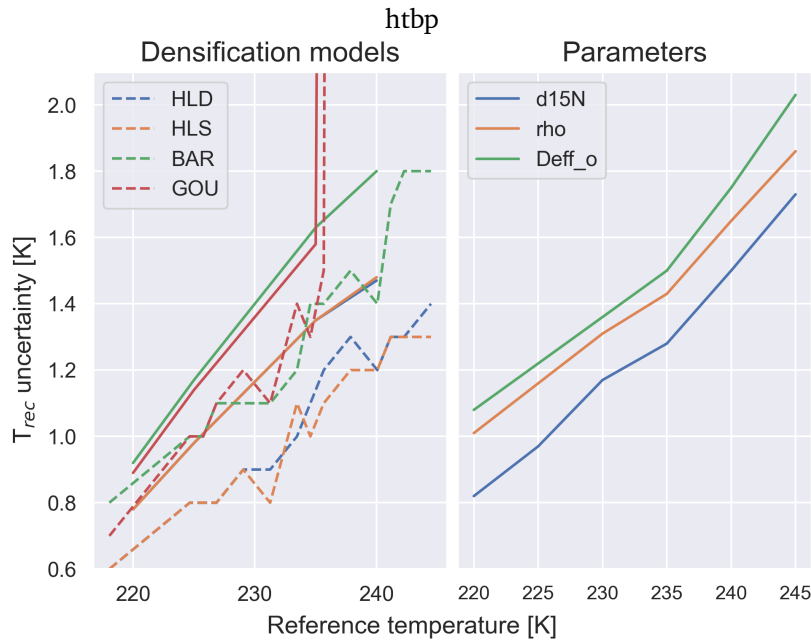


Figure 5.6: Relationship of reference temperature and uncertainty for reconstructed temperatures. The left side shows data from Table 5.1, where the vertical line is due to the Goujon model behaviour at higher temperatures. Right side shows

5.2.3 Dependence on temperature

In this experiment, we run the root-finder for six different temperatures in the temperature range from Kindler et al. [23] and for $N = 800$ repetitions each. As the figures are rather large and unwieldy, we select a few to include in the main-text³. The recorded standard deviation of T_{rec} for the rest are then condensed into the included Table 5.2. As before, we see the same behavior as in Table 5.1, where the uncertainties of the reconstructed temperatures increase with the reference temperature. To get a better visual representation, this relationship is plotted alongside the data from Table 5.1 into Figure 5.6. The dotted lines on the left are from a series of inversions from 218 K to 245 K. In all cases the uncertainty increases for rising reference temperatures. According to my knowledge, the cause of this is unknown and more research is necessary. From Figures 2.7 and 2.8, we know that increased temperatures lead to a shallower firn column and smaller close-off-depths. Therefore, one possible cause for this behaviour could be that the thinner firn column results in higher variability in the different outputs.

³: See Appendix D for the remaining plots

5.3 Response to changing input forcing

As mentioned earlier, we now turn to modelling the response of the Community Firn Model, when forced by a ramp input forcing of varying magnitude and duration. In addition, we will also review the method for estimating the temperature gradient and uncertainty in the Subsection 5.3.3

5.3.1 Varying magnitude

In Figure 5.7, two figures are plotted, one where both the temperature and accumulation rate are altered and one where only temperature is. Changes in only accumulation can be seen in Figure E.1 and an overview of all plots for the Barnola model is found in Appendices E.1 and E.2. Along the rows, we have a) temperature and accumulation forcing, b) close-off depth according to Equation 2.7, d) temperature gradient, e) resulting $\delta^{15}\text{N}_{\text{th}}$ and f) the total $\delta^{15}\text{N}$. Furthermore, the vertical lines signify the halfway time until equilibrium for z_{cod} , ΔT and equilibrium time for $\delta^{15}\text{N}_{\text{th}}$. The colour map chosen here uses “yellower” colours for higher amplitudes and vice versa. The equilibrium time for $\delta^{15}\text{N}_{\text{th}}$ is found by finding the first constant element to a tolerance of 0.006 permil, exploiting the fact that the equilibrium level is zero.

In Chapter 2, it was explained that increasing accumulation rates and temperature had opposite effects on the close-off depth. An increased surface temperature would lead to higher rates of densification leading to a shallower firn column and smaller z_{cod} . Increased accumulation rates meanwhile would lead to thicker firn columns and larger z_{cod} . We see the same behaviour in Figure 5.7 and that combining both “effects” lead to a now non-monotonic curve for the close-off depth. The close-off depth first increases quickly, before becoming overpowered and decreasing to a smaller value than previously. It would therefore seem that accumulation and temperature affect the firn at two different speeds, but also in two different magnitudes⁴.

4: This is reminiscent of the interplay between salinity and temperature in the Two-box Stommel model for the AMOC, see [131] for a very nice overview.

We also see a curious difference in the shape of the temperature gradient in d) between the upper and lower plot in Figure 5.7. Here, the shape for temperature change is sharper than the one for both temperature and accumulation. Although the accumulation rate does not directly affect the temperature gradient, it does affect the close-off depth, from which the temperature gradient is defined. In addition, heat diffusion is also altered slightly by way of changing the densification rate and column length. This results in a “smoother” function and a more varied distribution of halfway times.

This effect is also seen in the plot of $\delta^{15}\text{N}_{\text{cod,th}}$. Although here, the timing of the halfway times are reversed, which can also be seen in Figure 5.8.

In these figures, the halfway times have been collected for all densification schemes and the 28 magnitude multipliers. In each column the halfway time for each output is shown along with change in temperature, accumulation or both along the rows. Here, we immediately observe the aforementioned envelope shape from Figure 5.1 for most of the plots. The general trend for the halfway times seems that a higher magnitude leads to a lower time in all cases. This is a surprising result, as conventional wisdom [132] holds that larger fluctuations, concentrations or sizes require more time to equilibrate. However, in the upper part of Figure 5.8, we see the opposite behaviour and a more correct version in the lower half. In Subsection 5.3.3, we will

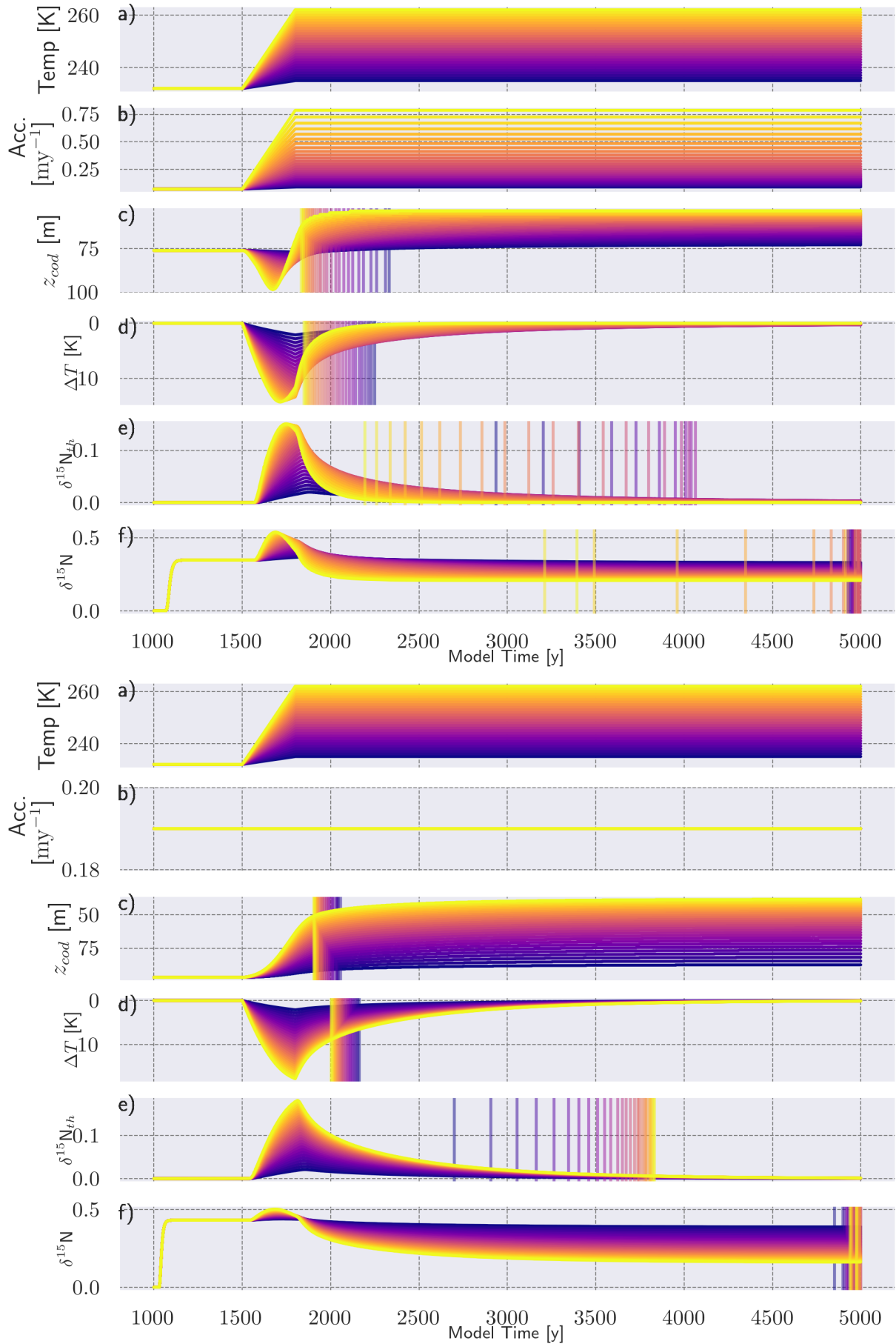


Figure 5.7: Response of CFM for changes in magnitude. Above: Changes in both temperature and accumulation rate, below: Changes in temperature only. Temperature gradient is taken between surface and close-off depth.

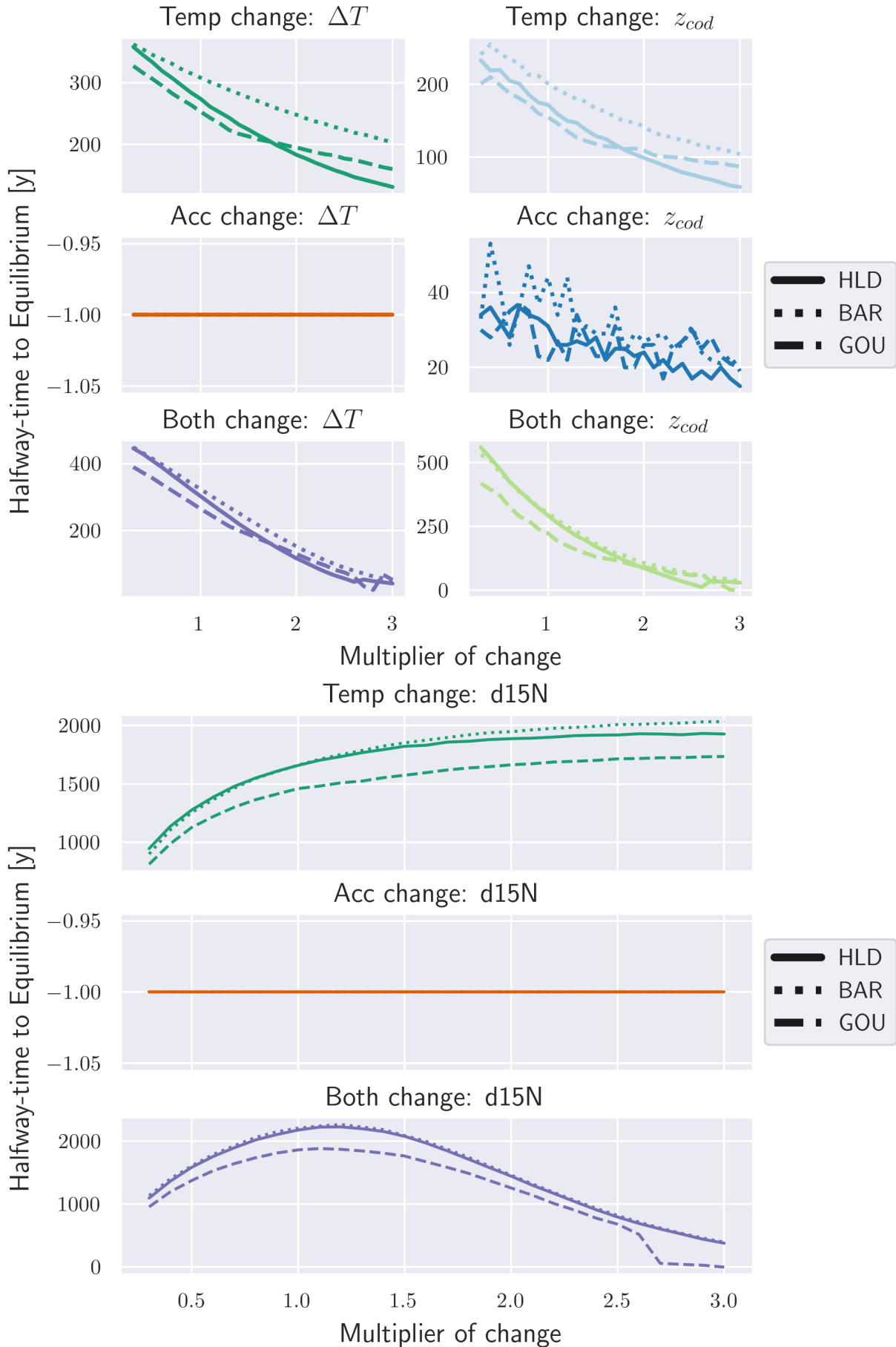


Figure 5.8: Collection of half-way times for changes in magnitude. Columns show half-way times in ΔT and z_{cod} , while rows signify changes in each forcing category.

compute the true equilibrium time for both ΔT and z_{cod} to hopefully shed some light on this matter.

However, for the accumulation close-off depth plot, there is high variability in the half-way times. Unlike its counterpart, the accumulation of snow does not feature a diffusion-like effect. Instead, each new element is set into place in discrete, sharp steps, unlike the diffusive smoothing of the temperature due to diffusion.

Finally, in the lower part of [Figure 5.8](#), we see two distinct behaviors for $\delta^{15}\text{N}_{\text{cod,th}}$. Changes only in temperature lead to a \sqrt{x} -like curve, while changes in both forcings lead to a x^2 -like curve, where x is the multiplier of change. One hypothesis for this behaviour could be that there exist two regimes of behaviour. One for $0 \geq x \leq 1.25$, where temperature dominates and one $1.25 \geq x \leq 3$, where the accumulation rate dominates the behavior. We also see a significant difference in the timescale between the upper and lower plots. This is because, for $\delta^{15}\text{N}_{\text{th}}$, we use the true equilibrium time, which is naturally larger than the half-way time.

5.3.2 Varying duration

Next, we consider changes in the duration of an input forcing signal. The array of duration values is set up to include eight entries between 10 and 100 years and then 20 linearly spaced values between 100 and 2000 years⁵. This is done to focus on events with a forcing increase or decrease in that time frame. The difference in duration creates a significant difference between outputs at each end. Short durations lead to sharp and fast initial "moves toward equilibrium", while longer durations result in more gradual changes. Observing [Figure 5.9](#), we see both a more exciting and boring figure than [Figure 5.8](#). Here, the general trend is an initial decrease in half-way time before increasing and decreasing again⁶. The exception is both-close-off depth, where we instead observe a fast decline. Finally, the equilibrium time for $\delta^{15}\text{N}_{\text{cod,th}}$ is remarkably monotonic and seemingly the same for all changes. We do see a sharp drop to 0 years for changes in temperature for the GOU and HLD models. Presently, this seems to have been caused by a reaction to the fast changes. In general, we see that changes in duration result in more homogeneous half-way times compared to that of magnitude change regarding the time scales.

5: See [Appendix E.1](#) for all figures

6: Unknown, if this trend continues beyond 2000 years.

5.3.3 Addendum: Argon and true equilibrium time

In [Subsection 4.3.1](#), we detailed how it might be possible to obtain the true equilibrium time for all variables. Essentially, we search for the first element, where the deviation between the current and the final value is below a set tolerance. For parameter z_{cod} and $\delta^{15}\text{N}$, we use the model resolution of 0.5 meters and measurement uncertainty of 0.006 permil from Kindler et al. [23]. Regarding the temperature gradient between top and close-off-depth, we instead use the result of

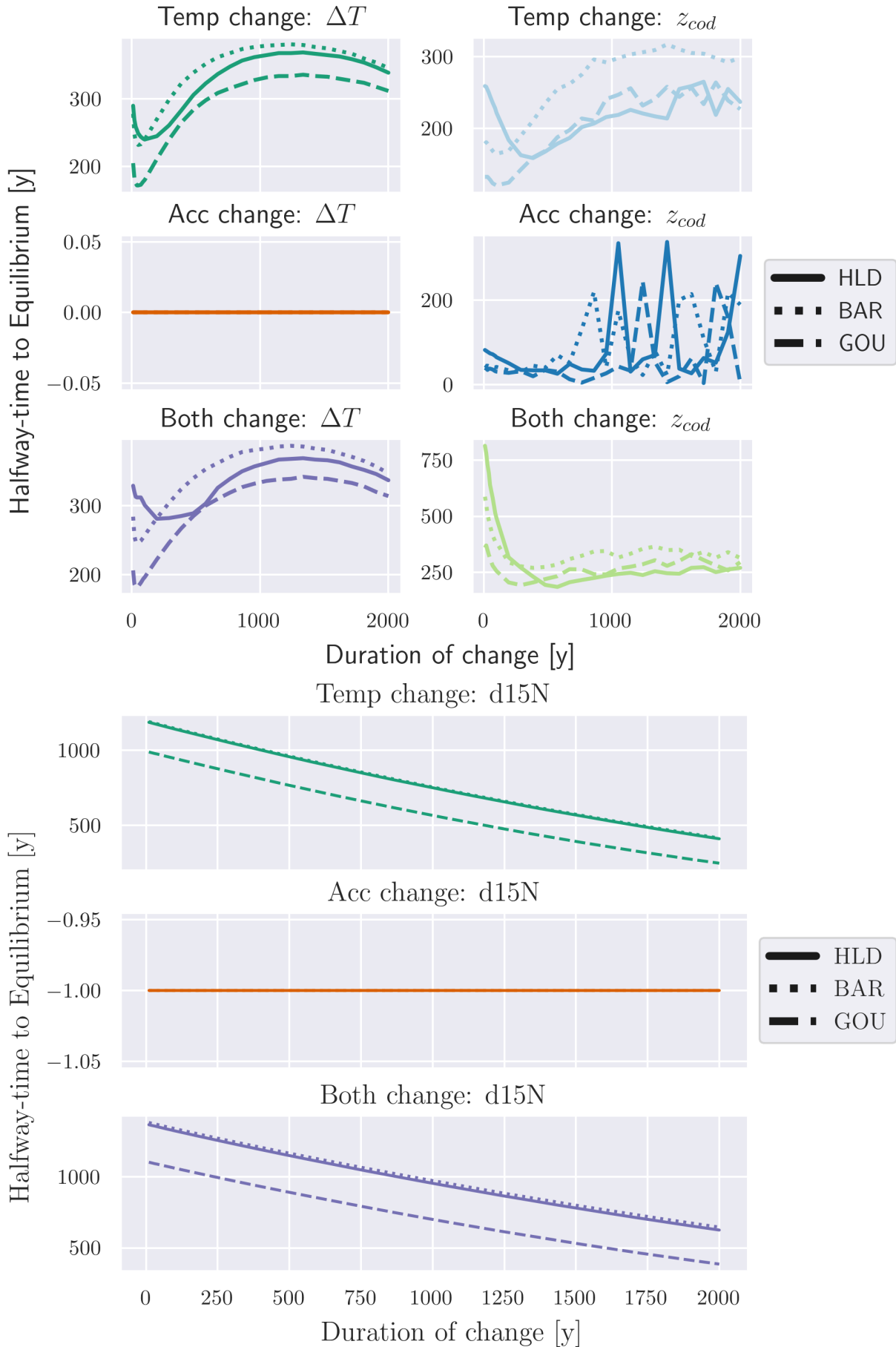


Figure 5.9: Collection of half-way times for changes in duration. Columns show half-way times in ΔT and z_{cod} , while rows signify changes in each forcing category.

$\sigma_{\Delta T} = 1.275$ K from Subsection 4.3.1 as our tolerance. The results can be seen in Figure 5.10 and Appendices F.1 and F.2 for the resulting figures.

Equilibrium times are necessarily higher than halfway times and the time-scales have increased as such to be closer to the ones for $\delta^{15}\text{N}_{\text{cod,th}}$ in Figures 5.8 and 5.9. In addition, all profiles, except for changes in accumulation rate, now resemble the profiles for $\delta^{15}\text{N}$. Likely, this results due to ΔT and $\delta^{15}\text{N}_{\text{cod,th}}$ being defined from the close-off-depth. In addition, we see that there is a significant difference in equilibrium times for acc. rate changes and other forcing changes. Unlike temperature, the accumulation rate does not have to diffuse down the firn-column but is instead directly applied deeper in the firn.

We saw earlier that while the halfway time was easy to compute if one was unsure of the measurement uncertainty or resolution for various parameters, it provides a misleading representation of the behavior of the system. For future research, it would therefore be more advantageous to begin with a measure of the parameter uncertainty, to compute the true equilibrium time with tolerance.

Finally, comparing the simple examples shown here to real DO-events is a challenge. Most DO-events feature a rapid period of warming, a plateau followed by a longer cooling period. Meanwhile, our experiment features a period of warming and a long plateau. However, the DO-events 24, 21, 14, 12 and 0 do approximately feature this behavior [23, p. 70]. Here, we compare the measurable $\delta^{15}\text{N}$ to the modelled ones. For each of these events, we observe a spike in the warming signal, which then quickly returns to approximately the previous value. This speed however, is generally faster than the equilibrium times observed in Figures 5.8 and 5.9 for similar periods of warming.

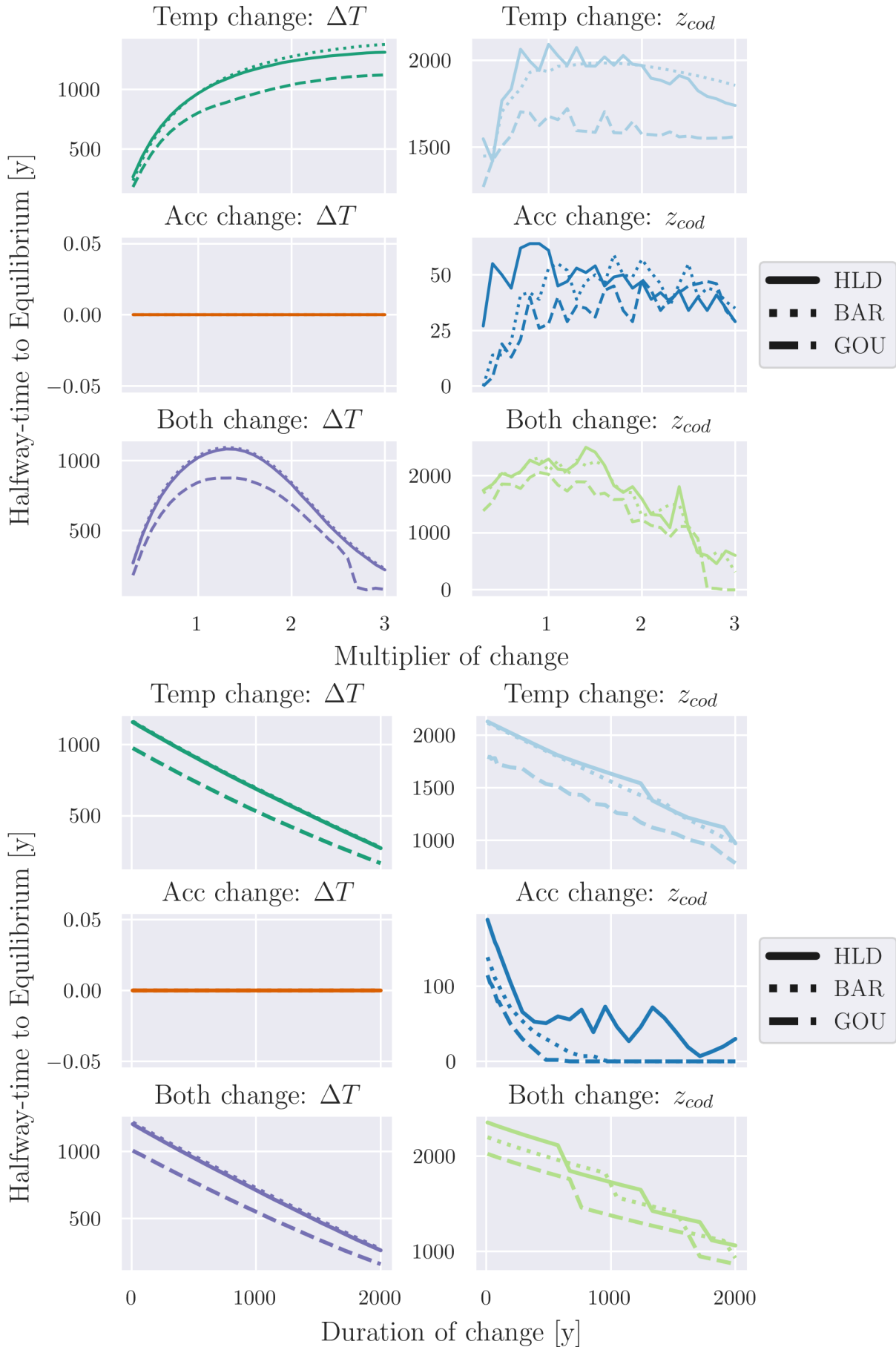


Figure 5.10: Collection of equilibrium times for changes in magnitude and duration. Columns show equilibrium times in ΔT and z_{cod} , while rows signify changes in each forcing category.

Conclusion

In this thesis, we have examined the Community Firn Model and how its coupling of densification and firn-air models might help to delve deeper into past climate changes. That is this thesis aimed to better understand the rapidity and magnitude of the Holocene transition by conducting two experiments. The first experiment focused on steady-state reconstruction of temperatures aiming to estimate the sensitivity of the Community Firn Model, if there were uncertainties in different parameters beyond stable nitrogen isotopes.

We showed that the standard deviation of the reconstructed temperatures increases, the more uncertainty sources are added. For example, $\sigma_{T_{\text{rec}}}$ for temperature inversion at 225 K for $N = 2400$ repetitions was shown to increase from 1 K to 1.3 K by adding uncertainty in ρ_s and D_{eff} . Furthermore, the sign of multiple peaks, hinted by [Figure 5.2](#), was found to be hidden due to the similar magnitudes between $\sigma_{^{15}\text{N}}$ and the deviation between each parameterization. Moreover, all densification schemes included in this thesis performed well in temperature inversion, arriving within 0.2 K of the reference temperature in most cases. Additionally, the densification models HLD and HLS consistently have a lower $\sigma_{T_{\text{rec}}}$ than those of BAR and GOU. Finally, for all cases, we observe an increase in $\sigma_{T_{\text{rec}}}$ for increasing reference temperature with some odd divergence from GOU.

The second experiment sought to investigate the response of the CFM to systematic changes in the duration and magnitude of a ramp input forcing. Firstly, we estimated the half-way-times and equilibrium times of the temperature gradient, close-off depth and $\delta^{15}\text{N}_{\text{cod,th}}$. Here, we found that the z_{cod} -model time profile is monotonic for changes in either accumulation or temperature as expected from [Chapter 2](#), but behaves non-monotonically when changing both. Secondly, for changes in magnitude, the half-way times are short monotonically decreasing, while the corresponding equilibrium times for $\delta^{15}\text{N}_{\text{th}}$ featured much longer time scales. They also showcased two different regimes of behaviour for changes in both forcings.

This behaviour continues for half-way times for changing duration, while the equilibrium times decrease monotonically. Here, we estimated the uncertainty of the temperature gradient by including $\delta^{40}\text{Ar}$ to calculate the excess amount of stable nitrogen isotopes. In doing so, we showed that the half-way time is misleading, when estimating the true equilibrium time since it predicted a lower half-way time for higher amplitudes of change. Finally, it was found that the CFM underestimates the equilibrium time for $\delta^{15}\text{N}$ compared to that of similar DO-events featuring a warming period and long plateau.

Outlook and additional research

As a final note, we will briefly review additional effects and methods, that have not been included in this thesis. Firstly, in our temperature inversion, we have been focused on steady-state inversion, to better perform the sensitivity tests. However, if one wishes to accurately model past DO-events directly, it is necessary to make use of transient firm model inversions. Here, one would exploit Equation 2.2 and use minimizers to find the coefficients α, β that yields the least disagreement between data and model. Here, one could also make use of windowed fitting to combat the change of these parameters over time [42]. This approach would use windows of fits over the 120 to 9 kyr b2k range, that each would estimate values for α, β instead of single values for the entire dataset. Moreover, one could also be to include stable argon measurements, which would lead to additional constraints on the reconstructed temperatures due to the different thermal sensitivities. As discussed previously, this carries more challenges with it as argon measurements and the resulting inversion are more challenging than their standard nitrogen counterpart[130].

Regarding the second experiment, there are a number of measures, one can take to better compare it with past DO-events. The first option would be to create modifiable DO-like events mimicking the shape of those in Kindler et al. [23, p. 70]. For example, one could include a variable length of the plateau and the cooling period. This would help reproduce the different DO-event shapes such as spikes (18,3) to "triangles" (19, 8) and "step-functions" (14,24). Additionally, steps should be taken to investigate the stepwise behaviour of the close-off depth, especially for changes only in accumulation rate, which results in higher variability of the halfway and equilibrium times seen in Figures 5.8 and 5.9.

Configuration files for the CFM **A**

In this document, we list the most important settings for the model and firn air configuration files, respectively.

- ▶ "physRho" specifies the densification scheme used for the main run physics. Here, one can select any of the 13 models, with four being the ones explained in [Subsection 2.2.2](#).
- ▶ "FirnAir" specifies if the firn_air module during the main run. This is set to True
- ▶ "TWriteInt" species the time interval in the output in years and "TWriteStart" is the first time-step to be written in the final output file.
- ▶ "int_type" tells CFM how to interpolate from forcing files to the model time. We can choose between "Nearest" for monthly climate data and "linear" for sparser data.
- ▶ "rhos0" is the surface density, normally set at 350.0 in kg m^{-3} .
- ▶ "yearSpin" is the amount of years the spin-up run should take, set to 1000 years. Users should take care to align this setting with the input files
- ▶ "H" is the thickness of the ice sheet in meters and HbaseSpin is the bottom of the model domain. These are set to 3000 m and 2700 m respectively, yielding a model height of 300 m.
- ▶ "stpsPerYear" is the amount of time steps per year, i.e., 1 yields yearly time steps, while 12 would be monthly. This is set to 0.5 as per the recommendation of Scheidt [26].
- ▶ "bdot_type" specifies if the CFM should use instantaneous or the mean accumulation rate, as seen in [Subsection 3.1.1](#). This is set to texttt"mean".
- ▶ "spin_climate_type" decides whether the spin-up run should use the initial or mean entry of the forcing files, this is set to "initial".
- ▶ "doublegrid" is an option for the CFM to compress model grids in regions where little change happens, to conserve space. This is set to False
- ▶ "outputs" species what the model should output. Here we specify "depth", "temperature", "BCO", "climate", "density" and "FirnAir". The last setting enables CFM to output firn air outputs.
- ▶ "grid_outputs" decides whether to put outputs on a regular evenly spaced grid or not. This is set to False
- ▶ "conductivity" specifies the heat conductivity parameterization used in heat diffusion. This is set to Calonne2019 [107].
- ▶ timesetup defines how to set up the time step size. "Exact" uses the input files to find the time step size, but requires a larger input file. "interp" uses a uniform dt and then interpolates the input forcing onto the model time domain. This is set to "interp".

The settings in the firm air configuration file were set as follows:

- ▶ "gaschoice" specifies the gas species to solve the firm air equation for. We set this to "d15N2"
- ▶ "gravity" and "thermal" enable `solver.py` to include gravitational settling and thermal diffusion in the finite volume method by Patankar [77]
- ▶ "runtype" can be set to either transient or steady state. We set this to "transient"
- ▶ "Diffu_param" specifies the diffusivity parameterization (see [Subsection 2.2.4](#))
- ▶ "lockin" specifies if the firm air module should include eddy diffusivity in the convective and lock-in zone. We set this to True
- ▶ "advection_type" specifies if the model should use the air advection as set by Christo, Darcy or neglect it altogether. This is set to "Darcy"
- ▶ "ConvectiveZoneDepth" specifies the depth of the convective zone. We set this to 1.5 meters.

Here, we have added the two settings "noisy_bco" and "bco_dist" to allow for variable close-off density in experiment 1.

Algorithm flowcharts **B**

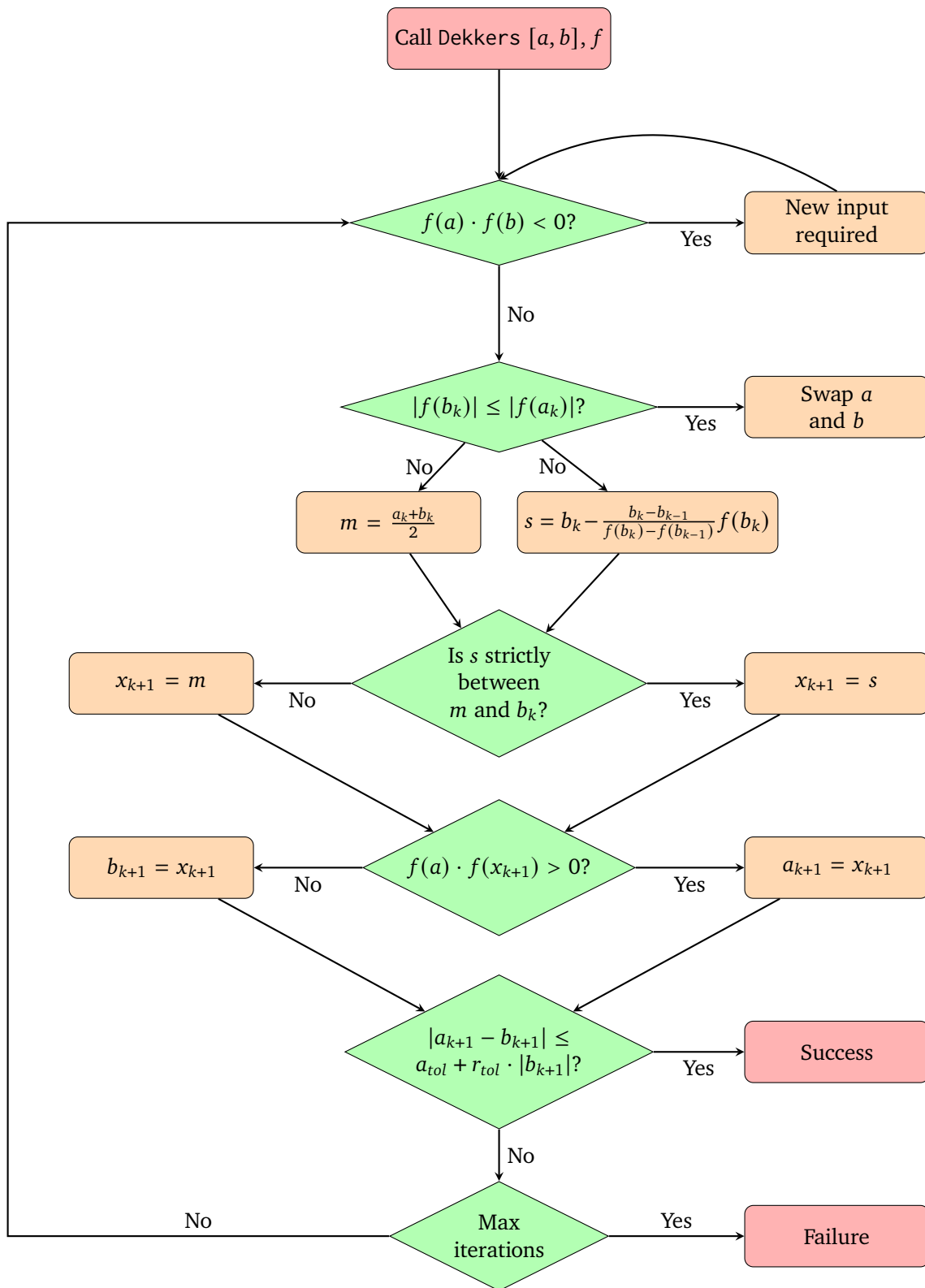


Figure B.1: Test

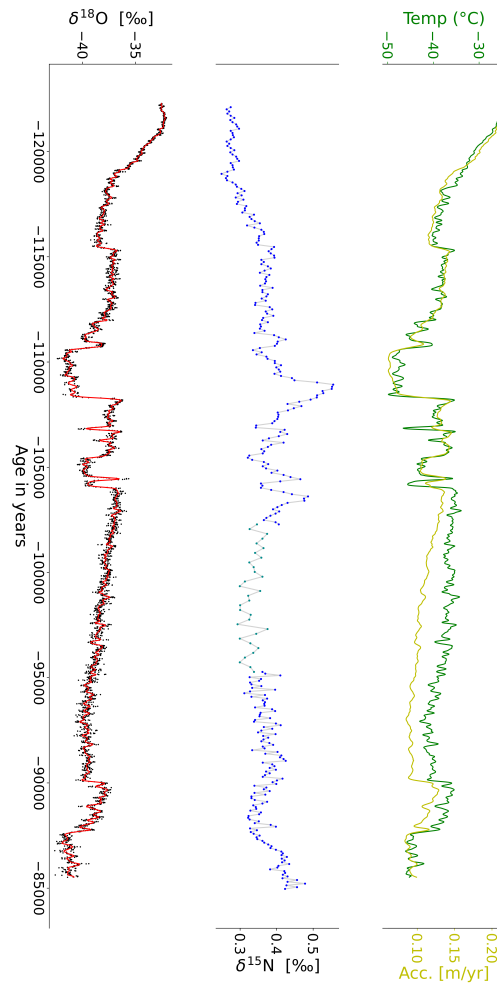


Figure C.1: Dataset from NGRIP Kindler et al. [23], 120 to 85 kyr b2k. In yellow accumulation rate in m/yr ice eq. as found by Kindler et al. [23]. In orange, the temperature reconstruction by [23] using ice-core data together with a firn densification model coupled with heat diffusion. Blue points are $\delta^{15}\text{N}$ on a gas age scale as measured by ● [108, 109] and ● by [23]. Black points are $\delta^{18}\text{O}$ on the ice age scale, while the red line is a cubic smoothing spline with a cut-off frequency $1/200 \text{ yr}^{-1}$. Adapted and modified from [23, 26].

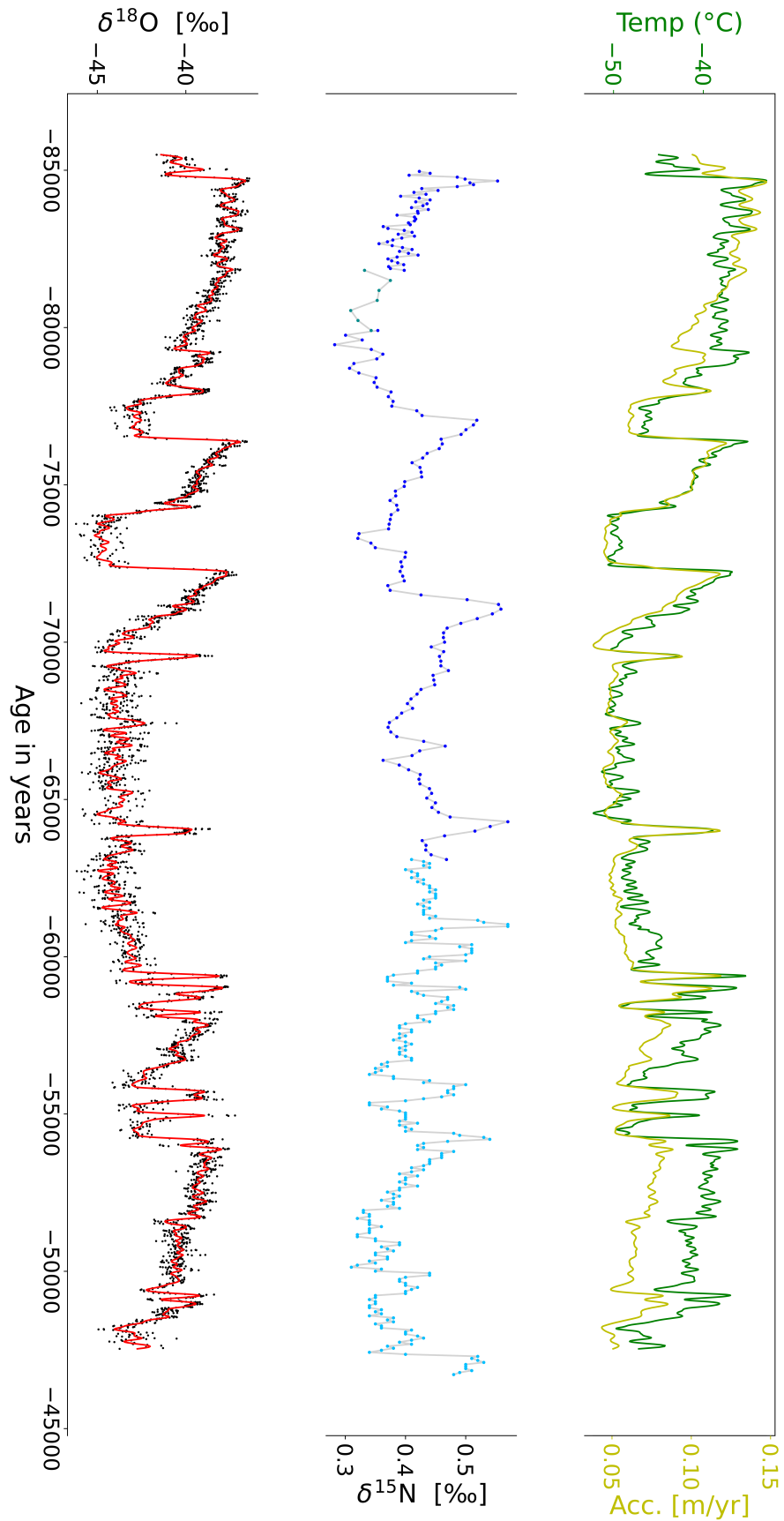


Figure C.2: Dataset from NGRIP Kindler et al. [23], 85 to 45 kyr b2k. In yellow accumulation rate in m/yr ice eq. as found by Kindler et al. [23]. In orange, the temperature reconstruction by [23] using ice-core data together with a firn densification model coupled with heat diffusion. Blue points are $\delta^{15}\text{N}$ on a gas age scale as measured by ● [108, 109] and ● by [23]. Black points are $\delta^{18}\text{O}$ on the ice age scale, while the red line is a cubic smoothing spline with a cut-off frequency $1/200 \text{ yr}^{-1}$. Adapted and modified from [23, 26].

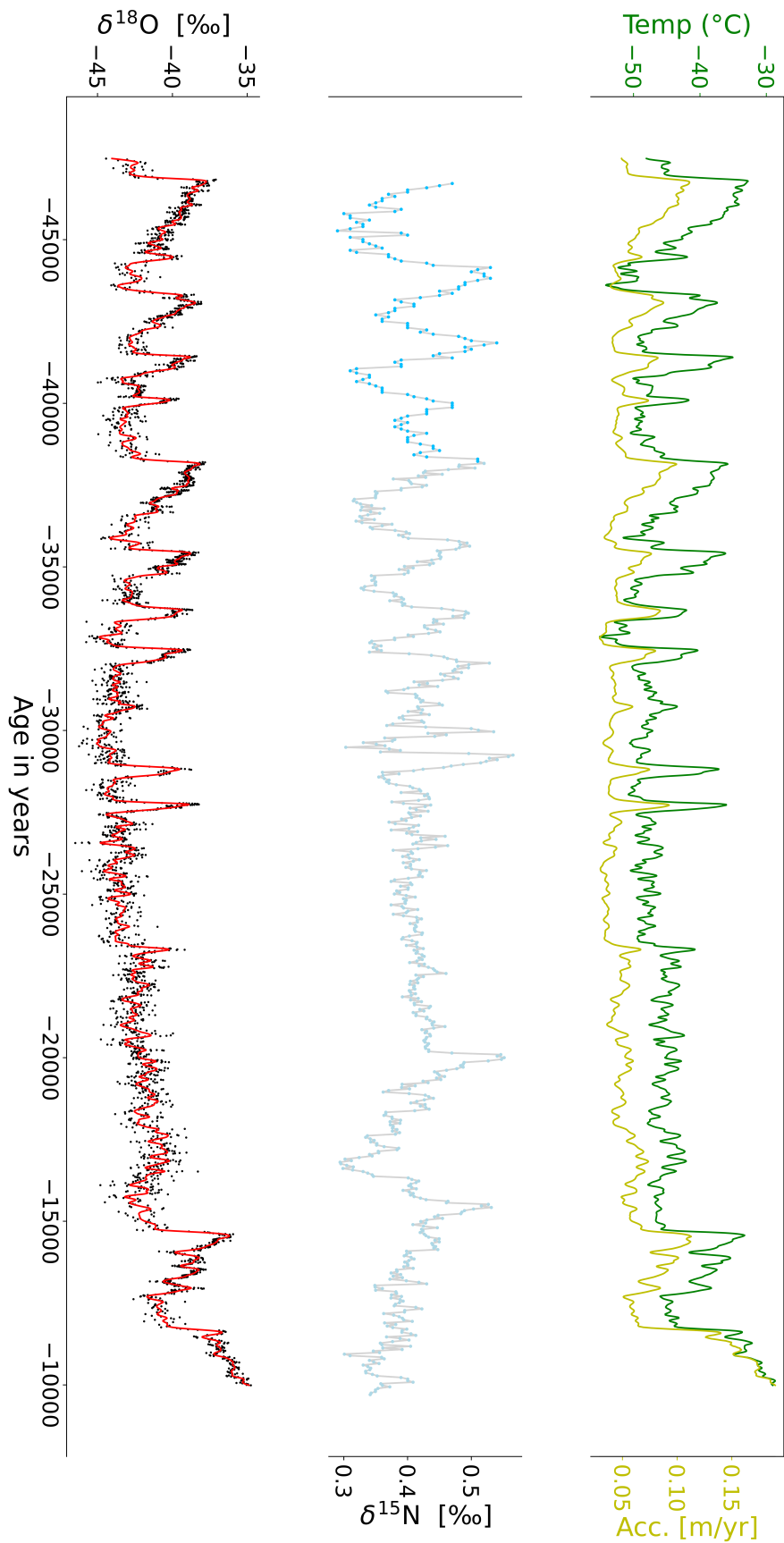


Figure C.3: Dataset from NGRIP Kindler et al. [23], 45 to 90 kyr b2k. In yellow accumulation rate in m/yr ice eq. as found by Kindler et al. [23]. In orange, the temperature reconstruction by [23] using ice-core data together with a firn densification model coupled with heat diffusion. Blue points are $\delta^{15}\text{N}$ on a gas age scale as measured by ● [108, 109] and ● by [23]. Black points are $\delta^{18}\text{O}$ on the ice age scale, while the red line is a cubic smoothing spline with a cut-off frequency $1/200 \text{ yr}^{-1}$. Adapted and modified from [23, 26].

Distribution plots

D.1 Densification models

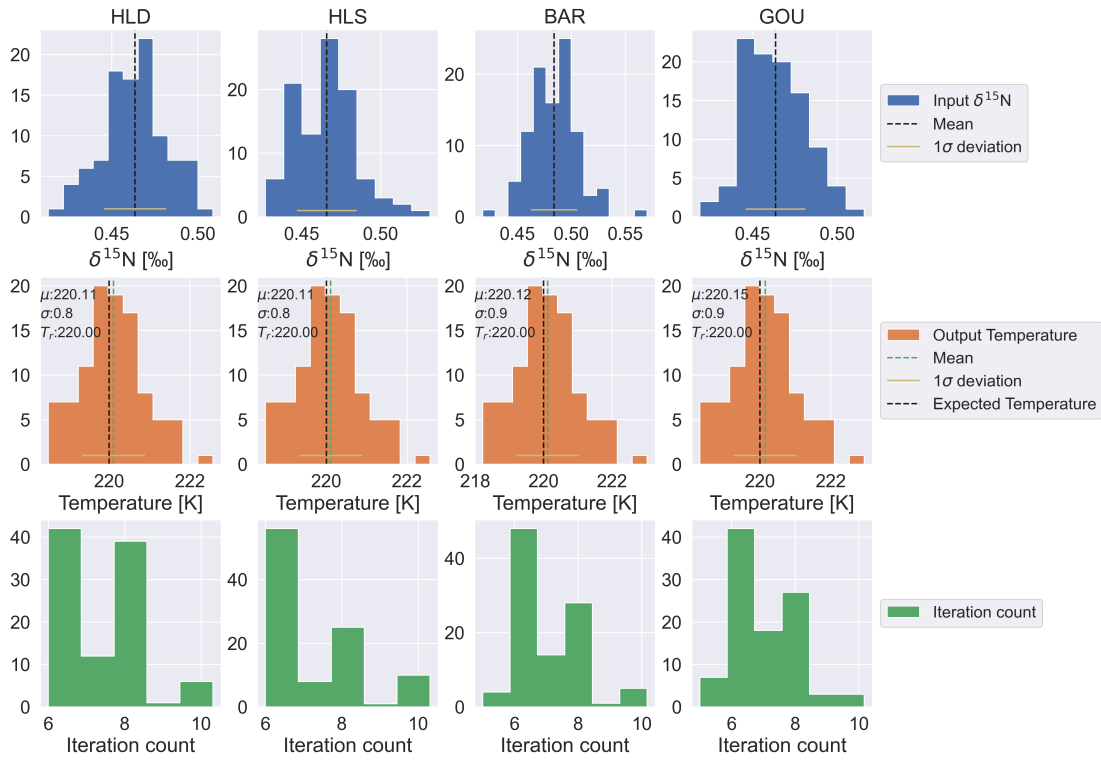


Figure D.1: Collection of plots showing results for $T_{ref} = 220$ K.

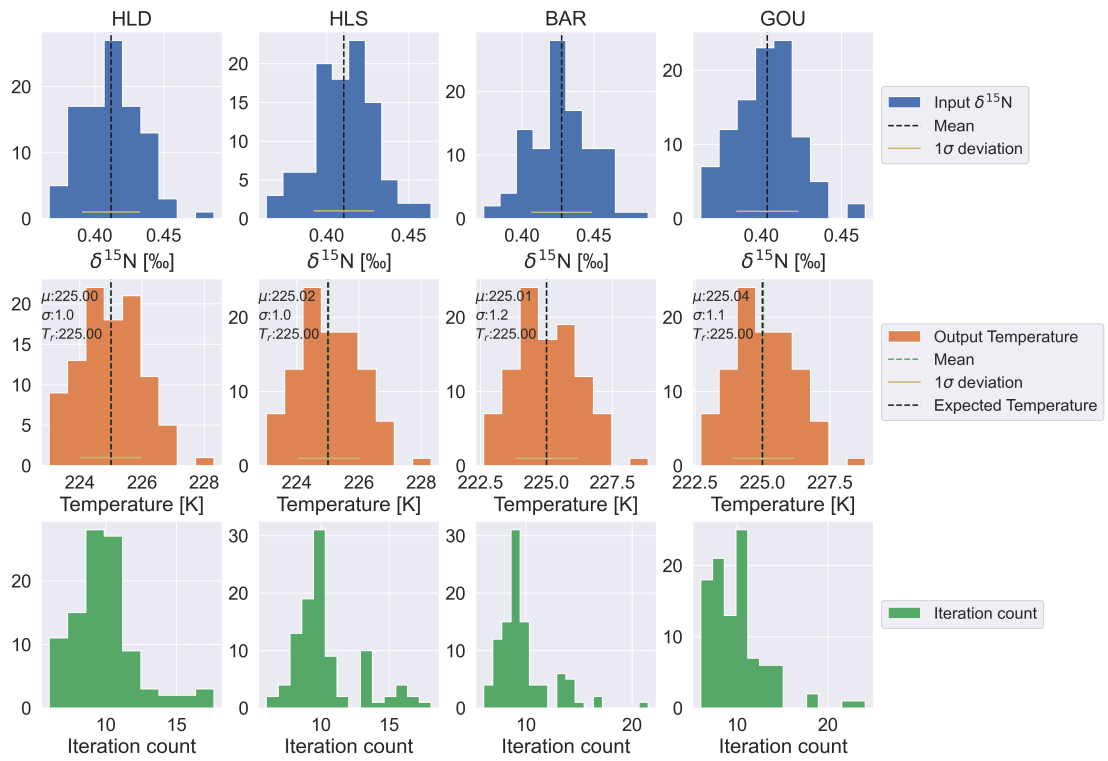


Figure D.2: Collection of plots showing results for $T_{ref} = 225$ K.

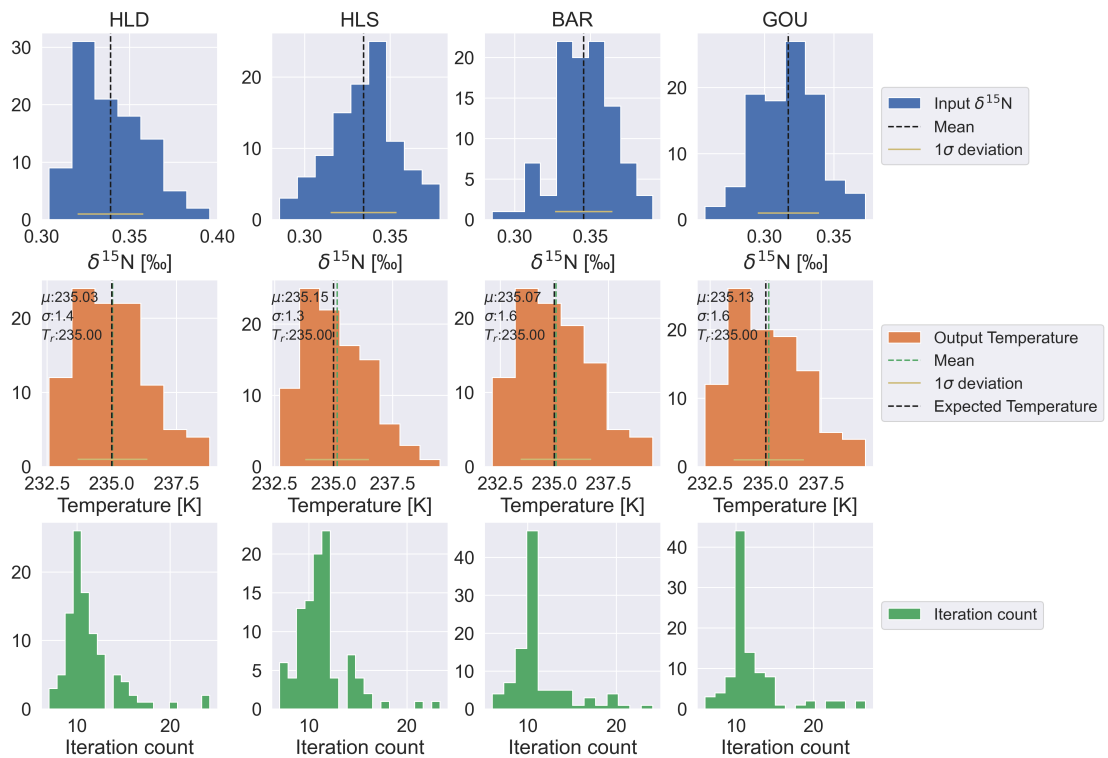


Figure D.3: Collection of plots showing results for $T_{ref} = 235$ K.

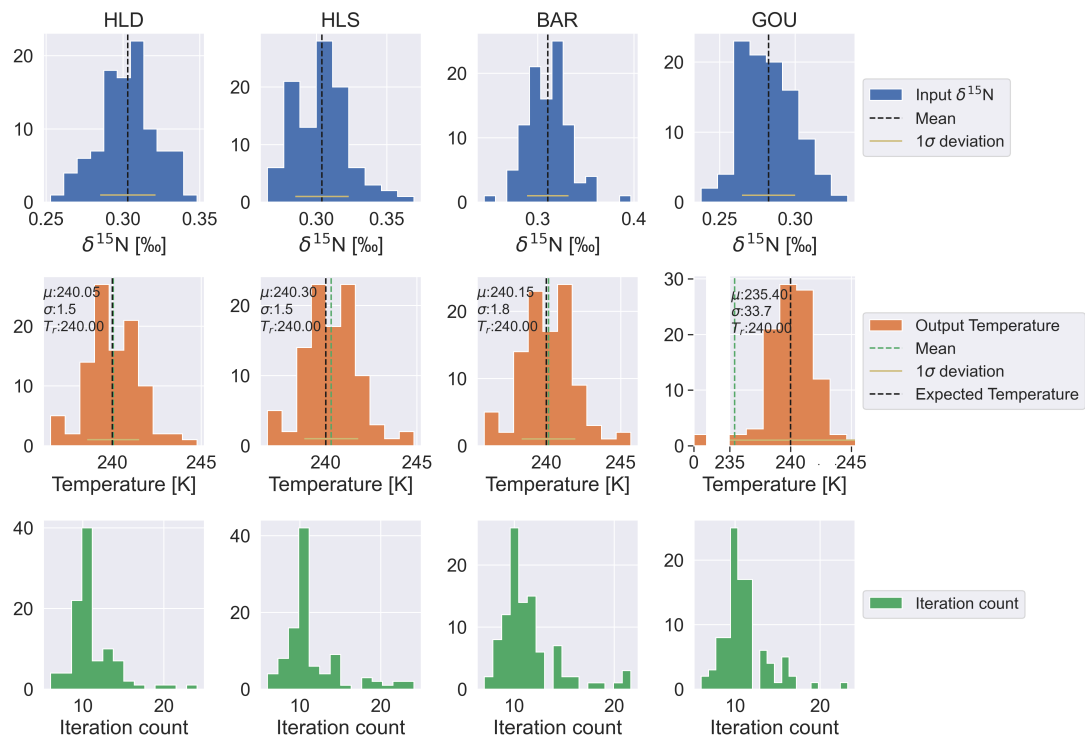


Figure D.4: Collection of plots showing results for $T_{ref} = 240$ K.

D.2 Diffusivity

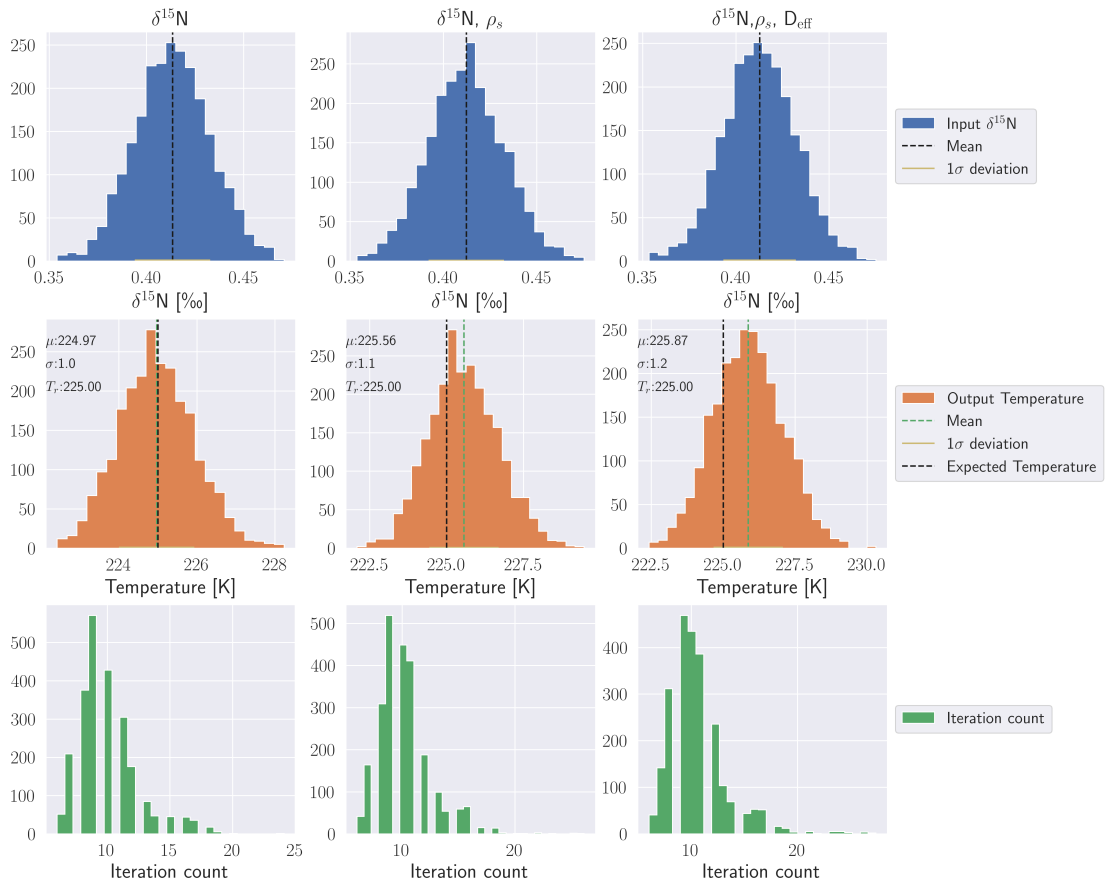


Figure D.5: Result of inversion for 225 K with uncertainty in different parameters for $N = 2400$ repetitions. Columns designate which uncertainty is included, while the rows show reference stable nitrogen isotopes, reconstructed temperatures and iteration count. Black and green vertical lines respectively show distribution mean and expected temperature, while the yellow line is one standard deviation. Surface density uncertainty is included in the third column

D.2.1 Multiple peaks

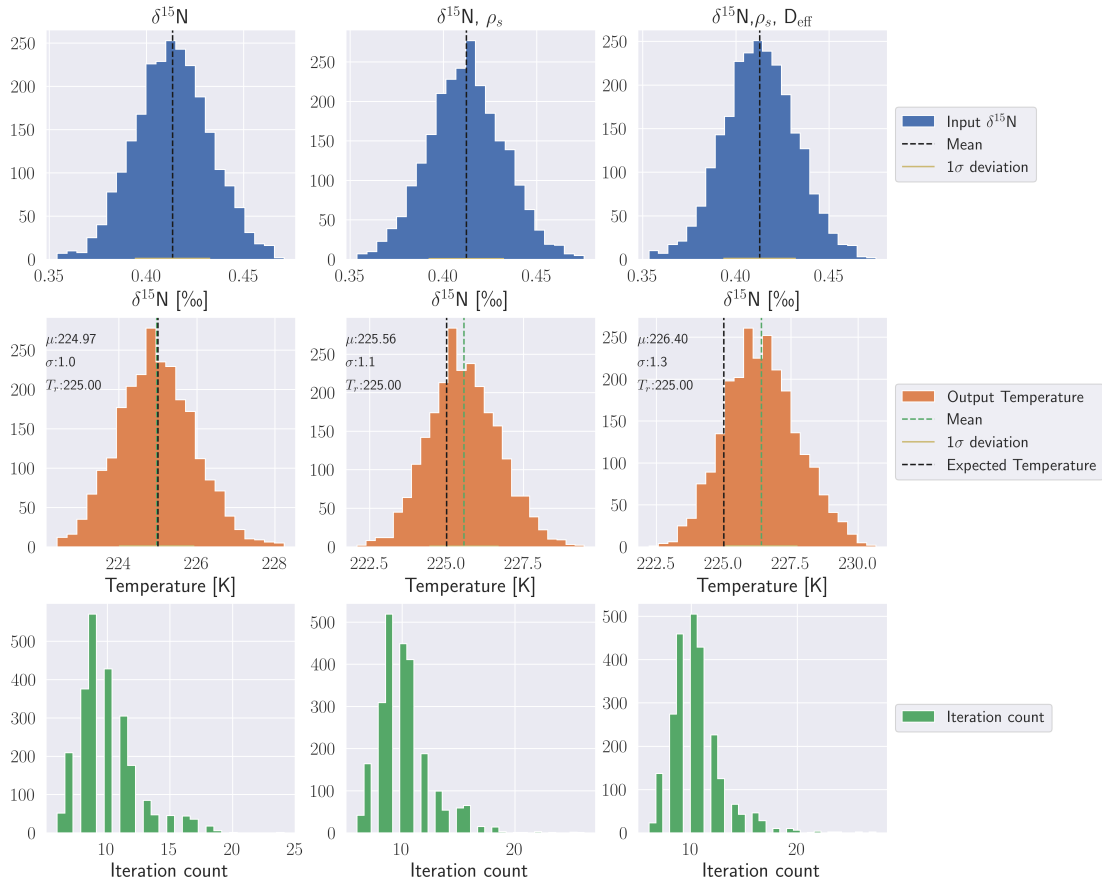


Figure D.6: Result of inversion for 225 K with uncertainty in different parameters for $N = 2400$ repetitions. Columns designate which uncertainty is included, while the rows show reference stable nitrogen isotopes, reconstructed temperatures and iteration count. Black and green vertical lines respectively show distribution mean and expected temperature, while the yellow line is one standard deviation. Surface density uncertainty is NOT included in the third column

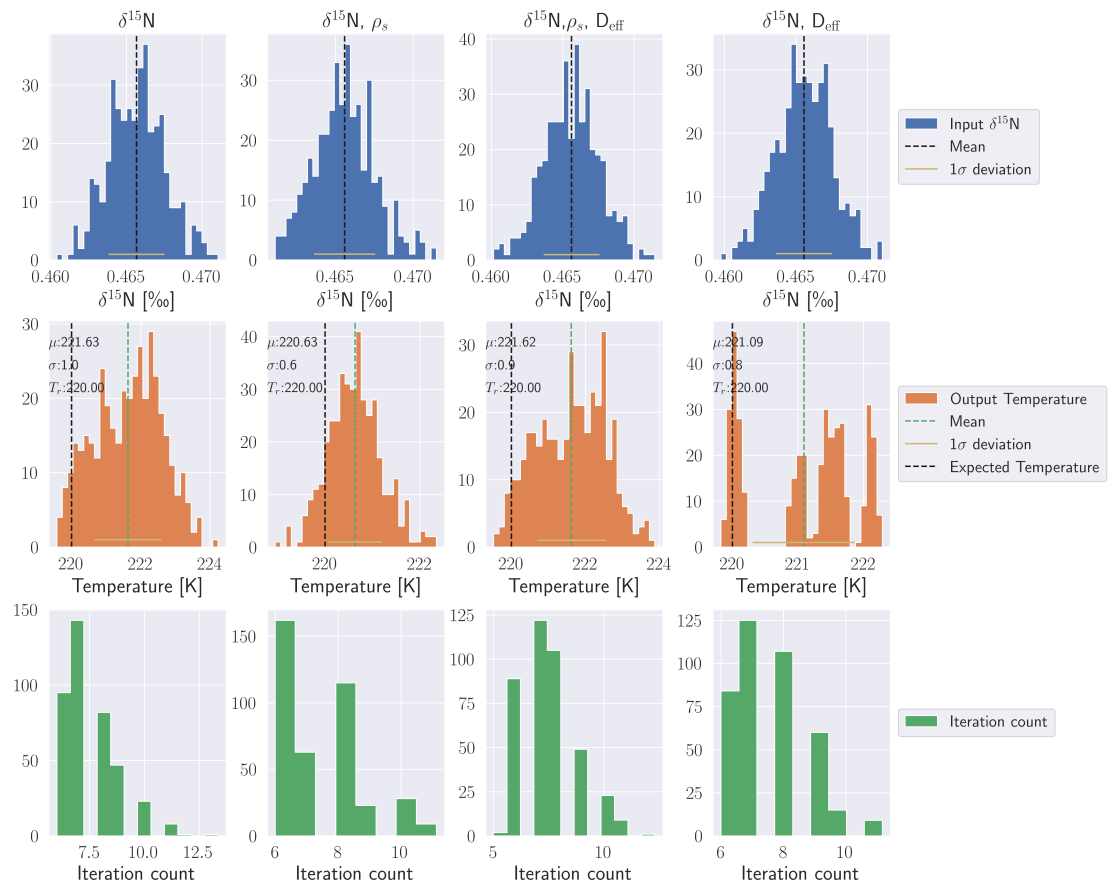


Figure D.7: Collection of plots showing results for $T_{ref} = 220$ K.

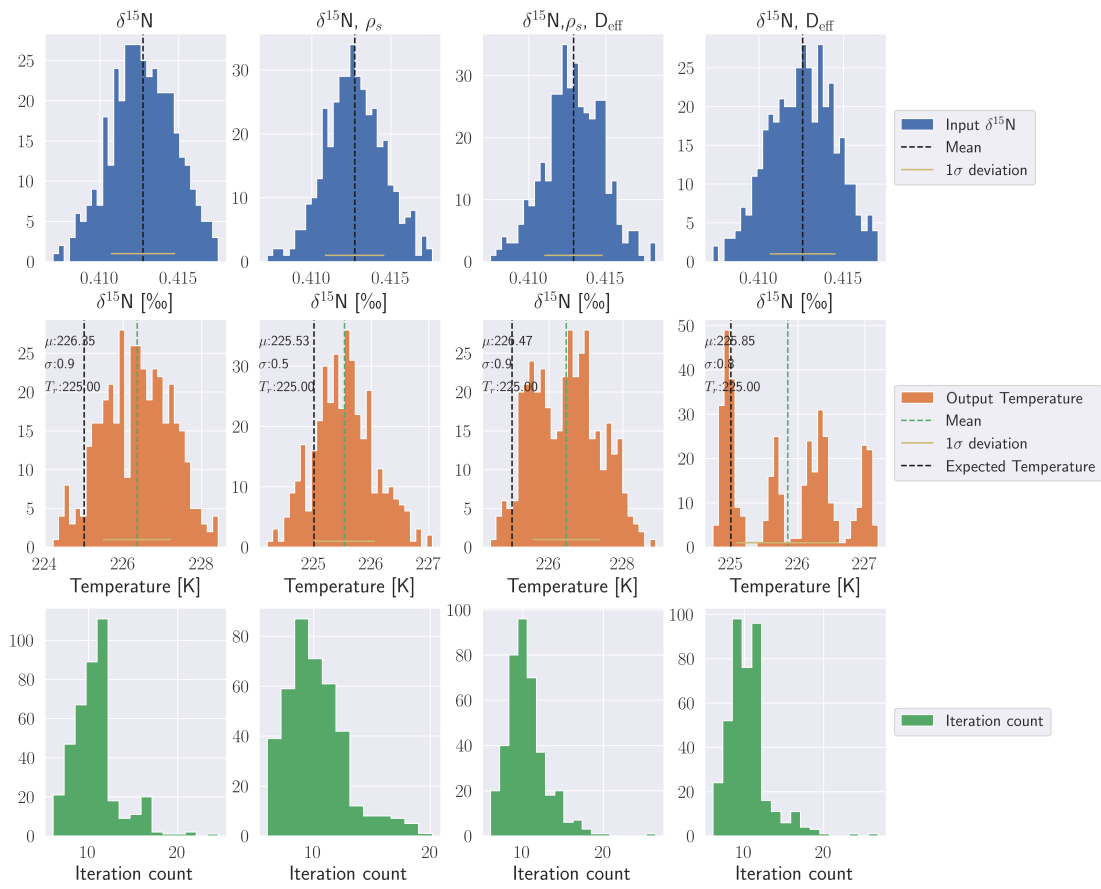


Figure D.8: Collection of plots showing results for $T_{\text{ref}} = 225$ K.

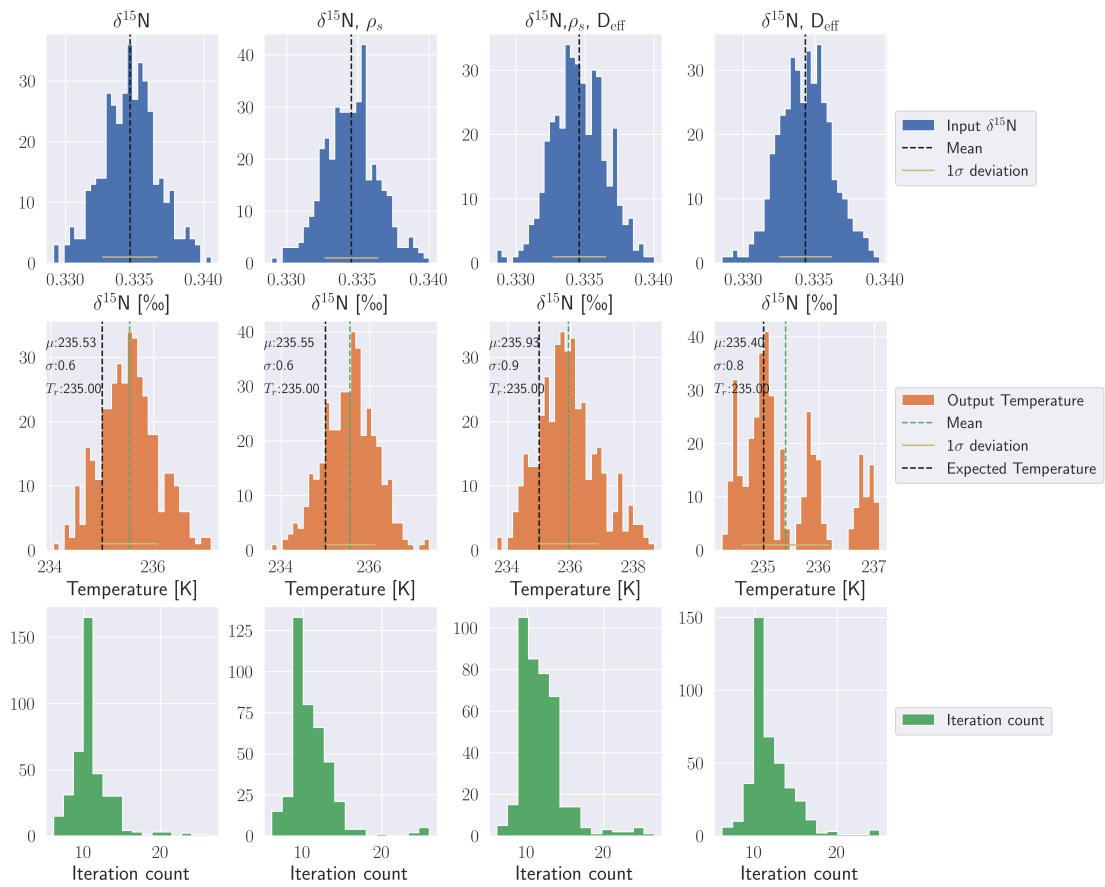


Figure D.9: Collection of plots showing results for $T_{ref} = 235$ K.

D.3 Influence of Density

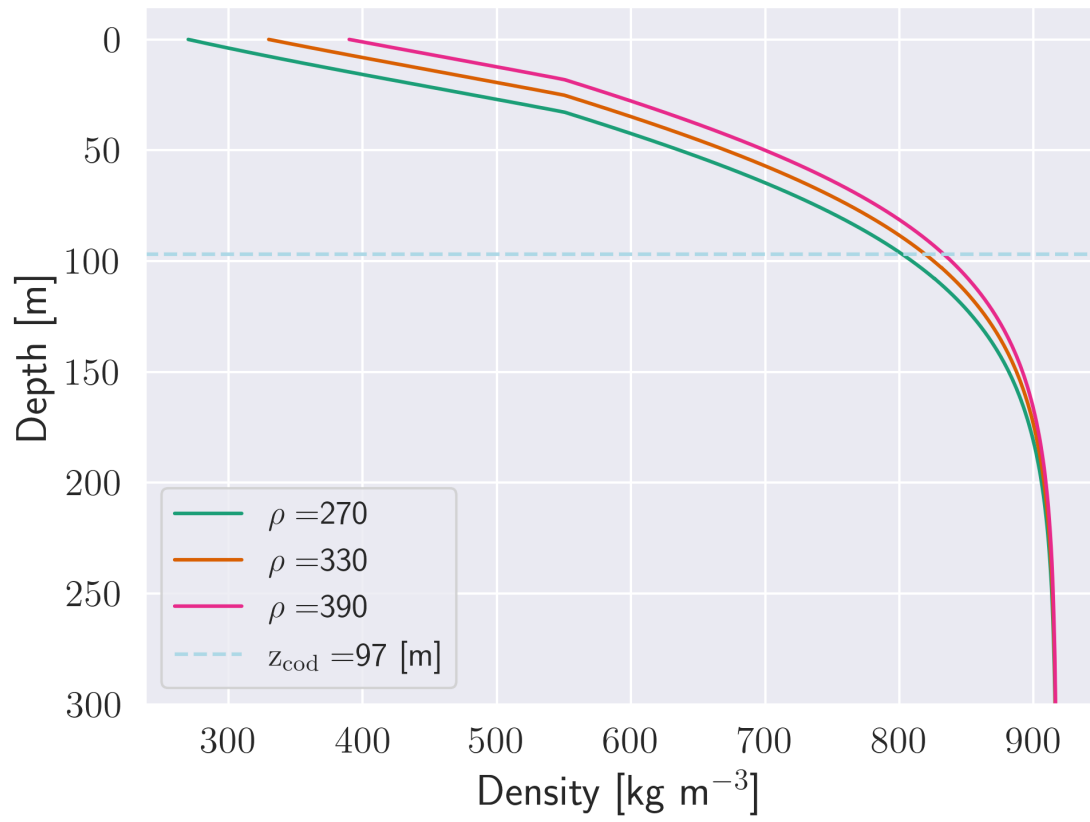


Figure D.10: Depth-density profile at 220 K

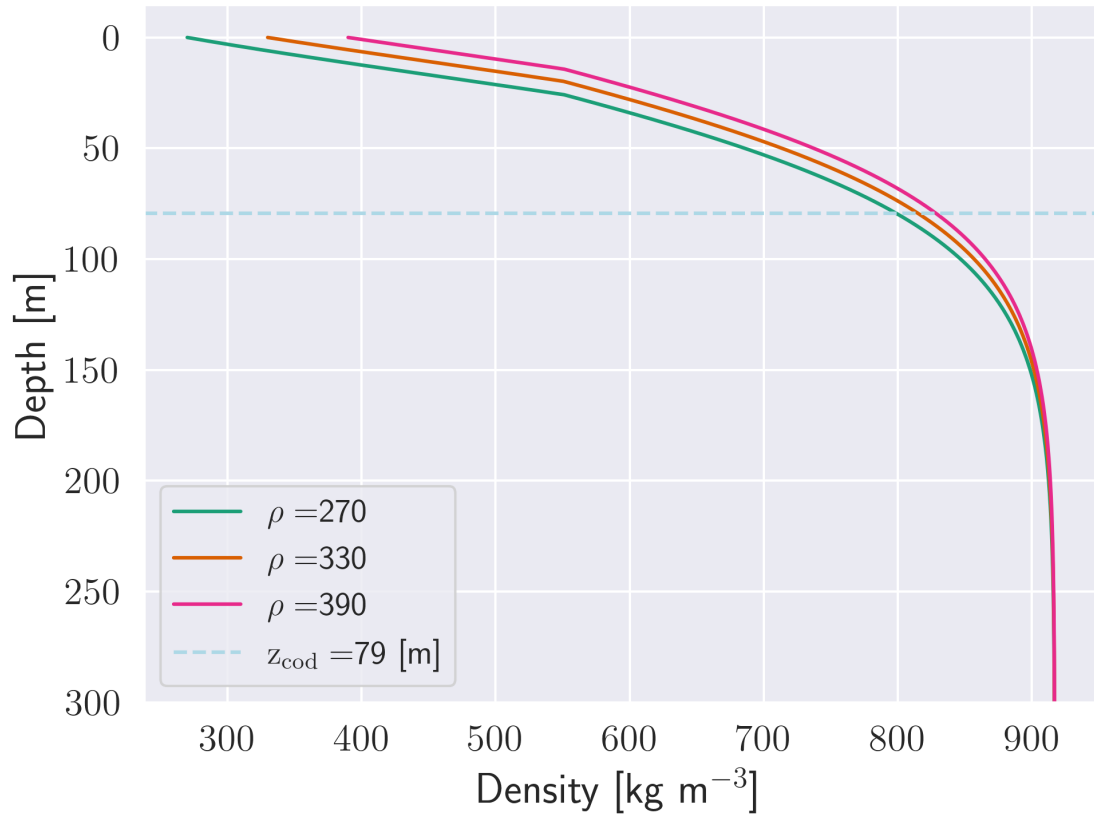


Figure D.11: Depth-density profile at 230 K

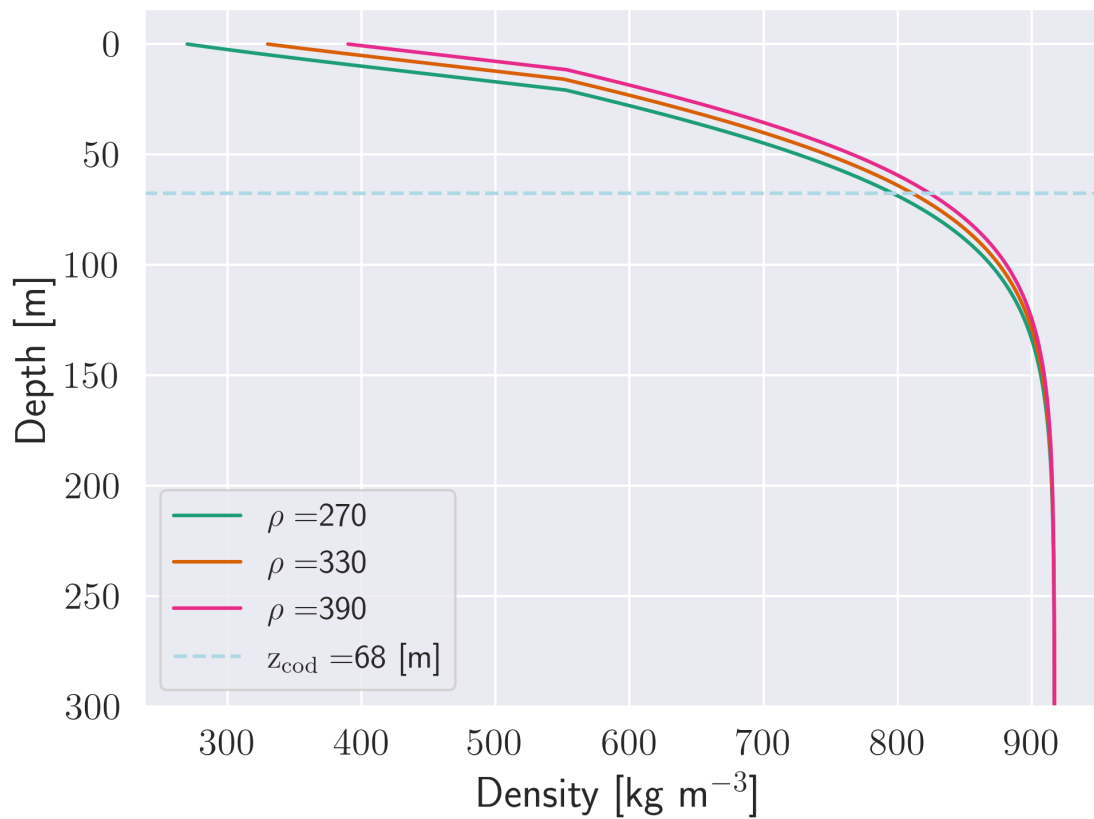


Figure D.12: Depth-density profile at 240 K

D.4 Influence of Diffusivity parameterization

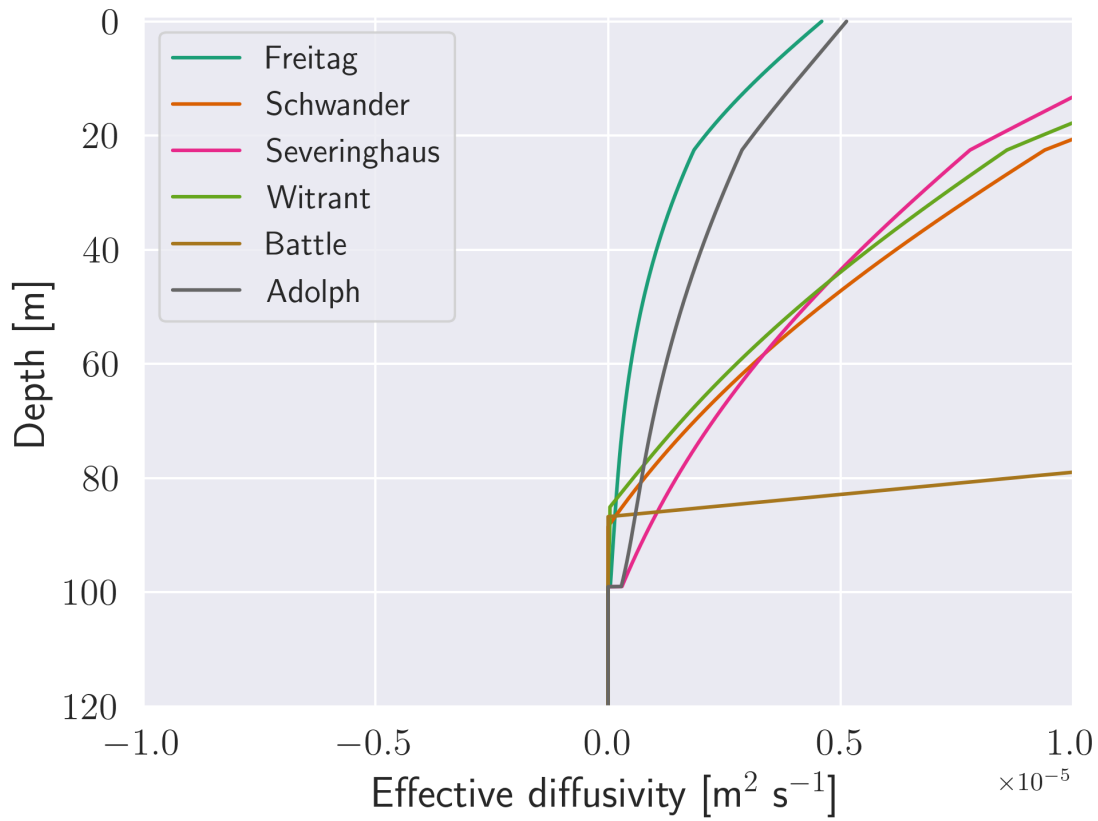


Figure D.13: Depth-diffusivity profile at 220 K

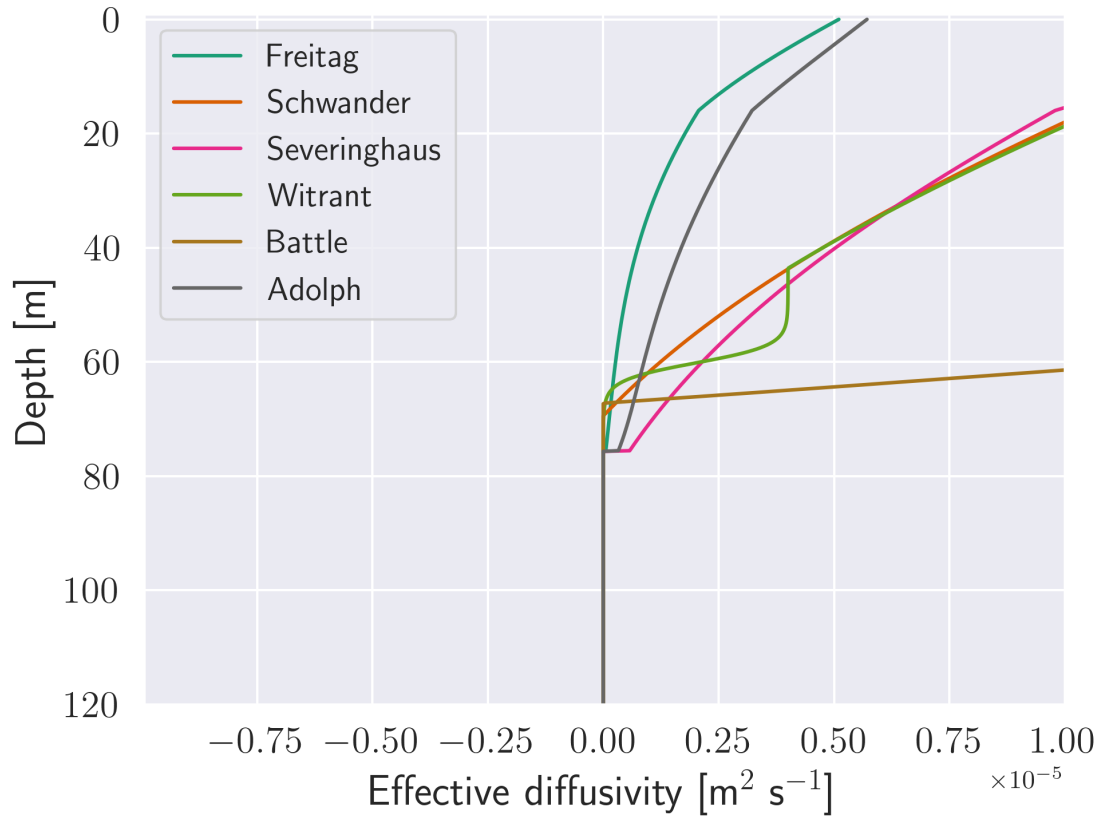


Figure D.14: Depth-diffusivity profile at 234 K

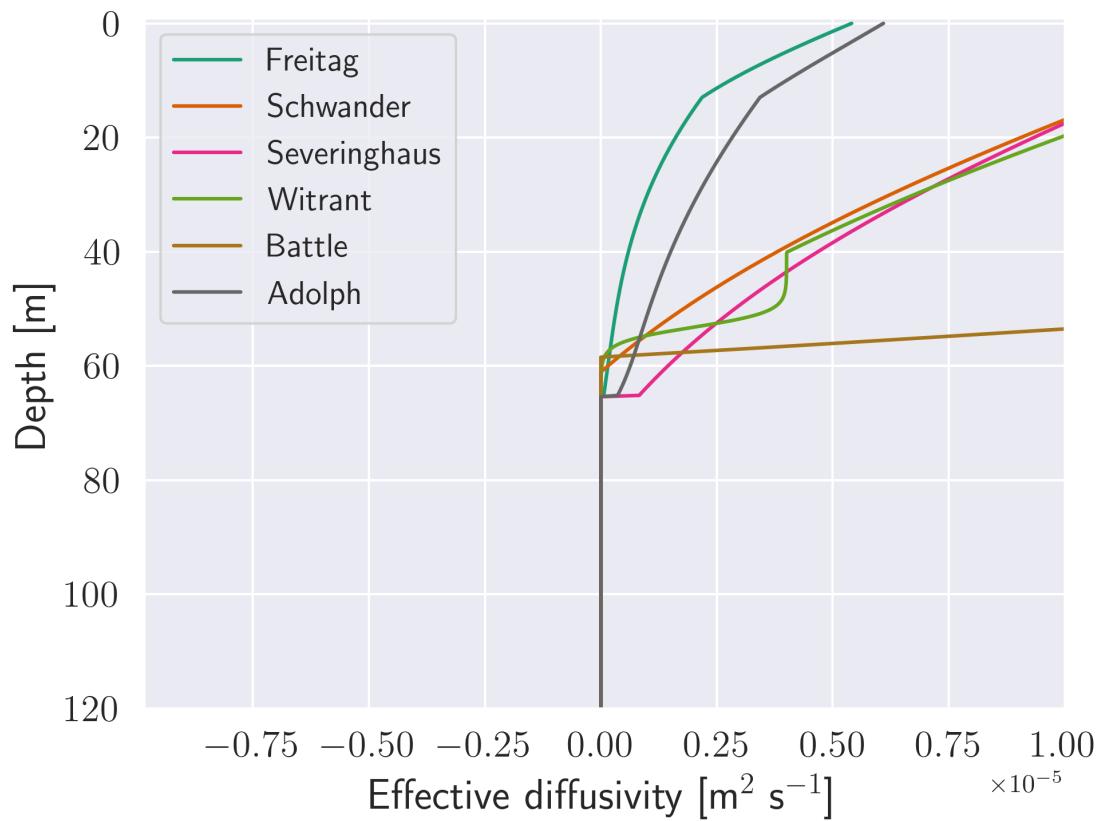


Figure D.15: Depth-diffusivity profile at 244 K

Additional plots for changing forcing Halfway-time **E**

E.1 Changing duration

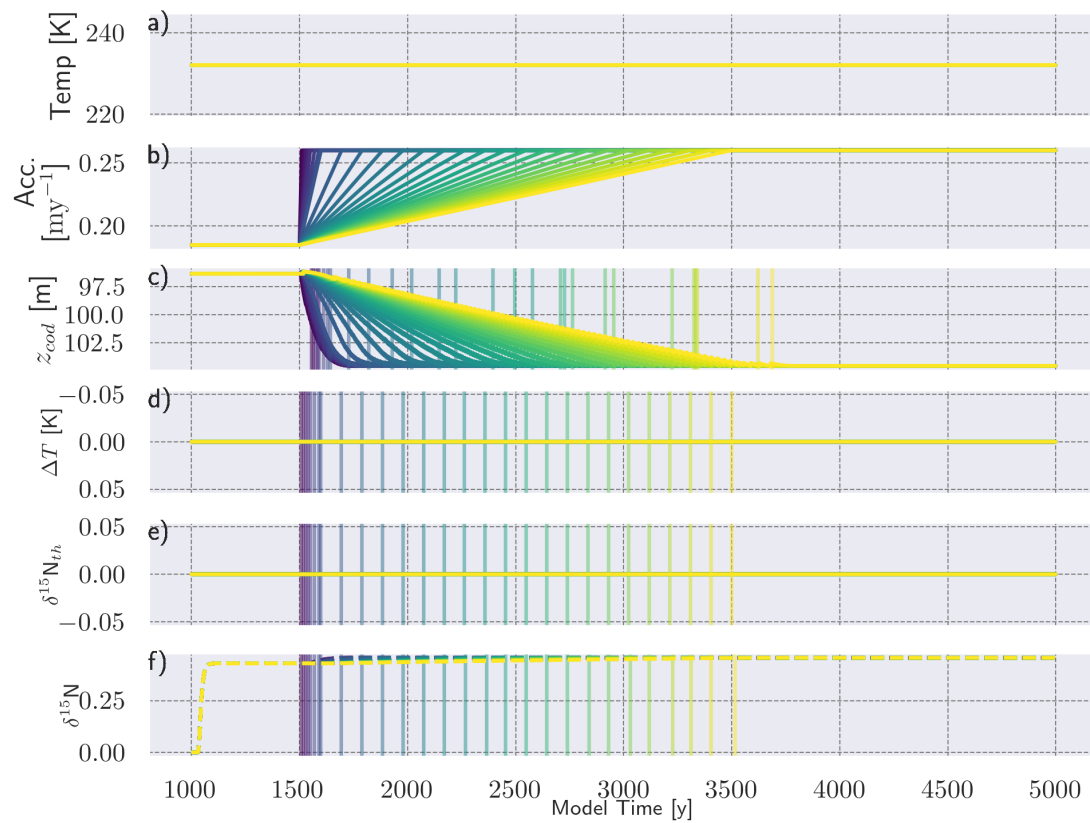


Figure E.1: Response of CFM for changes in duration of Acc

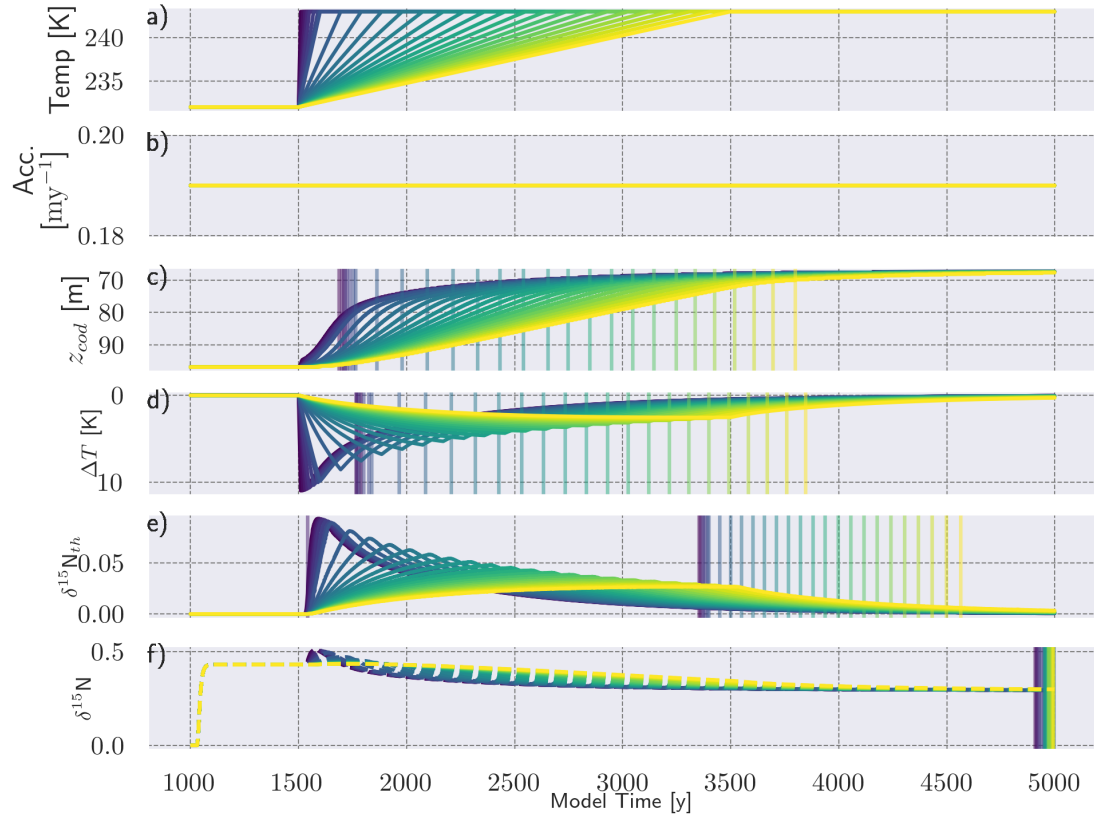


Figure E.2: Response of CFM for changes in duration in Temp

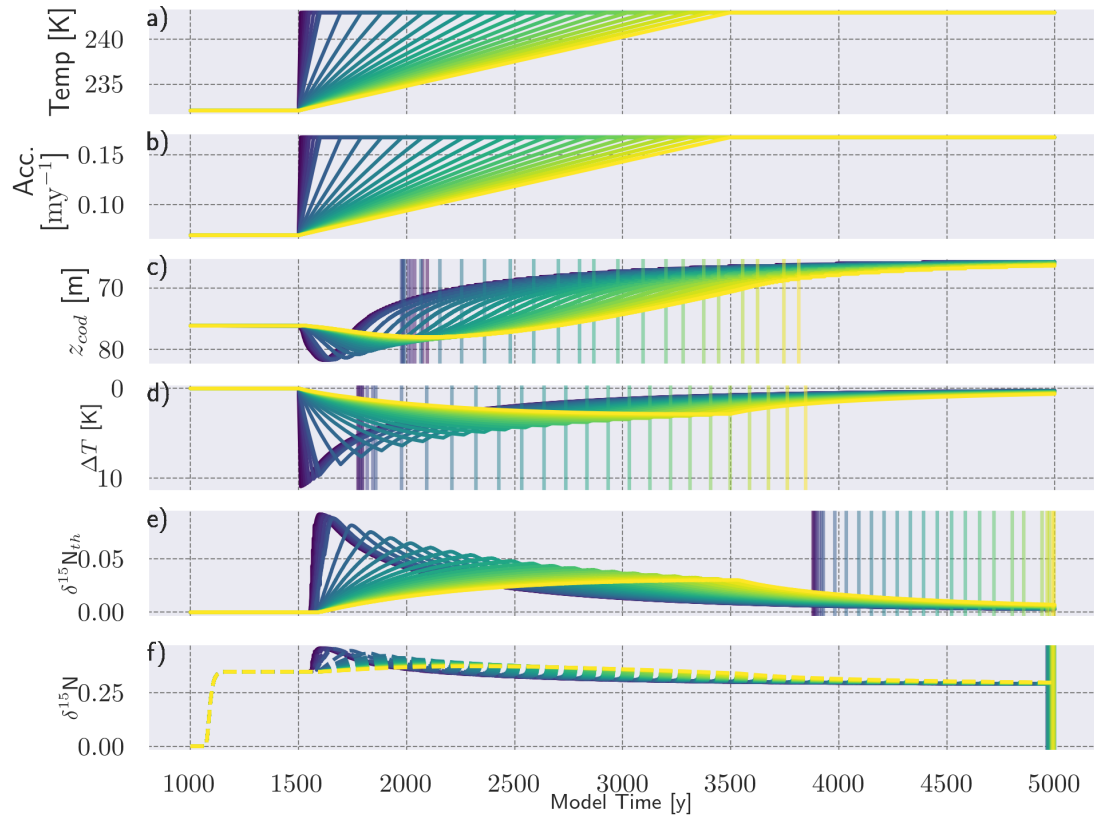


Figure E.3: Response of CFM for changes in duration in both

E.2 Changing magnitude

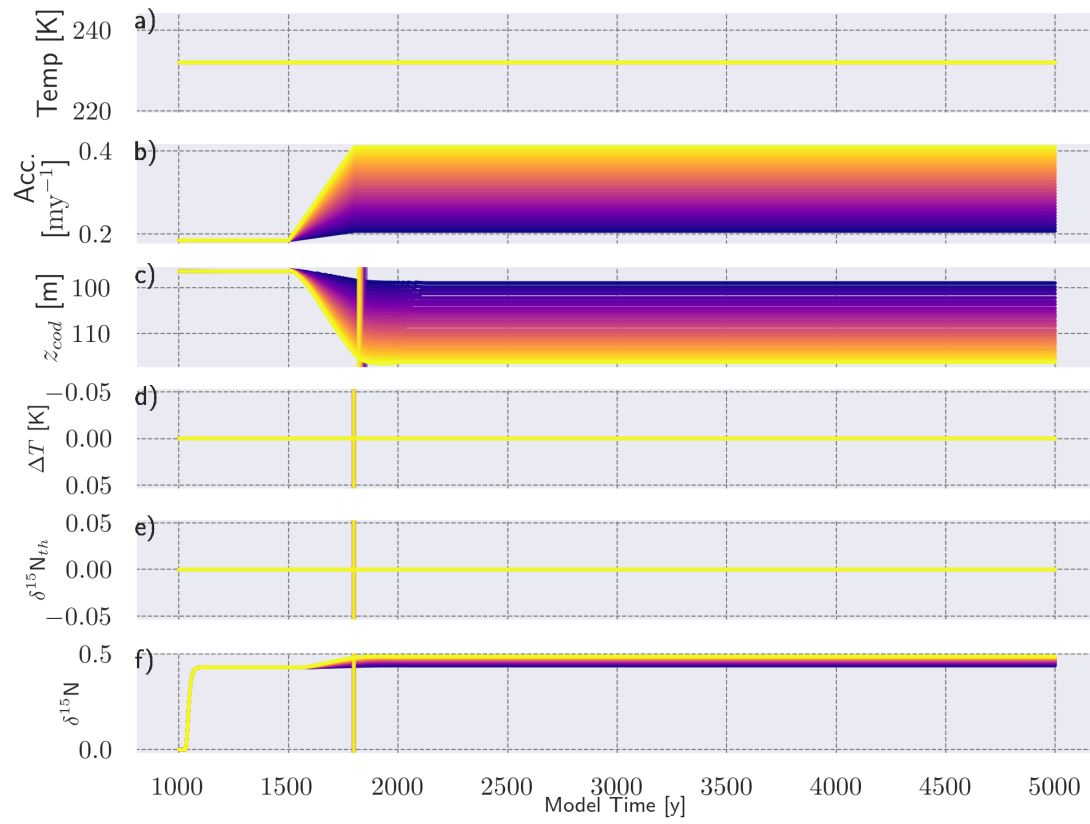


Figure E.4: Response of CFM for changes in magnitude of Acc

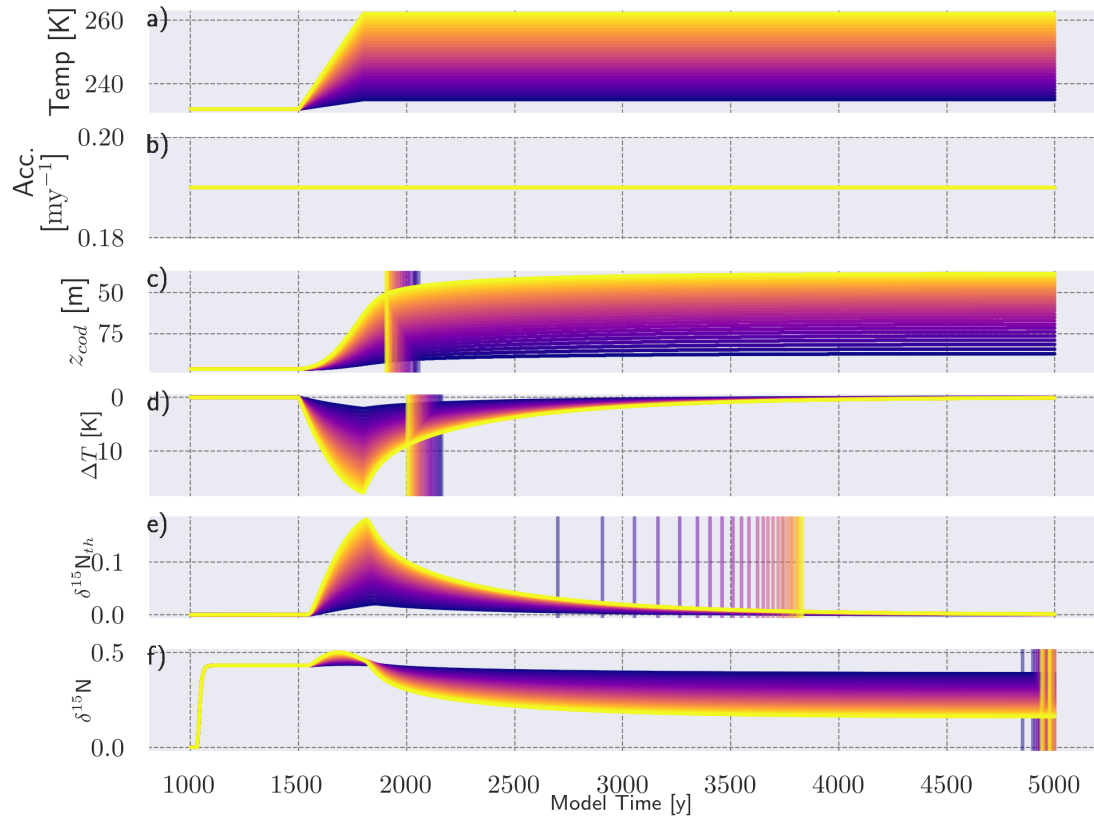


Figure E.5: Response of CFM for changes in magnitude in Temp

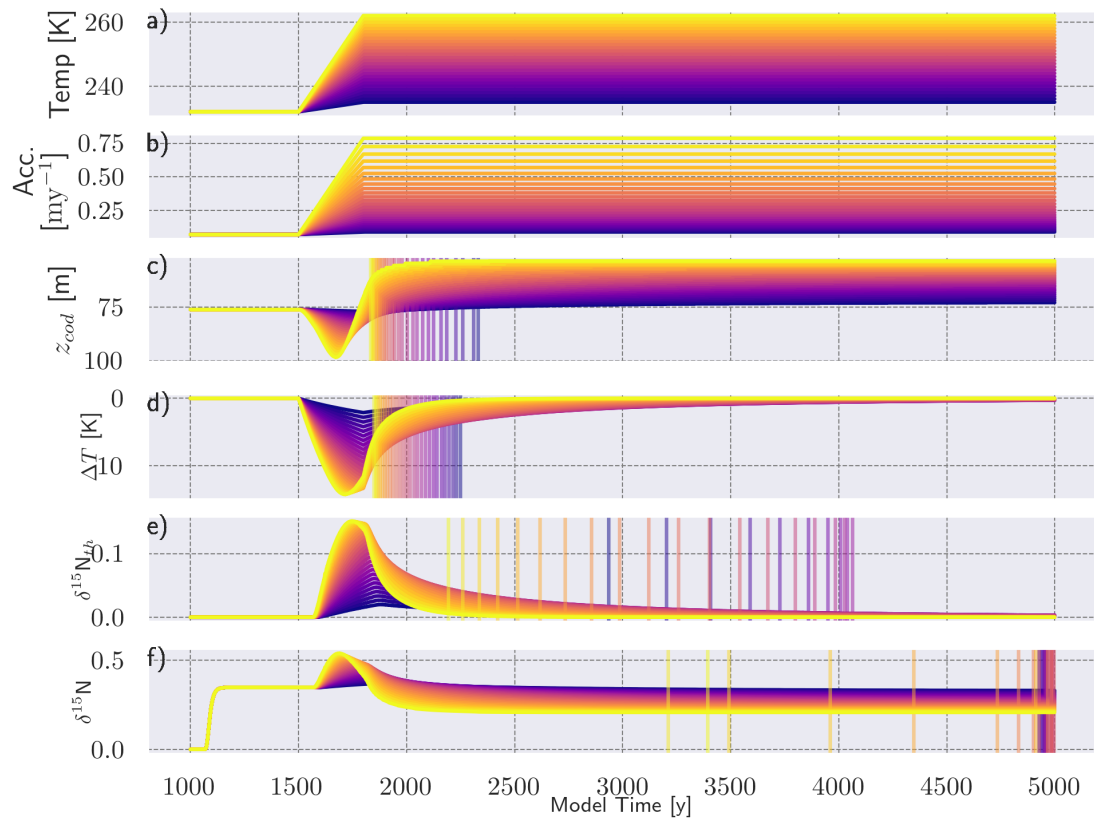


Figure E.6: Response of CFM for changes in magnitude in both

Additional plots for changing forcing

Equilibrium time **F**

F.1 Changing duration

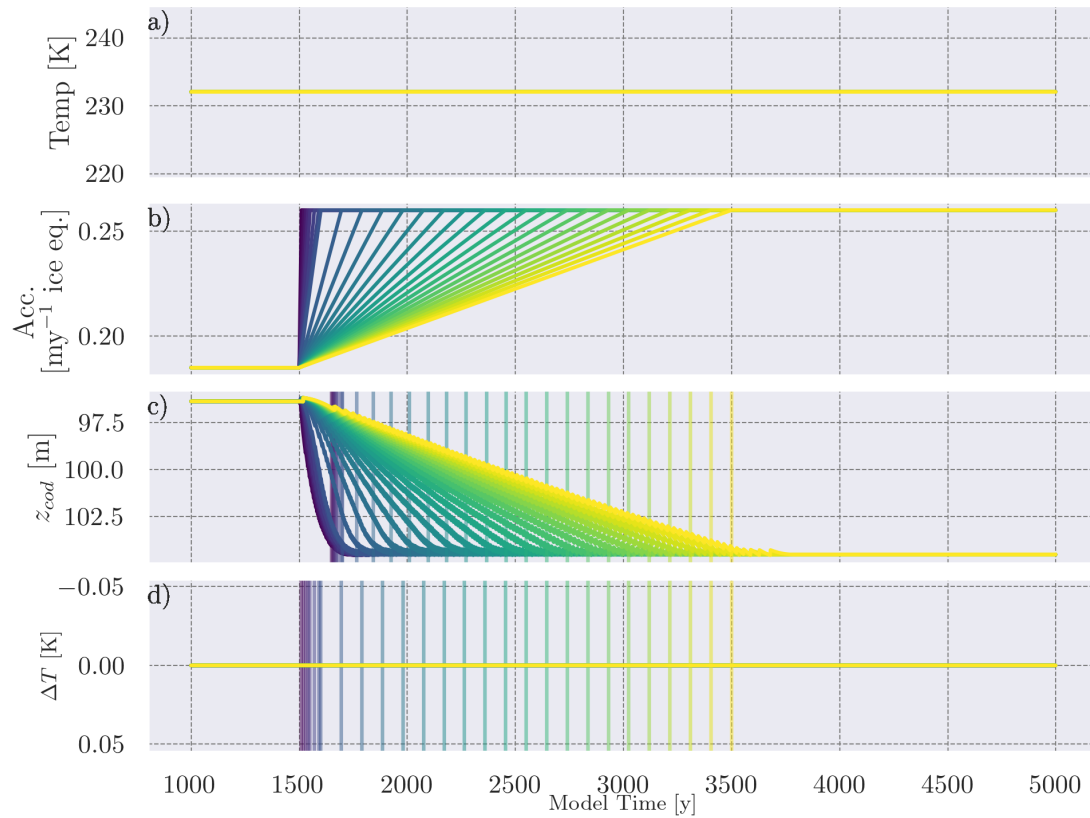


Figure F.1: Response of CFM for changes in duration of Acc

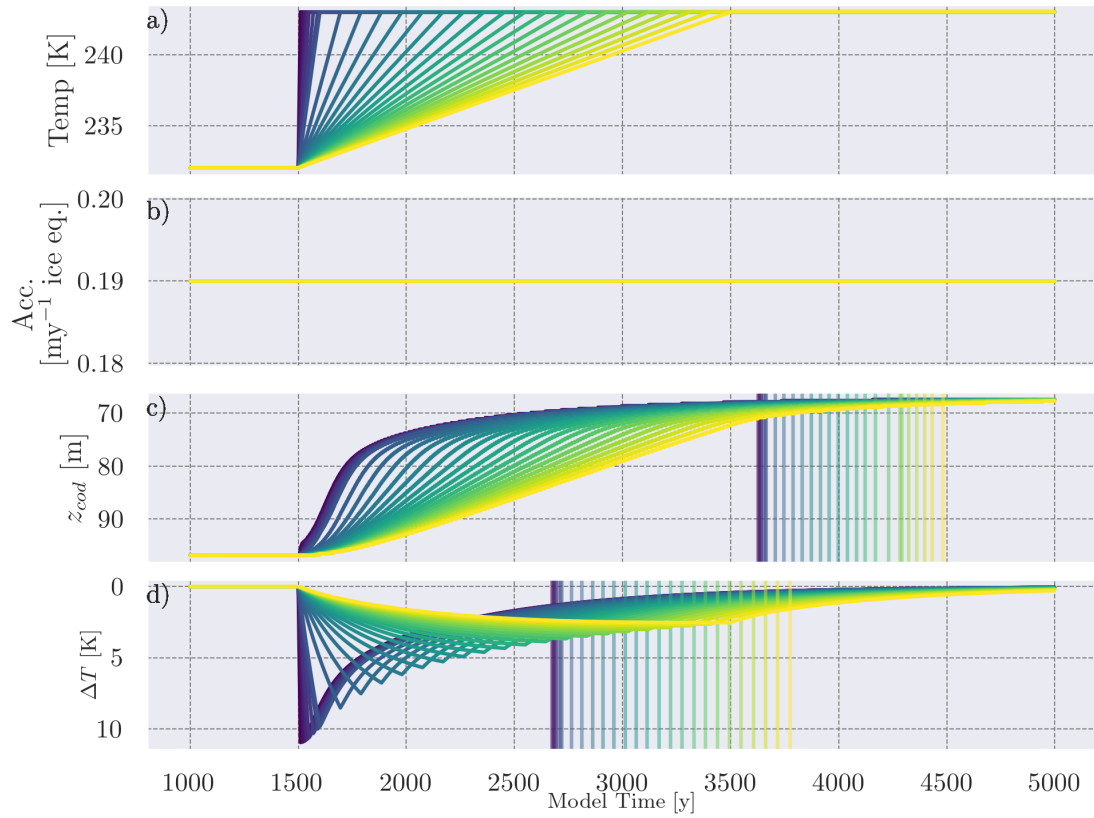


Figure F.2: Response of CFM for changes in duration in Temp

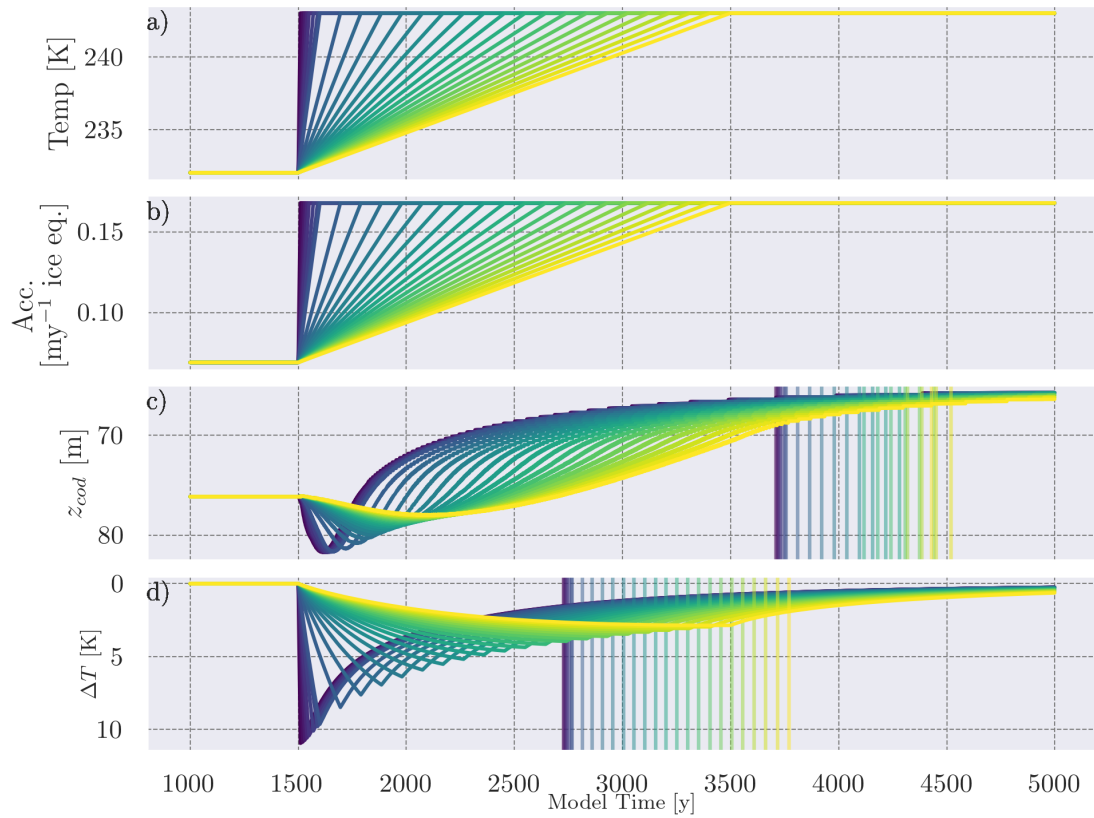


Figure F.3: Response of CFM for changes in duration in both

F.2 Changing duration

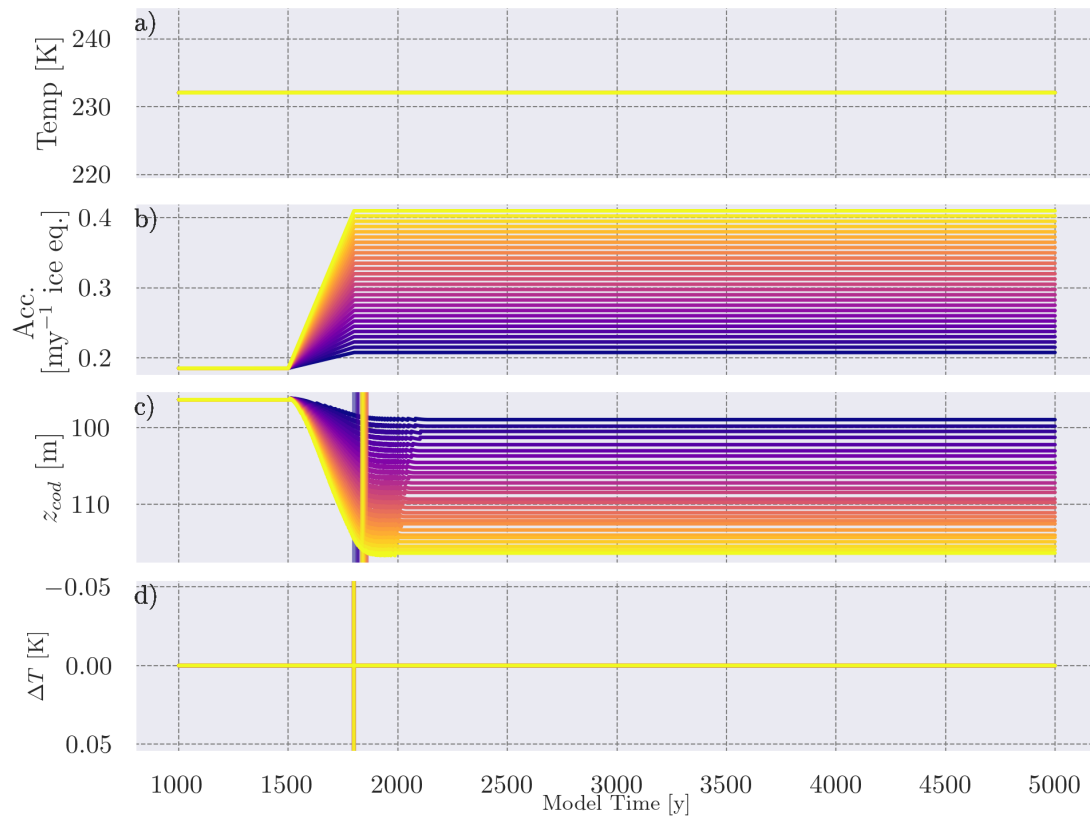


Figure F.4: Response of CFM for changes in magnitude of Acc

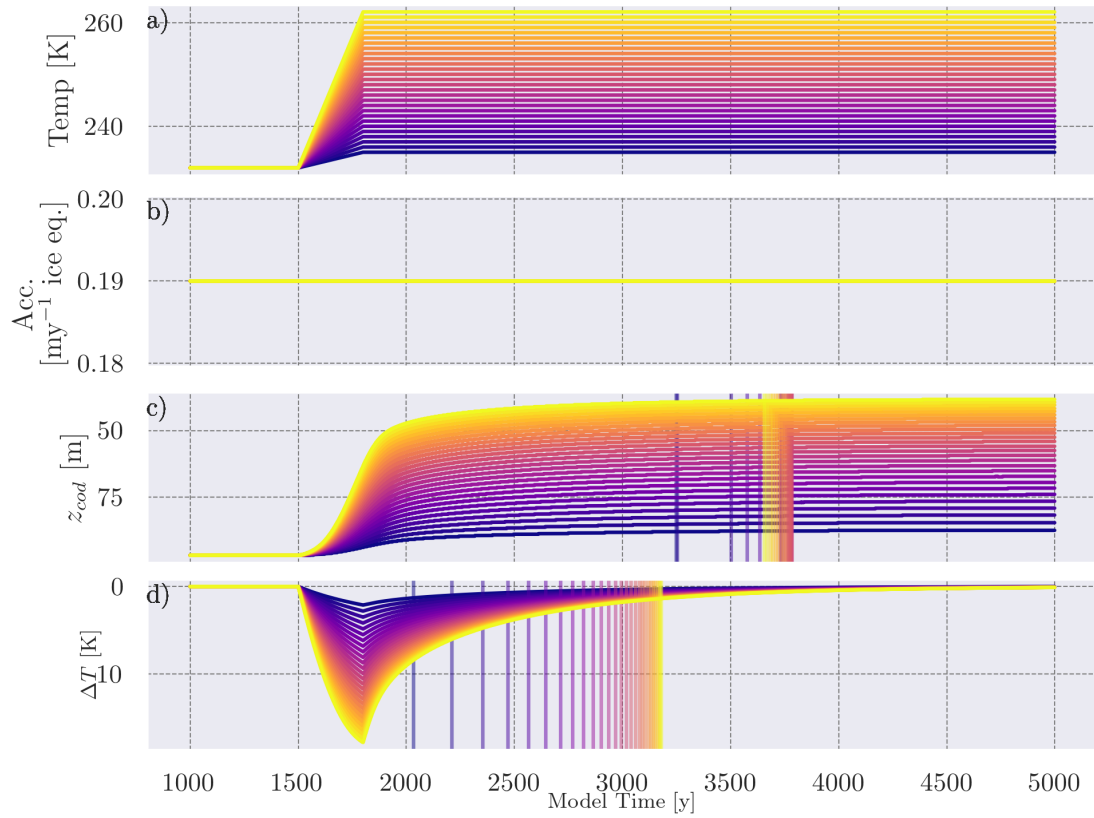


Figure F.5: Response of CFM for changes in magnitude in Temp

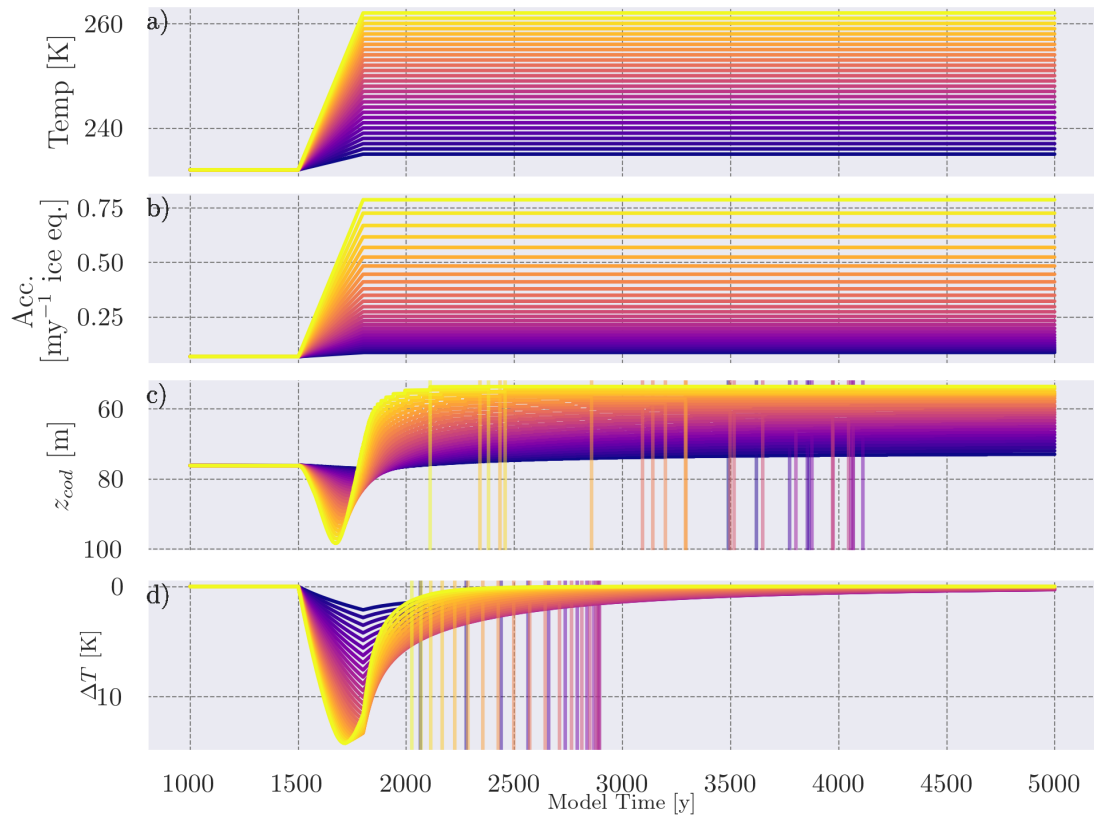


Figure F.6: Response of CFM for changes in magnitude in both

Bibliography

Here are the references in citation order.

- [1] *fmarotta/kaobook: A LaTeX class for books*. URL: <https://github.com/fmarotta/kaobook> (cited on page xiv).
- [2] G. a. K. Arroyo Ochori. 'Higher-dimensional modelling of geographic information'. PhD thesis. 2016. (Visited on 05/22/2023) (cited on page xiv).
- [3] Edward R. Tufte. *The Visual Display of Quantitative Information, 2nd Ed.* 2nd edition. Cheshire, Conn: Graphics Press, Feb. 2001. 200 pp. (cited on page xiv).
- [4] Matthew Butterick. *Practical Typography*. 2023. URL: <https://practicaltypography.com> (visited on 05/22/2023) (cited on page xiv).
- [5] Chester C. Langway. 'The history of early polar ice cores'. en. In: *Cold Regions Science and Technology*. Research in Cryospheric Science and Engineering 52.2 (Apr. 2008), pp. 101–117. DOI: [10.1016/j.coldregions.2008.01.001](https://doi.org/10.1016/j.coldregions.2008.01.001). (Visited on 05/15/2023) (cited on page 1).
- [6] E. Sorge. 'Glaziologische Untersuchungen in Eismitte'. In: *Wissenschaftliche Ergebnisse der Deutschen Gronland-Expedition Alfred-Wegener 1929 und 1930-1931* 3 (1935), p. 270. (Visited on 05/15/2023) (cited on page 1).
- [7] J. Jouzel. 'A brief history of ice core science over the last 50 yr'. In: *Climate of the Past* 9.6 (2013), pp. 2525–2547. DOI: [10.5194/cp-9-2525-2013](https://doi.org/10.5194/cp-9-2525-2013) (cited on page 1).
- [8] Valter Schytt. 'Scientific Results: Norwegian-British-Swedish Antarctic Expedition, 1949-52. Glaciology. Snow studies at Maudheim. Vol. 4. 2,A-C'. en. In: *Norwegian-British-Swedish Antarctic Expedition 1949-1952*. Google-Books-ID: AXd3zQEACAAJ. Norsk Polarinst., 1958 (cited on page 1).
- [9] C. Swithinbank. 'Scientific Results 3. Glaciology I'. en. In: *Norwegian-British-Swedish Antarctic Expedition 1949-1952*. Ed. by Norsk-britisk-svenske vitenskapelige ekspedisjon til Antarktis. Vol. 3. Norway: Norsk Polarinstitut, 1957 (cited on page 1).
- [10] M. M. Miller. 'Juneau Icefield Research Project, Alaska, 1950'. In: *American Geographical Society* 7 (1954) (cited on page 1).
- [11] Gérard Galibert. 'Groenland : J.-C. Heuberger, Forages sur l'Inlandsis ; A. Bauer, Le glacier de l'Éque'. fre. In: *Revue géographique des Pyrénées et du Sud-Ouest. Sud-Ouest Européen* 28.1 (1957), pp. 91–93. (Visited on 05/15/2023) (cited on page 1).
- [12] Chester C. Langway. 'A 400 Meter Deep Ice Core in Greenland: Preliminary Report'. en. In: *Journal of Glaciology* 3.23 (1958), pp. 217–217. DOI: [10.3189/S0022143000024278](https://doi.org/10.3189/S0022143000024278). (Visited on 05/15/2023) (cited on page 1).
- [13] William F. Ruddiman. *Earth's Climate: Past and Future*. en. W. H. Freeman, 2008 (cited on pages 1, 3).
- [14] NGRIP members. 'High-resolution record of Northern Hemisphere climate extending into the last interglacial period'. en. In: *Nature* 431.7005 (Sept. 2004), pp. 147–151. DOI: [10.1038/nature02805](https://doi.org/10.1038/nature02805). (Visited on 05/08/2023) (cited on pages 1, 32, 33).
- [15] W. Dansgaard. 'The Abundance of O18 in Atmospheric Water and Water Vapour'. en. In: *Tellus* 5.4 (1953), pp. 461–469. DOI: [10.1111/j.2153-3490.1953.tb01076.x](https://doi.org/10.1111/j.2153-3490.1953.tb01076.x). (Visited on 05/15/2023) (cited on pages 1, 4).

- [16] W. Dansgaard. 'Stable isotopes in precipitation'. en. In: *Tellus* 16.4 (1964), pp. 436–468. DOI: [10.1111/j.2153-3490.1964.tb00181.x](https://doi.org/10.1111/j.2153-3490.1964.tb00181.x). (Visited on 03/07/2023) (cited on pages 1, 3, 4).
- [17] Hansi A. Singh, David S. Battisti, and Cecilia M. Bitz. 'A Heuristic Model of Dansgaard–Oeschger Cycles. Part I: Description, Results, and Sensitivity Studies'. EN. In: *Journal of Climate* 27.12 (June 2014), pp. 4337–4358. DOI: [10.1175/JCLI-D-12-00672.1](https://doi.org/10.1175/JCLI-D-12-00672.1). (Visited on 05/15/2023) (cited on page 1).
- [18] H. C. Steen-Larsen and D. Dahl-Jensen. 'Modelling binge–purge oscillations of the Laurentide ice sheet using a plastic ice sheet'. en. In: *Annals of Glaciology* 48 (2008), pp. 177–182. DOI: [10.3189/172756408784700635](https://doi.org/10.3189/172756408784700635). (Visited on 05/15/2023) (cited on page 1).
- [19] Gary Shaffer, Steffen Malskær Olsen, and Christian J. Bjerrum. 'Ocean subsurface warming as a mechanism for coupling Dansgaard-Oeschger climate cycles and ice-raftering events'. en. In: *Geophysical Research Letters* 31.24 (2004). DOI: [10.1029/2004GL020968](https://doi.org/10.1029/2004GL020968). (Visited on 05/15/2023) (cited on page 1).
- [20] Bradley R. Markle et al. 'Global atmospheric teleconnections during Dansgaard–Oeschger events'. en. In: *Nature Geoscience* 10.1 (Jan. 2017), pp. 36–40. DOI: [10.1038/ngeo2848](https://doi.org/10.1038/ngeo2848). (Visited on 05/15/2023) (cited on page 1).
- [21] J. B. Pedro et al. 'Dansgaard-Oeschger and Heinrich event temperature anomalies in the North Atlantic set by sea ice, frontal position and thermocline structure'. en. In: *Quaternary Science Reviews* 289 (Aug. 2022), p. 107599. DOI: [10.1016/j.quascirev.2022.107599](https://doi.org/10.1016/j.quascirev.2022.107599). (Visited on 05/15/2023) (cited on page 1).
- [22] Camille Li and Andreas Born. 'Coupled atmosphere-ice-ocean dynamics in Dansgaard-Oeschger events'. en. In: *Quaternary Science Reviews* 203 (Jan. 2019), pp. 1–20. DOI: [10.1016/j.quascirev.2018.10.031](https://doi.org/10.1016/j.quascirev.2018.10.031). (Visited on 05/15/2023) (cited on page 1).
- [23] P. Kindler et al. 'Temperature reconstruction from 10 to 120 kyr b2k from the NGRIP ice core'. In: *Climate of the Past* 10.2 (2014), pp. 887–902. DOI: [10.5194/cp-10-887-2014](https://doi.org/10.5194/cp-10-887-2014) (cited on pages 1, 2, 4, 7, 14, 23, 31–35, 39–41, 44, 48, 51, 55, 57, 60, 65–67).
- [24] M. Döring and M. C. Leuenberger. 'Novel automated inversion algorithm for temperature reconstruction using gas isotopes from ice cores'. In: *Climate of the Past* 14.6 (2018), pp. 763–788. DOI: [10.5194/cp-14-763-2018](https://doi.org/10.5194/cp-14-763-2018) (cited on pages 1, 4).
- [25] Vasileios Gkinis et al. 'Numerical experiments on firn isotope diffusion with the Community Firn Model'. en. In: *Journal of Glaciology* 67.263 (June 2021), pp. 450–472. DOI: [10.1017/jog.2021.1](https://doi.org/10.1017/jog.2021.1). (Visited on 03/07/2023) (cited on pages 1, 26, 27, 34, 35).
- [26] Katharina Scheidt. 'Modeling Paleotemperatures from Stable Nitrogen Isotopes with the Community Firn Model'. en. MA thesis. Center for Ice and Climate, Sept. 1, 2022. (Visited on 05/01/2023) (cited on pages 1, 6, 26, 27, 31, 61, 65–67).
- [27] K. K. Andersen et al. 'Retrieving a common accumulation record from Greenland ice cores for the past 1800 years'. In: *Journal of Geophysical Research: Atmospheres* 111 (D15 2006). DOI: [10.1029/2005JD006765](https://doi.org/10.1029/2005JD006765). (Visited on 05/19/2023) (cited on page 3).
- [28] S. O. Rasmussen et al. 'Early Holocene climate oscillations recorded in three Greenland ice cores'. In: *Quaternary Science Reviews*. Early Holocene climate oscillations - causes and consequences 26.15 (Aug. 2007), pp. 1907–1914. DOI: [10.1016/j.quascirev.2007.06.015](https://doi.org/10.1016/j.quascirev.2007.06.015). (Visited on 05/19/2023) (cited on page 3).
- [29] A. Svensson et al. 'Direct linking of Greenland and Antarctic ice cores at the Toba eruption (74 ka BP)'. In: *Climate of the Past* 9.2 (2013), pp. 749–766. DOI: [10.5194/cp-9-749-2013](https://doi.org/10.5194/cp-9-749-2013) (cited on page 3).

- [30] Eliza Cook et al. 'Volcanism and the Greenland ice cores: A new tephrochronological framework for the last glacial-interglacial transition (LGIT) based on cryptotephra deposits in three ice cores'. en. In: *Quaternary Science Reviews* 292 (Sept. 2022), p. 107596. DOI: [10.1016/j.quascirev.2022.107596](https://doi.org/10.1016/j.quascirev.2022.107596). (Visited on 05/19/2023) (cited on page 3).
- [31] V. A. Levchenko et al. 'The ^{14}C "bomb spike" determines the age spread and age of CO_2 in Law Dome firn and ice'. In: *Geophysical Research Letters* 23.23 (1996), pp. 3345–3348. DOI: [10.1029/96GL03156](https://doi.org/10.1029/96GL03156). (Visited on 05/19/2023) (cited on page 3).
- [32] D. M. Etheridge et al. 'Natural and anthropogenic changes in atmospheric CO_2 over the last 1000 years from air in Antarctic ice and firn'. In: *Journal of Geophysical Research: Atmospheres* 101 (D2 1996), pp. 4115–4128. DOI: [10.1029/95JD03410](https://doi.org/10.1029/95JD03410). (Visited on 05/19/2023) (cited on page 3).
- [33] R. Spahni et al. 'The attenuation of fast atmospheric CH_4 variations recorded in polar ice cores'. In: *Geophysical Research Letters* 30.11 (2003). DOI: [10.1029/2003GL017093](https://doi.org/10.1029/2003GL017093). (Visited on 05/19/2023) (cited on page 3).
- [34] C. MacFarling Meure et al. 'Law Dome CO_2 , CH_4 and N_2O ice core records extended to 2000 years BP'. In: *Geophysical Research Letters* 33.14 (2006). DOI: [10.1029/2006GL026152](https://doi.org/10.1029/2006GL026152). (Visited on 05/19/2023) (cited on page 3).
- [35] Heather Goss. *Cutting to the Core*. June 2021. URL: <http://eos.org/agu-news/cutting-to-the-core> (visited on 05/22/2023) (cited on page 3).
- [36] Carol Kendall and Eric A. Caldwell. 'Chapter 2 - Fundamentals of Isotope Geochemistry'. In: *Isotope Tracers in Catchment Hydrology*. Ed. by CAROL KENDALL and JEFFREY J. McDONNELL. Amsterdam: Elsevier, 1998, pp. 51–86. DOI: <https://doi.org/10.1016/B978-0-444-81546-0.50009-4> (cited on page 3).
- [37] Zachary Sharp. *Principles of Stable Isotope Geochemistry, 2nd Edition*. Jan. 2017 (cited on page 4).
- [38] Z. Liu et al. 'Reconstruction of Past Antarctic Temperature Using Present Seasonal d^{18}O -Inversion Layer Temperature: Unified Slope Equations and Applications'. EN. In: *Journal of Climate* 36.9 (Mar. 2023), pp. 2933–2957. DOI: [10.1175/JCLI-D-22-0012.1](https://doi.org/10.1175/JCLI-D-22-0012.1). (Visited on 05/19/2023) (cited on page 4).
- [39] Sigfus J. Johnsen et al. 'Greenland palaeotemperatures derived from GRIP bore hole temperature and ice core isotope profiles'. en-US. In: 47.5 (Jan. 1995), p. 624. DOI: [10.3402/tellusb.v47i5.16077](https://doi.org/10.3402/tellusb.v47i5.16077). (Visited on 05/08/2023) (cited on pages 4, 34, 35).
- [40] Kurt M. Cuffey and Gary D. Clow. 'Temperature, accumulation, and ice sheet elevation in central Greenland through the last deglacial transition'. en. In: *Journal of Geophysical Research: Oceans* 102.C12 (1997), pp. 26383–26396. DOI: [10.1029/96JC03981](https://doi.org/10.1029/96JC03981). (Visited on 05/19/2023) (cited on page 4).
- [41] Christof Huber et al. 'Isotope calibrated Greenland temperature record over Marine Isotope Stage 3 and its relation to CH_4 '. en. In: *Earth and Planetary Science Letters* 243.3 (Mar. 2006), pp. 504–519. DOI: [10.1016/j.epsl.2006.01.002](https://doi.org/10.1016/j.epsl.2006.01.002). (Visited on 05/08/2023) (cited on pages 4, 33).
- [42] J. Jouzel et al. 'Magnitude of isotope/temperature scaling for interpretation of central Antarctic ice cores'. en. In: *Journal of Geophysical Research: Atmospheres* 108.D12 (2003). DOI: [10.1029/2002JD002677](https://doi.org/10.1029/2002JD002677). (Visited on 05/15/2023) (cited on pages 4, 60).
- [43] M. A. Ahmadi and A. Bahadori. 'Chapter Eight - Gas Hydrates'. en. In: *Fluid Phase Behavior for Conventional and Unconventional Oil and Gas Reservoirs*. Ed. by Alireza Bahadori. Boston: Gulf Professional Publishing, Jan. 2017, pp. 405–444. DOI: [10.1016/B978-0-12-803437-8.00008-7](https://doi.org/10.1016/B978-0-12-803437-8.00008-7). (Visited on 05/19/2023) (cited on page 4).

- [44] F. Pauer et al. 'Air clathrate crystals from the GRIP deep ice core, Greenland: a number-, size- and shape-distribution study'. en. In: *Journal of Glaciology* 45.149 (1999), pp. 22–30. DOI: [10.3189/S0022143000003002](https://doi.org/10.3189/S0022143000003002). (Visited on 05/19/2023) (cited on page 4).
- [45] Hiroshi Ohno, Vladimir Ya Lipenkov, and Takeo Hondoh. 'Formation of air clathrate hydrates in polar ice sheets: heterogeneous nucleation induced by micro-inclusions'. en. In: *Journal of Glaciology* 56.199 (2010), pp. 917–921. DOI: [10.3189/002214310794457317](https://doi.org/10.3189/002214310794457317). (Visited on 05/19/2023) (cited on pages 4, 5).
- [46] Michael R. House. 'Orbital forcing timescales: an introduction'. In: *Geological Society, London, Special Publications* 85.1 (Jan. 1995), pp. 1–18. DOI: [10.1144/GSL.SP.1995.085.01.01](https://doi.org/10.1144/GSL.SP.1995.085.01.01). (Visited on 04/28/2023) (cited on page 4).
- [47] André Mariotti. 'Atmospheric nitrogen is a reliable standard for natural ^{15}N abundance measurements'. en. In: *Nature* 303.5919 (June 1983), pp. 685–687. DOI: [10.1038/303685a0](https://doi.org/10.1038/303685a0). (Visited on 04/28/2023) (cited on page 4).
- [48] K. Fourteau et al. 'Historical porosity data in polar firn'. In: *Earth System Science Data* 12.2 (2020), pp. 1171–1177. DOI: [10.5194/essd-12-1171-2020](https://doi.org/10.5194/essd-12-1171-2020) (cited on page 5).
- [49] Jakob Schwander. 'The transformation of snow to ice and the occlusion of gases'. eng. In: *Schwander, Jakob (1989). The transformation of snow to ice and the occlusion of gases. In: Oeschger, H.; Langway, C. C. (eds.) The environmental record in glaciers and ice sheets. Physical, Chemical, and Earth Sciences Research Report: Vol. 8 (pp. 53-67). John Wiley & Sons. Ed. by H. Oeschger and C. C. Langway. Vol. 8. John Wiley & Sons, 1989, pp. 53–67.* (Visited on 04/25/2023) (cited on pages 5, 14).
- [50] C. Buizert et al. 'Gas transport in firn: multiple-tracer characterisation and model intercomparison for NEEM, Northern Greenland'. In: *Atmospheric Chemistry and Physics* 12.9 (2012), pp. 4259–4277. DOI: [10.5194/acp-12-4259-2012](https://doi.org/10.5194/acp-12-4259-2012) (cited on pages 5, 6, 16, 17, 19).
- [51] C. Goujon, J.-M. Barnola, and C. Ritz. 'Modeling the densification of polar firn including heat diffusion: Application to close-off characteristics and gas isotopic fractionation for Antarctica and Greenland sites'. en. In: *Journal of Geophysical Research: Atmospheres* 108.D24 (2003). DOI: [10.1029/2002JD003319](https://doi.org/10.1029/2002JD003319). (Visited on 04/22/2023) (cited on pages 5, 7, 11, 12).
- [52] C. Buizert. 'ICE CORE METHODS | Studies of Firn Air'. en. In: ed. by Scott A. Elias and Cary J. Mock. Amsterdam: Elsevier, Jan. 2013, pp. 361–372. DOI: [10.1016/B978-0-444-53643-3.00330-7](https://doi.org/10.1016/B978-0-444-53643-3.00330-7). (Visited on 04/15/2023) (cited on page 6).
- [53] Jeffrey P. Severinghaus, Alexi Grachev, and Mark Battle. 'Thermal fractionation of air in polar firn by seasonal temperature gradients'. en. In: *Geochemistry, Geophysics, Geosystems* 2.7 (2001). DOI: [10.1029/2000GC000146](https://doi.org/10.1029/2000GC000146). (Visited on 04/27/2023) (cited on pages 6, 14, 17).
- [54] Patricia Martinerie et al. 'Physical and climatic parameters which influence the air content in polar ice'. en. In: *Earth and Planetary Science Letters* 112.1-4 (Aug. 1992), pp. 1–13. DOI: [10.1016/0012-821X\(92\)90002-D](https://doi.org/10.1016/0012-821X(92)90002-D). (Visited on 03/07/2023) (cited on pages 6, 12, 28).
- [55] Michael M. Herron and Chester C. Langway. 'Firn Densification: An Empirical Model'. en. In: *Journal of Glaciology* 25.93 (1980), pp. 373–385. DOI: [10.3189/S0022143000015239](https://doi.org/10.3189/S0022143000015239). (Visited on 04/22/2023) (cited on pages 7, 9, 10).
- [56] Sepp Kipfstuhl et al. 'Air bubbles and Clathrate hydrates in the transition zone of the NGRIP Deep Ice Core'. In: *Geophysical Research Letters* 28.4 (2001), pp. 591–594. DOI: [10.1029/1999GL006094](https://doi.org/10.1029/1999GL006094). (Visited on 05/19/2023) (cited on page 7).

- [57] J. -M. Barnola et al. 'CO₂-climate relationship as deduced from the Vostok ice core: a re-examination based on new measurements and on a re-evaluation of the air dating'. en. In: *Tellus B* 43.2 (1991), pp. 83–90. DOI: [10.1034/j.1600-0889.1991.t01-1-00002.x](https://doi.org/10.1034/j.1600-0889.1991.t01-1-00002.x). (Visited on 04/22/2023) (cited on pages 7, 10, 11).
- [58] Jessica M. D. Lundin et al. 'Firn Model Intercomparison Experiment (FirnMICE)'. en. In: *Journal of Glaciology* 63.239 (June 2017), pp. 401–422. DOI: [10.1017/jog.2016.114](https://doi.org/10.1017/jog.2016.114). (Visited on 04/22/2023) (cited on pages 7, 9, 10).
- [59] Henri Bader. 'Sorge's Law of Densification of Snow on High Polar Glaciers'. en. In: *Journal of Glaciology* 2.15 (1954), pp. 319–323. DOI: [10.3189/S0022143000025144](https://doi.org/10.3189/S0022143000025144). (Visited on 04/22/2023) (cited on page 7).
- [60] V. Schytt and G. Robin. 'The Norwegian-British-Swedish Antarctic Expedition, 1949-52. 1. Summary of the glaciological work: preliminary report, by Valter Schytt. 2. Summary of seismic shooting investigations in Dronning Maud Land, by G. de Q. Robin'. In: 1953. (Visited on 04/22/2023) (cited on page 8).
- [61] Valter Schytt. 'Snow and ice studies in Antarctica'. eng. In: (1958). (Visited on 04/22/2023) (cited on page 8).
- [62] C. M. Stevens et al. 'The Community Firn Model (CFM) v1.0'. In: *Geoscientific Model Development* 13.9 (2020), pp. 4355–4377. DOI: [10.5194/gmd-13-4355-2020](https://doi.org/10.5194/gmd-13-4355-2020) (cited on pages 10–13, 16–18, 23, 24, 40, 41).
- [63] Pierre Pimienta. 'Étude du comportement mécanique des glaces polycristallines aux faibles contraintes : applications aux glaces des calottes polaires'. PhD thesis. Thèse de doctorat Mécanique Grenoble 1 1987 ; 168, Jan. 1987. (Visited on 04/22/2023) (cited on pages 10, 12).
- [64] Pierre Pimienta and Paul Duval. 'Mechanical behavior of anisotropic polar ice'. In: *The Physical Basis of Ice Sheet Modelling* 170 (Jan. 1987) (cited on page 10).
- [65] C. S. M. Doake and E. W. Wolff. 'Flow law for ice in polar ice sheets'. en. In: *Nature* 318.6041 (Nov. 1985), pp. 83–83. DOI: [10.1038/318083a0](https://doi.org/10.1038/318083a0). (Visited on 04/22/2023) (cited on page 10).
- [66] D. S Wilkinson and M. F Ashby. 'Pressure sintering by power law creep'. en. In: *Acta Metallurgica* 23.11 (Nov. 1975), pp. 1277–1285. DOI: [10.1016/0001-6160\(75\)90136-4](https://doi.org/10.1016/0001-6160(75)90136-4). (Visited on 04/22/2023) (cited on pages 10, 12).
- [67] H. Hansen et al. 'Additive manufacturing of metal components – process-material interaction in different process chains'. In: *IOP Conference Series: Materials Science and Engineering* 580 (Dec. 2019), p. 012006. DOI: [10.1088/1757-899X/580/1/012006](https://doi.org/10.1088/1757-899X/580/1/012006) (cited on page 10).
- [68] Laurent Arnaud, Jean M. Barnola, and Paul Duval. 'Physical modeling of the densification of snow/finn and ice in the upper part of polar ice sheets'. In: *Physics of Ice Core Records* (2000), pp. 285–305. (Visited on 04/23/2023) (cited on pages 11, 12).
- [69] Catherine Ritz. 'Interpretation of the Temperature Profile Measured at Vostok, East Antarctica'. en. In: *Annals of Glaciology* 12 (1989), pp. 138–144. DOI: [10.3189/S0260305500007102](https://doi.org/10.3189/S0260305500007102). (Visited on 04/23/2023) (cited on page 11).
- [70] R. B. Alley. 'FIRN DENSIFICATION BY GRAIN-BOUNDARY SLIDING : A FIRST MODEL'. en. In: *Le Journal de Physique Colloques* 48.C1 (Mar. 1987), pp. C1–256. DOI: [10.1051/jphyscol:1987135](https://doi.org/10.1051/jphyscol:1987135). (Visited on 04/23/2023) (cited on page 11).
- [71] Keishi Gotoh and John L. Finney. 'Statistical geometrical approach to random packing density of equal spheres'. en. In: *Nature* 252.5480 (Nov. 1974), pp. 202–205. DOI: [10.1038/252202a0](https://doi.org/10.1038/252202a0). (Visited on 04/25/2023) (cited on page 11).

- [72] Randall M. German. ‘Coordination number changes during powder densification’. en. In: *Powder Technology* 253 (Feb. 2014), pp. 368–376. DOI: [10.1016/j.powtec.2013.12.006](https://doi.org/10.1016/j.powtec.2013.12.006). (Visited on 04/25/2023) (cited on page 11).
- [73] Laurent Arnaud. ‘Modélisation de la transformation de la neige en glace à la surface des calottes polaires : étude du transport des gaz dans ces milieux poreux’. fr. PhD thesis. Université Joseph-Fourier - Grenoble I, June 1997. (Visited on 04/23/2023) (cited on page 12).
- [74] E. Arzt. ‘The influence of an increasing particle coordination on the densification of spherical powders’. en. In: *Acta Metallurgica* 30.10 (Oct. 1982), pp. 1883–1890. DOI: [10.1016/0001-6160\(82\)90028-1](https://doi.org/10.1016/0001-6160(82)90028-1). (Visited on 04/23/2023) (cited on page 12).
- [75] E. Arzt, M. F. Ashby, and K. E. Easterling. ‘Practical applications of hotisostatic Pressing diagrams: Four case studies’. en. In: *Metallurgical Transactions A* 14.1 (Feb. 1983), pp. 211–221. DOI: [10.1007/BF02651618](https://doi.org/10.1007/BF02651618). (Visited on 04/23/2023) (cited on page 12).
- [76] C. Buizert et al. ‘The WAIS Divide deep ice core WD2014 chronology—Part 1: Methane Synchronization (68–31 ka BP) and the gas age-ice age difference’. In: *Climate of the Past* 11 (Feb. 2015), pp. 153–173. DOI: [10.5194/cp-11-153-2015](https://doi.org/10.5194/cp-11-153-2015) (cited on page 12).
- [77] Suhas Patankar. *Numerical Heat Transfer and Fluid Flow*. Boca Raton: CRC Press, Oct. 1980 (cited on pages 13, 24–27, 43, 62).
- [78] H. Craig, Y. Horibe, and T. Sowers. ‘Gravitational Separation of Gases and Isotopes in Polar Ice Caps’. In: *Science* 242.4886 (Dec. 1988), pp. 1675–1678. DOI: [10.1126/science.242.4886.1675](https://doi.org/10.1126/science.242.4886.1675). (Visited on 03/07/2023) (cited on page 14).
- [79] Sydney Chapman and T. G. Cowling. *The Mathematical Theory of Non-uniform Gases: An Account of the Kinetic Theory of Viscosity, Thermal Conduction and Diffusion in Gases*. en. Google-Books-ID: ZloRtgEACAAJ. Cambridge University Press, May 1970 (cited on page 14).
- [80] M. C. Leuenberger, C. Lang, and J. Schwander. ‘Delta 15N measurements as a calibration tool for the paleothermometer and gas-ice age differences: A case study for the 8200 B.P. event on GRIP ice’. en. In: *Journal of Geophysical Research: Atmospheres* 104.D18 (1999), pp. 22163–22170. DOI: [10.1029/1999JD900436](https://doi.org/10.1029/1999JD900436). (Visited on 04/27/2023) (cited on pages 14, 15).
- [81] Gábor Lente and Katalin Ósz. ‘Barometric formulas: various derivations and comparisons to environmentally relevant observations’. en. In: *ChemTexts* 6.2 (Apr. 2020), p. 13. DOI: [10.1007/s40828-020-0111-6](https://doi.org/10.1007/s40828-020-0111-6). (Visited on 04/27/2023) (cited on page 14).
- [82] C. Lang et al. ‘16°C Rapid Temperature Variation in Central Greenland 70,000 Years Ago’. In: *Science* 286.5441 (Oct. 1999), pp. 934–937. DOI: [10.1126/science.286.5441.934](https://doi.org/10.1126/science.286.5441.934). (Visited on 04/27/2023) (cited on page 15).
- [83] V. Boersma-Klein and A. E. De Vries. ‘The influence of the distribution of atomic masses within the molecule on thermal diffusion: I. Isotopic CO and N₂ molecules’. en. In: *Physica* 32.4 (Apr. 1966), pp. 717–733. DOI: [10.1016/0031-8914\(66\)90004-8](https://doi.org/10.1016/0031-8914(66)90004-8). (Visited on 04/27/2023) (cited on page 15).
- [84] A. N. Davenport and E. R. S. Winter. ‘Diffusion properties of gases. Part V.—The thermal diffusion of carbon monoxide, nitrogen and methane’. en. In: *Transactions of the Faraday Society* 47.0 (Jan. 1951), pp. 1160–1169. DOI: [10.1039/TF9514701160](https://doi.org/10.1039/TF9514701160). (Visited on 04/27/2023) (cited on page 15).

- [85] Alexi Grachev and Jeff Severinghaus. ‘Laboratory determination of thermal diffusion constants for $^{29}\text{N}_2/^{28}\text{N}_2$ in air at temperatures from -60 to 0°C for reconstruction of magnitudes of abrupt climate changes using the ice core fossil-air palaeothermometer’. In: *Geochimica et Cosmochimica Acta* 67 (Feb. 2003). DOI: [10.1016/S0016-7037\(02\)01115-8](https://doi.org/10.1016/S0016-7037(02)01115-8) (cited on page 15).
- [86] J. Schwander et al. ‘The age of the air in the firn and the ice at Summit, Greenland’. en. In: *Journal of Geophysical Research: Atmospheres* 98.D2 (1993), pp. 2831–2838. DOI: [10.1029/92JD02383](https://doi.org/10.1029/92JD02383). (Visited on 04/27/2023) (cited on page 16).
- [87] R. Allan Freeze and John A. Cherry. *Groundwater*. en. Google-Books-ID: feVOAAAA-MAAJ. Prentice-Hall, 1979 (cited on pages 16, 18).
- [88] Vincent Rommelaere, Laurent Arnaud, and Jean-Marc Barnola. ‘Reconstructing recent atmospheric trace gas concentrations from polar firn and bubbly ice data by inverse methods’. en. In: *Journal of Geophysical Research: Atmospheres* 102.D25 (1997), pp. 30069–30083. DOI: [10.1029/97JD02653](https://doi.org/10.1029/97JD02653). (Visited on 04/27/2023) (cited on page 16).
- [89] Cathy Trudinger et al. ‘Modeling air movement and bubble trapping in firn’. In: *Journal of Geophysical Research* 102 (Mar. 1997), pp. 6747–6764. DOI: [10.1029/96JD03382](https://doi.org/10.1029/96JD03382) (cited on pages 16, 17).
- [90] Jeffrey P. Severinghaus et al. ‘Deep air convection in the firn at a zero-accumulation site, central Antarctica’. en. In: *Earth and Planetary Science Letters* 293.3 (May 2010), pp. 359–367. DOI: [10.1016/j.epsl.2010.03.003](https://doi.org/10.1016/j.epsl.2010.03.003). (Visited on 04/27/2023) (cited on page 16).
- [91] K. Kawamura et al. ‘Kinetic fractionation of gases by deep air convection in polar firn’. In: *Atmospheric Chemistry and Physics* 13.21 (2013), pp. 11141–11155. DOI: [10.5194/acp-13-11141-2013](https://doi.org/10.5194/acp-13-11141-2013) (cited on page 16).
- [92] C. Buizert and J. P. Severinghaus. ‘Dispersion in deep polar firn driven by synoptic-scale surface pressure variability’. In: *The Cryosphere* 10.5 (2016), pp. 2099–2111. DOI: [10.5194/tc-10-2099-2016](https://doi.org/10.5194/tc-10-2099-2016) (cited on pages 16, 18, 19).
- [93] B. Birner et al. ‘The influence of layering and barometric pumping on firn air transport in a 2-D model’. In: *The Cryosphere* 12.6 (2018), pp. 2021–2037. DOI: [10.5194/tc-12-2021-2018](https://doi.org/10.5194/tc-12-2021-2018) (cited on page 16).
- [94] Kenji Kawamura et al. ‘Convective mixing of air in firn at four polar sites’. en. In: *Earth and Planetary Science Letters* 244.3 (Apr. 2006), pp. 672–682. DOI: [10.1016/j.epsl.2006.02.017](https://doi.org/10.1016/j.epsl.2006.02.017). (Visited on 04/27/2023) (cited on page 16).
- [95] J. Schwander, B. Stauffer, and A. Sigg. ‘Air Mixing in Firn and the Age of the Air at Pore Close-Off’. en. In: *Annals of Glaciology* 10 (1988), pp. 141–145. DOI: [10.3189/S0260305500004328](https://doi.org/10.3189/S0260305500004328). (Visited on 04/27/2023) (cited on pages 17, 44, 45, 47).
- [96] T. R. Marrero and E. A. Mason. ‘Gaseous Diffusion Coefficients’. In: *Journal of Physical and Chemical Reference Data* 1.1 (Oct. 1972), pp. 3–118. DOI: [10.1063/1.3253094](https://doi.org/10.1063/1.3253094) (cited on page 17).
- [97] K. Schäfer et al., eds. *Transportphänomene ; I. Viskosität und Diffusion*. de. Google-Books-ID: TuRdwwEACAAJ. Springer, 1969 (cited on page 17).
- [98] M. Battle et al. ‘Atmospheric gas concentrations over the past century measured in air from firn at the South Pole’. en. In: *Nature* 383.6597 (Sept. 1996), pp. 231–235. DOI: [10.1038/383231a0](https://doi.org/10.1038/383231a0). (Visited on 04/27/2023) (cited on pages 17, 44, 45).

- [99] Johannes Freitag, Uwe Dobrindt, and Josef Kipfstuhl. ‘A new method for predicting transport properties of polar firn with respect to gases on the pore-space scale’. en. In: *Annals of Glaciology* 35 (2002), pp. 538–544. DOI: [10.3189/172756402781816582](https://doi.org/10.3189/172756402781816582). (Visited on 04/27/2023) (cited on pages 18, 45).
- [100] E. Witrant et al. ‘A new multi-gas constrained model of trace gas non-homogeneous transport in firn: evaluation and behaviour at eleven polar sites’. In: *Atmospheric Chemistry and Physics* 12.23 (2012), pp. 11465–11483. DOI: [10.5194/acp-12-11465-2012](https://doi.org/10.5194/acp-12-11465-2012) (cited on pages 18, 45).
- [101] A. C. Adolph and M. R. Albert. ‘Gas diffusivity and permeability through the firn column at Summit, Greenland: measurements and comparison to microstructural properties’. In: *The Cryosphere* 8.1 (2014), pp. 319–328. DOI: [10.5194/tc-8-319-2014](https://doi.org/10.5194/tc-8-319-2014) (cited on pages 18, 45).
- [102] Pauli Virtanen et al. ‘SciPy 1.0: fundamental algorithms for scientific computing in Python’. en. In: *Nature Methods* 17.3 (Mar. 2020), pp. 261–272. DOI: [10.1038/s41592-019-0686-2](https://doi.org/10.1038/s41592-019-0686-2). (Visited on 03/07/2023) (cited on pages 20, 45).
- [103] Richard P. Brent. ‘An Algorithm with Guaranteed Convergence for Finding a Zero of a Function’. In: *Comput. J.* 14 (1971), pp. 422–425 (cited on pages 20, 21, 40).
- [104] T. J. Dekker. ‘Find a zero by means of successive linear interpolation’. en. In: *Constructive Aspects of the Fundamental Theorem of Algebra: Proceedings of a Symposium Conducted at the IBM Research Laboratory, Zürich-Rüschlikon, Switzerland, June 5-7, 1967*. Ed. by Bruno Dejon and Peter Henrici. Vol. 8. Google-Books-ID: XRGoAAAIAAJ. Wiley-Interscience, 1969, p. 337 (cited on page 20).
- [105] Eric W. Weisstein. *Brent’s Method*. URL: <https://mathworld.wolfram.com/> (visited on 05/21/2023) (cited on page 21).
- [106] Jun Li and H. Jay Zwally. ‘Modeling of firn compaction for estimating ice-sheet mass change from observed ice-sheet elevation change’. en. In: *Annals of Glaciology* 52.59 (2011), pp. 1–7. DOI: [10.3189/172756411799096321](https://doi.org/10.3189/172756411799096321). (Visited on 05/02/2023) (cited on page 24).
- [107] Neige Calonne et al. ‘Thermal Conductivity of Snow, Firn, and Porous Ice From 3-D Image-Based Computations’. en. In: *Geophysical Research Letters* 46.22 (2019), pp. 13079–13089. DOI: [10.1029/2019GL085228](https://doi.org/10.1029/2019GL085228). (Visited on 05/03/2023) (cited on pages 25, 61).
- [108] Amaelle Landais et al. ‘Large temperature variations over rapid climatic events in Greenland: a method based on air isotopic measurements’. en. In: *Comptes Rendus Geoscience* 337.10 (Aug. 2005), pp. 947–956. DOI: [10.1016/j.crte.2005.04.003](https://doi.org/10.1016/j.crte.2005.04.003). (Visited on 05/08/2023) (cited on pages 31, 33, 41, 65–67).
- [109] E. Capron et al. ‘A global picture of the first abrupt climatic event occurring during the last glacial inception’. en. In: *Geophysical Research Letters* 39.15 (2012). DOI: [10.1029/2012GL052656](https://doi.org/10.1029/2012GL052656). (Visited on 05/08/2023) (cited on pages 31, 33, 41, 65–67).
- [110] Katrine K. Andersen et al. ‘Greenland Ice Core Chronology 2005 (GICC05) and 20 year means of oxygen isotope data from ice core NGRIP’. In: (). Type: dataset. DOI: [10.1594/PANGAEA.586838](https://doi.org/10.1594/PANGAEA.586838). (Visited on 05/19/2023) (cited on page 32).
- [111] Sigfus J. Johnsen et al. ‘Oxygen isotope and palaeotemperature records from six Greenland ice-core stations: Camp Century, Dye-3, GRIP, GISP2, Renland and North-GRIP’. In: *Journal of Quaternary Science* 16.4 (2001), pp. 299–307. DOI: <https://doi.org/10.1002/jqs.622> (cited on page 33).
- [112] B.M. Vinther et al. ‘A synchronized dating of three Greenland ice cores throughout the Holocene’. English. In: *Journal of Geophysical Research* 111 (2006). Paper id.: D13102 (cited on page 33).

- [113] S. O. Rasmussen et al. 'A new Greenland ice core chronology for the last glacial termination'. In: *Journal of Geophysical Research: Atmospheres* 111 (D6 2006). DOI: [10.1029/2005JD006079](https://doi.org/10.1029/2005JD006079). (Visited on 05/22/2023) (cited on page 33).
- [114] Katrine K. Andersen et al. 'The Greenland Ice Core Chronology 2005, 15–42ka. Part I: constructing the time scale'. In: *Quaternary Science Reviews. Critical Quaternary Stratigraphy* 25.23 (Dec. 2006), pp. 3246–3257. DOI: [10.1016/j.quascirev.2006.08.002](https://doi.org/10.1016/j.quascirev.2006.08.002). (Visited on 05/22/2023) (cited on page 33).
- [115] A. Svensson et al. 'A 60 000 year Greenland stratigraphic ice core chronology'. In: *Climate of the Past* 4.1 (2008), pp. 47–57. DOI: [10.5194/cp-4-47-2008](https://doi.org/10.5194/cp-4-47-2008) (cited on page 33).
- [116] E. W. Wolff et al. 'Millennial-scale variability during the last glacial: The ice core record'. In: *Quaternary Science Reviews. Vegetation Response to Millennial-scale Variability during the Last Glacial* 29.21 (Oct. 2010), pp. 2828–2838. DOI: [10.1016/j.quascirev.2009.10.013](https://doi.org/10.1016/j.quascirev.2009.10.013). (Visited on 05/22/2023) (cited on page 33).
- [117] klima-og geofysik Is-. *Data - icesamples - software*. en. July 2007. URL: <https://www.iceandclimate.nbi.ku.dk/data/> (visited on 05/08/2023) (cited on page 33).
- [118] A. Landais et al. 'A continuous record of temperature evolution over a sequence of Dansgaard-Oeschger events during Marine Isotopic Stage 4 (76 to 62 kyr BP)'. en. In: *Geophysical Research Letters* 31.22 (2004). DOI: [10.1029/2004GL021193](https://doi.org/10.1029/2004GL021193). (Visited on 05/08/2023) (cited on pages 33, 41).
- [119] E. Capron et al. 'Synchronising EDML and NorthGRIP ice cores using $\delta^{18}\text{O}$ of atmospheric oxygen ($\delta^{18}\text{O}_{\text{atm}}$) and CH_4 measurements over MIS5 (80–123 kyr)'. en. In: *Quaternary Science Reviews. Climate of the Last Million Years: New Insights from EPICA and Other Records* 29.1 (Jan. 2010), pp. 222–234. DOI: [10.1016/j.quascirev.2009.07.014](https://doi.org/10.1016/j.quascirev.2009.07.014). (Visited on 05/08/2023) (cited on pages 33, 41).
- [120] E. Capron et al. 'Millennial and sub-millennial scale climatic variations recorded in polar ice cores over the last glacial period'. In: *Climate of the Past* 6.3 (2010), pp. 345–365. DOI: [10.5194/cp-6-345-2010](https://doi.org/10.5194/cp-6-345-2010) (cited on pages 33, 41).
- [121] J. Schwander et al. 'Age scale of the air in the summit ice: Implication for glacial-interglacial temperature change'. In: *Journal of Geophysical Research* 1021 (Aug. 1997), pp. 19483–19494. DOI: [10.1029/97JD01309](https://doi.org/10.1029/97JD01309) (cited on page 33).
- [122] D. Dahl-Jensen et al. 'Past temperatures directly from the greenland ice sheet'. eng. In: *Science (New York, N.Y.)* 282.5387 (Oct. 1998), pp. 268–271. DOI: [10.1126/science.282.5387.268](https://doi.org/10.1126/science.282.5387.268) (cited on pages 34, 35).
- [123] Anais J. Orsi. 'Temperature reconstruction at the West Antarctic Ice Sheet Divide, for the last millennium, from the combination of borehole temperature and inert gas isotope measurements /'. en. PhD thesis. University of California, San Diego, 2013. (Visited on 05/11/2023) (cited on page 41).
- [124] Alexi M. Grachev and Jeffrey P. Severinghaus. 'Determining the Thermal Diffusion Factor for $^{40}\text{Ar}/^{36}\text{Ar}$ in Air To Aid Paleoreconstruction of Abrupt Climate Change'. In: *The Journal of Physical Chemistry A* 107.23 (June 2003), pp. 4636–4642. DOI: [10.1021/jp027817u](https://doi.org/10.1021/jp027817u). (Visited on 05/11/2023) (cited on page 41).
- [125] J. D. Morgan et al. 'Gas isotope thermometry in the South Pole and Dome Fuji ice cores provides evidence for seasonal rectification of ice core gas records'. In: *The Cryosphere* 16.7 (2022), pp. 2947–2966. DOI: [10.5194/tc-16-2947-2022](https://doi.org/10.5194/tc-16-2947-2022) (cited on page 41).

- [126] Takuro Kobashi, Jeffrey P. Severinghaus, and Kenji Kawamura. 'Argon and nitrogen isotopes of trapped air in the GISP2 ice core during the Holocene epoch (0–11,500 B.P.): Methodology and implications for gas loss processes'. In: *Geochimica et Cosmochimica Acta* 72.19 (Oct. 2008), pp. 4675–4686. DOI: [10.1016/j.gca.2008.07.006](https://doi.org/10.1016/j.gca.2008.07.006). (Visited on 05/21/2023) (cited on page 41).
- [127] Hugues Goosse. *Climate System Dynamics and Modelling*. Cambridge University Press, Aug. 2015. (Visited on 05/21/2023) (cited on page 42).
- [128] Muhammad Iqbal. 'Chapter 5 - A CLOUDLESS-SKY ATMOSPHERE AND ITS OPTICS'. en. In: ed. by Muhammad Iqbal. Academic Press, Jan. 1983, pp. 85–105. DOI: [10.1016/B978-0-12-373750-2.50010-0](https://doi.org/10.1016/B978-0-12-373750-2.50010-0). (Visited on 05/11/2023) (cited on page 42).
- [129] C. Huber et al. 'Evidence for molecular size dependent gas fractionation in firn air derived from noble gases, oxygen, and nitrogen measurements'. In: *Earth and Planetary Science Letters* 243.1 (Mar. 2006), pp. 61–73. DOI: [10.1016/j.epsl.2005.12.036](https://doi.org/10.1016/j.epsl.2005.12.036). (Visited on 05/21/2023) (cited on page 42).
- [130] Michael Döring and Markus Christian Leuenberger. 'Comparison of Holocene temperature reconstructions based on GISP2 multiple-gas-isotope measurements'. In: *Quaternary Science Reviews* 280 (Mar. 2022), p. 107274. DOI: [10.1016/j.quascirev.2021.107274](https://doi.org/10.1016/j.quascirev.2021.107274). (Visited on 05/21/2023) (cited on pages 42, 60).
- [131] James Walsh. 'The Ocean and Climate Change: Stommel's Conceptual Model'. In: *CODEE Journal* 12.1 (Feb. 2019). DOI: [10.5642/codee.201912.01.03](https://doi.org/10.5642/codee.201912.01.03) (cited on page 52).
- [132] J R Bourne. 'Chapter 10 - Mixing in single-phase chemical reactors'. In: *Mixing in the Process Industries*. Ed. by N Harnby, M F Edwards, and A W Nienow. Oxford: Butterworth-Heinemann, Jan. 1992, pp. 184–199. DOI: [10.1016/B978-075063760-2/50031-7](https://doi.org/10.1016/B978-075063760-2/50031-7). (Visited on 05/21/2023) (cited on page 52).

Index

A

Air advection	18
Buizert	19
Darcy	18
Air diffusion	15

B

BAR Model	10
Brent's method	20

C

Community Firn Model	23
Main run	25
Spin-up run	25
Convection	16

D

Dekker's method	20
delta notation	3

E

Effective diffusivity	17
-----------------------------	----

F

Firn	5
------------	---

G

GICCo5ext	32
GOU Model	11
Gravitational fractionation	13

H

Heat diffusion	4
HLA Model	9
HLD Model	7
HLS Model	10

I

Ice core	3
----------------	---

L

Lock-in depth	5
---------------------	---

M

Molecular diffusion	6
Multiprocessing	36

N

NGRIP data	32
------------------	----

O

Orbital time scales	4
---------------------------	---

P

Porosity	5
Closed	5
Open	5

R

Rayleigh Distillation	4
Root-finder	35

T

Thermal fractionation	14
-----------------------------	----

W

Water stable isotopes	3
-----------------------------	---

Z

Zones of densification	5
Convective zone	6
Diffusive zone	6
Lock-in zone	6